KINEMATICS AND DYNAMICS OF OCEANIC OVERFLOWS: APPLICATION TO THE DENMARK STRAIT AND FAROE BANK CHANNEL

by

Atousa Saberi

A dissertation submitted to The Johns Hopkins University

in conformity with the requirements for the degree of

Doctor of Philosophy

Baltimore, Maryland

July, 2022

Abstract

An important mechanism in redistribution of heat and salt in the ocean is known as the global meridional overturning circulation. Oceanic overflows contribute to the deep branches of the conveyor belt. Determining overflow dynamics and kinematics is critical to estimating the changes in overflow production and composition as it ultimately impacts global ocean circulation. In this work, we first present the kinematics of a specific sea-strait, and then study some aspects of overflow dynamics. We study the overflow of dense water from Denmark Strait (known as Denmark Strait Overflow, DSO) which feeds the lower limb of the conveyor belt in the northern extremity of the Atlantic Ocean. We investigate the upstream pathways of the DSO through the application of backward Lagrangian particle tracking in a realistic ocean model. The Lagrangian analysis confirms the existence of previously known branches from the North and it also reveals an additional pathway emerging from south of Iceland. The southern pathways supply over 25% of the DSO during winter of 2008 when the North Atlantic Oscillation (NAO) index was positive and can potentially change depending on the phase of the NAO. The southern pathways mark a more direct route from the near-surface subpolar

North Atlantic to the NADW. The second part of this study involves the dynamics of overflow pathway partitioning and the effect of upstream reservoir on overflow production for an idealized sea-strait geometry with a continuously varying (parabolic) cross-section. We use rotating hydraulic theory and idealized modeling to reveal the relation between reservoir conditions, strait geometry, and overflow transport. The results reveal that the basin circulation intrudes more into the channel for a wide parabola with low curvature than a narrow parabola causing large variations in the interface height near the channel. Far enough from the channel entrance, the hydraulically controlled flow in the strait is nearly independent of the basin circulation regardless of the parabolic curvature. Comparing the model to theory, we find that the measurement of the wetted edges of the flow at the critical section can be used for prediction of the volume flux. Based on this finding, we suggest three monitoring strategies for transport estimation and compare the estimates with the observed values at the Faroe Bank Channel. The results show that the estimated transports are within the range of observed values. The third part of this work is about the effect of hydraulic control on the variability in transport observed in some sea-straits on timescales such as the seasonal cycle. We force our numerical model with periodic inflow in the upstream basin for subcritical and hydraulically controlled flow to see the effect of hydraulic control on the suppression of time variability. Results reveal that although the narrowing and shallowing of topography lead to a local suppression of time dependence, the hydraulic control at the sill causes a further suppression of time variability.

Thesis Committee

Primary Readers

Thomas W. N. Haine (Primary Advisor)
Professor
Morton K. Blaustein Department of Earth and Planetary Sciences
Johns Hopkins Krieger School of Arts and Sciences

Anand Gnanadesikan
Professor
Morton K. Blaustein Department of Earth and Planetary Sciences
Johns Hopkins Krieger School of Arts and Sciences

Alternate Readers

Darryn W. Waugh
Professor
Morton K. Blaustein Department of Earth and Planetary Sciences
Johns Hopkins Krieger School of Arts and Sciences

Acknowledgments

Throughout the PhD journey I have received a lot of support from mentors, colleagues, friends, and family.

I am eternally thankful to my primary advisor and mentor, Thomas Haine. I would like to thank him for always encouraging me to pursue my interests, and helping me in thought organization and in developing independence in pursuing scientific endeavors.

I would like to sincerely thank my mentor and friend, Larry Pratt, who co-advised $2/3^{rd}$ of my research. He always made himself available and answered every question I had with patience, and a unique sense of humor.

I would like to thank my Ph.D. committee, Anand Gnanadesikan for always encouraging me to think about the big picture and Darryn Waugh for his constructive comments and supportive advice. They kindly made themselves available whenever I needed their support. I would like to thank my mentors and collaborators, Karl Helfrich, Amy Bower, and Heather Furey for helping me understand some of the concepts involved in my research. I am also grateful for the opportunity to learn about good teaching practices from Rebecca Kelly and Alexios Monopolis. They helped me develop a deeper understanding of the impact of humans on Earth systems, and the rise of

pressing issues such as population growth, and endangerment of biodiversity and natural resources. I would like to thank Sabine Stanley for being a great mentor and lending her ears to any complaints I had about graduate student life.

I would like to thank lab-mates and friends, Molly Menzel, Mahmoud Osman, Saman Karimi, Aleksi Nummelin, Renske Gelderloos, Mattia Almansi, and Ali Siddiqui for thoughtful research discussions. I would also like to thank international colleagues and friends such as Ailin Brakstad, Stefanie Semper, and Shuwen Tan for the inspiring science discussions.

PhD has been a long journey with lots of unique sweet and bitter events that has shaped my personality. It started with living separate from my lifelong friend, my college sweetheart, my beloved husband, Soroosh, and ended with the joy of having a sweet son, Kayhan. I am eternally grateful to Soroosh for being a loving and supportive partner. During this adventure, Soroosh was additionally like a colleague whom I sometimes had scientific and technical discussions with.

My deepest respect to my parents for their love, sacrifices and emotional support and gratitude for my brother whose sense of humor made me laugh in difficult situations. If anything, this journey made me see how precious it is to have kind people, family and friends around.

Table of Contents

List of Tables

List of Figures

Chapter 1

Introduction

Never my heart deprived of
knowledge, few secrets were not
divulged
for seventy-two years I pondered
day and night, only to know that
I know nothing.

Omar Khayyam, Rubaiyat.

1.1 The role of deep ocean passages in the climate system

Sills, straits, and passages connect separate ocean basins. A sill is a ridge that separates one basin from another. An oceanic sill is a topographic saddle with the sill depth analogous to the saddle point. In the deep ocean, sills connect deep basins. The sill depth controls the density of waters that can flow over the ridge. Similarly, straits and passages are submarine topographies, that connect deep basins such as in fracture zones. These complex topographies steer the flow and constrain it horizontally. They play an important role in the

distribution of water masses and the location of currents.

Much of the mixing in the ocean occurs near these complex topographic features and the boundaries. Observations in different parts of the global ocean suggest that the flow over steep bottom slopes in the deep ocean is a major mechanism for dissipating the ocean's energy (Talley et al., 2013). The flows of water through the straits, canyons, and over topographic features are similar in many ways; these dense overflows undergo significant mixing, entrain ambient fluid, which dilutes the temperature and salinity signal of the water, and increases the volume flow (Price and Baringer, 1994; Chassignet, Cenedese, and Verron, 2012). Although the mixing in overflows is highly localized (North, Jochumsen, and Moritz, 2018), it plays a significant role in influencing the large-scale ocean circulation (Koszalka, Haine, and Magaldi, 2017). Overflows are stratified. As the water moves down topography it accelerates due to gravity and the strong shear between different layers with different densities lead to a turbulence-generating instability. They are affected by rotation which constrains the flow to approximately follow topographic contours. Additionally, many of the passages, shallow or deep, are strategically advantageous locations for the measurement of property fluxes relevant to the ocean circulation and to the global climate due to their chocking effect (Pratt and Whitehead, 2008).

1.2 Greenland-Scotland Ridge

The large-scale circulation of the ocean also known as the Meridional Overturning Circulation (MOC) consists of shallow and deep-water currents that

transport mass, heat, carbon, and nutrients around the globe. One of the components of the global ocean circulation is in the Atlantic Ocean basin and is called the Atlantic Meridional Overturning Circulation (AMOC). The North Atlantic Deep Water (NADW) is the major input of dense water sustaining the AMOC. The densest component of NADW is provided by overflows through Greenland-Scotland Ridge. The Greenland-Scotland Ridge is the gateway for flow exchange between the Arctic Ocean, the Nordic Seas and the North Atlantic Ocean. The dense and deep waters in the North Atlantic originate in the Nordic Seas. It is also one of the few regions where considerable amounts of atmospheric carbon dioxide (CO2) uptake by the ocean happens throughout the year (Drange et al., 2005). The strong air-sea exchange of momentum, heat, and freshwater in the Nordic Seas leads to a significant water mass transformation, especially during winter. Additionally, the carbon, nutrients, and oxygen in these waters play an important role in determining the chemical properties of the deep ocean and the carbon concentration of the atmosphere (Marinov et al., 2008). It is also a key region where the dense waters that fill the deep North Atlantic are formed. The flow through Denmark Strait and Faroe Bank Channel accounts for about 90% of the total overflow entering the North Atlantic Deep Water (Østerhus et al., 2019).

These two straits are the main gateways between the Nordic Seas and the North Atlantic Ocean. The Nordic Seas are comprised of the Norwegian Sea, Greenland Sea and the Iceland Sea shown in Figure 1.1. The warm Atlantic-origin waters marked in red move northward via Norwegian Atlantic Water (NAW) and the North Icelandic Irminger current (NIIC). These waters become

densified in the Nordic Seas and return south via the East Greenland Current (EGC), North Icelandic Jet (NIJ), and Iceland Faroe slope jet (ISFJ).

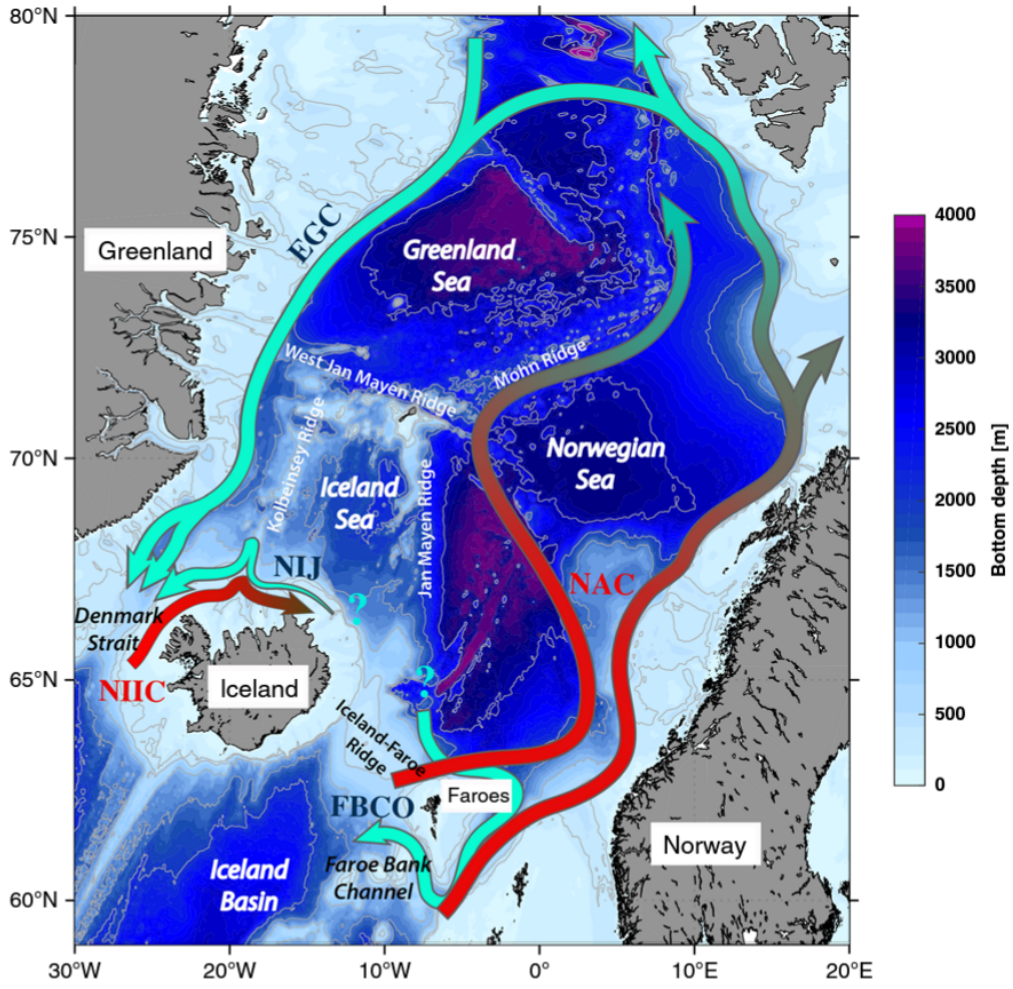

Figure 1.1: The Nordic Seas (the Greenland Sea, Norwegian Sea and Iceland Sea) and the Irminger Sea are labeled. The pathways of warm Atlantic inflow and dense outflow are shown in red and green arrows, respectively. Norwegian Atlantic Current (NAC), North Icelandic Irminger Current (NIIC), East Greenland Current (EGC), North Icelandic Jet (NIJ), and Faroe Bank Channel overflow are shown. The figure is retrieved from Huang et al., 2020.

The Denmark Strait and Faroe bank Channel are the focus of this thesis. Despite prior attempts to understand the overflow through Denmark Strait

(known as DSO), its properties, sources and pathways are still mysterious. That is because the characteristics of the DSO are variable at the Denmark Strait. This makes it challenging to study the DSO from observations. Given the complexity of observing the real-world ocean, exploring the DSO pathways in a realistic ocean model is needed.

The overflows of dense water at the Denmark Strait and Faroe Bank Channel are *hydraulically controlled*, meaning that the sills are able to regulate the volume flow rate and the reservoir level (Käse, Girton, and Sanford, 2003; Pratt and Whitehead, 2008). Therefore, hydraulic theory can explain the dynamics of overflow pathway partitioning and the effect of upstream reservoir on overflow production for a given sea-strait geometry. The Denmark Strait and Faroe Bank Channel are two examples of deep ocean passages in the ocean that are advantageous sites for long term monitoring of deep transport.

In addition to illuminating the dynamics of the overflow, rotating hydraulics theory provides potential for simplifying monitoring strategy by reducing the number of quantities that need to be measured. This has been done before through previous analytical models (Whitehead, Leetmaa, and Knox, 1974; Gill, 1977; Whitehead, 1989; Whitehead, 1998; Borenäs and Nikolopoulos, 2000; Killworth and McDonald, 1993) . However, the applicability of these theories has been limited by idealizations such as restriction to zero or uniform potential vorticity (pv) and to channels with rectangular cross sections. None of these studies considered various types of inflow and their effect on the controlled flow in the channel, however, nor did they consider effects of dissipation or friction. Helfrich and Pratt, 2003 developed an idealized

model of a basin-strait system with bottom friction and three different basin inflows. Their study was restricted to a channel with rectangular channel cross section, bounded by vertical walls, as in most of the previous studies. Despite mathematical convenience in considering a rectangular cross-section it is not realistic in the real world. It is important to study the dynamics of channels with continuously varying (parabolic) cross-sections to account for the rounded nature of sea-strait topographies and potentially improve monitoring strategies for realistic channel geometries.

At FBC, there is an observed seasonal variability in volume transport with maximum in August and minimum in February (Østerhus et al., 2008). At Denmark Strait, however, despite changes in overflow sources, the seasonality in transport is weak (Huang et al., 2020). While the formation of overflow water is a seasonal process, the seasonality at the sill section is weak. The time variability in overflow transport can be studied through rotating hydraulic theory.

1.3 Outline

In chapter 2 we focus on the kinematics of Denmark Strait Overflow and address the following questions: What are the origins and pathways of the DSO? How do the model pathways compare with observed pathways? How do the temperature, salinity, depth and density of the overflow water evolve along the DSO pathways?

Chapter 3 focuses on exploring the dynamics of overflow pathway partitioning and the effect of upstream reservoir on overflow production for a canonical sea-strait geometry. We study the dynamics of channels with continuously varying (parabolic) cross-sections to account for rounded nature of sea-strait topographies. We also develop overflow monitoring strategies. The theoretical result is applied to the Faroe Bank Channel case study and is compared against observations. The following questions are addressed: How does the change in channel geometry from rectangle to parabola change the flow physics? What are the transport pathways from the mass source through the basin, into the narrow strait and over the shallow sill? How do these pathways change as the location of the mass source changes? How is the interface in the channel affected by the parabolic bottom topography? What are some possible monitoring strategies that take advantage of the fact that hydraulic control and hydraulic criticality exist at or near the sill? What is the best location to conduct monitoring with fixed instruments? Are there any trade-offs in terms of convenience and accuracy between possible strategies?

The sources of the overflows can vary in time which can result in variability in the overflow transport. In Chapter 4 we elaborate on the potential role of the hydraulic control on the observed variability in transport at some sea-straits such as FBC, by targetting the following questions: Does hydraulic control suppress time dependence in the overflow transport? Does narrowing and shallowing of topography lead to a local suppression of time dependence and, if so, to what extent hydraulic control is implicated? Is the suppression of

variability a function of frequency and amplitude of forcing?

Chapter 5 summarizes the key findings of each chapter and discusses potential avenues for future work.

In the appendix, the findings from teaching experience and how that informed my perspective on research is shared.

Chapter 2

Lagrangian Perspective on the Origins of Denmark Strait Overflow

> Time travels in diverse paces with diverse persons. I will tell you who time ambles withal, who time trots withal, who time gallops withal, and who he stands still withal.
>
> W. Shakespeare, As you like it.

2.1 Introduction

The dense waters entering the Atlantic Ocean from the northern latitudes spill across the Greenland-Iceland-Scotland ridges through two main passages: the Denmark Strait and Faroe Bank Channel. The two overflows merge after entrainment to form the densest constituent of North Atlantic Deep Water (NADW), which is the main contribution to the deep branch of the north Atlantic Meridional Overturning Circulation (AMOC) (Swift, Aagaard, and

Malmberg, 1980; Pratt and Whitehead, 2008; Østerhus et al., 2019). The focus of this study is the origins of the dense water that cascades over Denmark Strait, known as Denmark Strait Overflow (DSO). The DSO is a major export route for dense waters in the Nordic Seas, feeding the deep western boundary current (Dickson and Brown, 1994). The mean volume transport of the DSO is approximately 3.2 ± 0.5 Sv (Macrander et al., 2007; Jochumsen et al., 2017). Determining the overflow origins and pathways is important for estimating the state and variability of the AMOC and hence the climate system.

Furthermore, water flowing across a topographic barrier is a ubiquitous process in the ocean and the DSO is a prime example (Pratt and Whitehead, 2008). The flows of water through narrow straits, canyons and over topographic features are similar in many ways; these dense overflows undergo significant mixing, entrain ambient fluid, which dilutes the temperature and salinity signal of the water, and increases the volume flow (Price and Baringer, 1994; Chassignet, Cenedese, and Verron, 2012). Although the mixing in overflows is highly localized (North, Jochumsen, and Moritz, 2018), it plays a significant role in influencing the large scale ocean circulation (Koszalka, Haine, and Magaldi, 2017). Studying the DSO helps us understand common features of climatologically important overflow processes in other parts of the global ocean.

The fate and downstream evolution of the overflow and its variability have been well studied through observations (Macrander et al., 2005; Tanhua, Olsson, and Jeansson, 2008) and realistic modeling both in Eulerian (Köhl et al., 2007; Haine et al., 2008; Almansi et al., 2017) and Lagrangian representations

of the flow field (Koszalka, Haine, and Magaldi, 2013; Appen et al., 2014). The formation, sources, and pathways of the DSO have also been studied (Rudels et al., 2002; Köhl et al., 2007). However, despite various proposed circulation schemes based on hydrographic transects (Harden et al., 2016; Våge et al., 2013), the sources and details of the DSO upstream pathways are still uncertain due to mesoscale eddy features, short timescale (3 - 5 day) variability, mixing, and watermass transformation (Almansi et al., 2017; Spall et al., 2019; Moritz et al., 2019).

There are two main hypothesized sources of the DSO. The first source is the Atlantic-origin water (warmer than 0°C) resulting from transformation in the eastern part of the Nordic Seas (Mauritzen, 1996) and the second source is the Arctic-origin water (colder than 0°C) resulting from transformation in the Greenland and Iceland Seas (Swift and Aagaard, 1981). The first source is transported primarily by the East Greenland Current (EGC) that flows along the east Greenland shelfbreak. The EGC bifurcates upstream of the Denmark Strait, with one branch continuing along the east Greenland shelfbreak and a separated branch called the separated EGC (sEGC) (Våge et al., 2013) located farther offshore, near the base of the Iceland slope. The contribution of the EGC to the DSO was recognized through hydrography, age analysis, and isotope ratio measurements (Swift, Aagaard, and Malmberg, 1980; Smethie Jr. and Swift, 1989; Rudels et al., 2002; Tanhua, Olsson, and Jeansson, 2005).

The second DSO source is carried by the North Icelandic Jet (NIJ) which is centered near the 650 m isobath approaching Denmark Strait from the Iceland slope (Jónsson and Valdimarsson, 2004; Våge et al., 2011; Semper et al., 2019).

Chemical oceanography studies suggest that there are other water masses contributing to the DSO (Jeansson et al., 2008; Tanhua, Bulsiewicz, and Rhein, 2005), but their percentage of contribution appears to be small (Mastropole et al., 2017). The NIJ and EGC currents are observed to be less distinguishable from each other closer to the Denmark Strait (Jónsson and Valdimarsson, 2004). To distinguish the currents upstream of Denmark Strait, Harden et al. (2016) analyzed data from a densely instrumented mooring array deployed from September 2011 to July 2012 at the Kögur section, which is roughly 200 km north of Denmark Strait (see Figure 2.1).

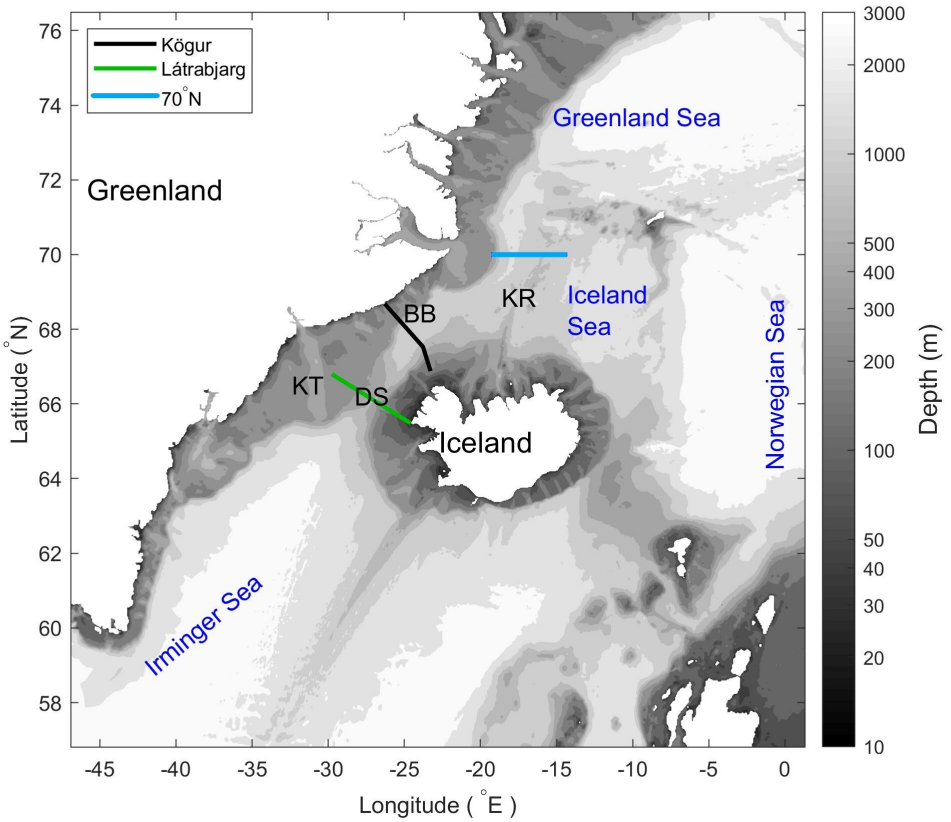

Figure 2.1: The bottom topography of the model, and model boundaries. The isobath shading is shown in logarithmic intervals. The abbreviation for topographic features are: Denmark Strait (DS), Blosseville Basin (BB), Kolbeinsey Ridge (KR), and Kangerdlugssuaq Trough (KT). The Kögur and Látrabjarg sections are shown with black and green lines, respectively. A section at 70°N, used for comparison with observation is shown with blue line (see Figure 2.3). The Nordic Seas (the Greenland Sea, Norwegian Sea and Iceland Sea) and the Irminger Sea are labeled in blue.

The sEGC is typically found near the base of the Iceland slope and is often difficult to distinguish from the NIJ. In the yearly-mean hydrographic and orthogonal velocity at the Kögur section, the NIJ and sEGC appear as a single feature (Harden et al., 2016). The NIJ also interacts with the (inshore) northward- flowing relatively warm and saline North Icelandic Irminger

Current (NIIC) when the bottom topography steers the two currents close together (Pickart et al., 2017).

These studies of the DSO sources and pathways have been mostly based on Eulerian measurements and moorings at historical hydrographic sections. Although they estimate transport and hydrographic properties, they do not conclusively show the connectivity between sections and the evolution of individual currents from one section to another (Jong et al., 2018). The vertical sections are distant from each other, which makes it challenging to trace the origins of the DSO water through the currents that carry them from one vertical section to the other (Tanhua, Olsson, and Jeansson, 2008). There is only one Lagrangian study from observations that investigates pathways of dense water using acoustically tracked, high-resolution RAFOS float trajectories (Jong et al., 2018). These float trajectories revealed new information on the connection between the EGC and the NIJ, and on the subsurface circulation in the Iceland Sea. But they are relatively few in number, and could not be tracked through the Strait itself, leaving some gaps in our knowledge of pathways leading up to the sill (Jong et al., 2018). Given the complexity of observing pathways leading to the DSO, it is sensible to explore them in a realistic circulation model, in particular to perform backward Lagrangian particle tracking to investigate the origins of the dense waters flowing over the sill at Denmark Strait. Here we apply this technique using a well-studied regional model (Almansi et al., 2017) to trace the near-field origins of the overflow. The available model run, described in detail in the following section, is 15 months long, limiting our ability to study long term trends and seasonality with this

particular simulation. Nevertheless, short term evolution of the Lagrangian particle pathways and hydrographic properties leading up to the sill can be revealed in detail.

The words *origin* and the *DSO* need to be carefully defined. The question of the origin of a watermass is time and space dependent. The farther back in time, the more distributed the *origin* of a watermass in space becomes. It is important to determine how far back in time we are interested in the DSO sources. In this paper, we define the word *origin* as the farthest upstream location from the Denmark Strait in our computational domain within a three month time window, which is the shortest length within the time boundaries of our model run that reveals geographically distinct DSO sources. The DSO needs to be defined as well. In the literature various criteria based on temperature or density have been used (Cooper, 1955; Tanhua, Olsson, and Jeansson, 2008; Behrens et al., 2017). In this study, we use the most common definition by Dickson and Brown, 1994: The DSO is the water with $\sigma_\theta \geq 27.8$ kg m^{-3} at the Látrabjarg sill section (see Figure 2.1) that flows southwards after cascading over the Denmark Strait (by *sill section* we mean the saddle point in the bottom topography that the Látrabjarg section transects). In this paper, we address the following questions: What are the origins and pathways of the DSO? How do the model pathways compare with observed pathways? How do the temperature, salinity, depth and density properties evolve along the DSO pathways? How do the Lagrangian pathways improve our understanding of circulation in the area? How do the main currents interact? What is the best schematic representation of the DSO pathways?

In section 2 of this chapter, the details of the numerical model, the particle tracking code, and the observational data used for this study are discussed. In section 3 model results are compared with observations, the Lagrangian particle tracking results are presented, and the DSO particle properties, trajectories, and preferred pathways are investigated. A summary and discussion are provided in section 4.

2.2 Methodology

2.2.1 Numerical model configuration

The flow field is calculated using the hydrostatic version of the Massachusetts Institute of Technology General Circulation Model (MITgcm) developed by Marshall et al., 1997. It solves the Navier-Stokes equations under the Boussinesq approximation for an incompressible fluid in a rotating frame of reference. The model domain is configured for the Denmark Strait and it includes the sub-Arctic region from the Greenland Sea to Cape Farewell (Figure 2.1). The model simulation period is from 01-Sep-2007 to 30-Nov-2008. The temporal resolution of the model is 30 seconds but the output is stored every 6 hours. The horizontal grid resolution is 2 km in the center of the domain from 60°N to 71°N (Figure 2.1), and it decreases to 4 km moving toward the boundaries. The vertical grid resolution decreases from 2 to 15 m in the upper 120 m and is 15 m thereafter.

The model configuration is identical to that of Almansi et al., 2017, except

that the atmospheric forcing at the surface (air temperature, specific humidity, wind, evaporation, precipitation, and radiation) is based on three hourly 15 km resolution fields from the regional Arctic System Reanalysis product (ASRv2;UCAR-NCAR and OHSTATE-POLARMET, 2017). The model is initialized using the global $1/12^{\circ}$ reanalysis of the HYbrid Coordinate Ocean Model (HYCOM) + Navy Coupled Ocean Data Assimilation (NCODA) (Cummings and Smedstad, 2014), and a coupled ocean-sea ice data assimilation product for the North Atlantic Ocean and Arctic called the TOPAZv4 monthly reanalysis (Sakov et al., 2012). At the open boundaries, time series of velocity, temperature, and salinity from HYCOM + NCODA are used. The sea surface temperature is relaxed to the satellite data from the Operational Sea Surface Temperature and Sea Ice Analysis (OSTIA) global product with a time scale of 5 days (Donlon et al., 2012). The oceanic component is coupled with the MITgcm sea ice model (Losch et al., 2010). Freshwater forcing from runoff, and solid and liquid discharge is used along the Greenland coast from a combination of climate models, remote sensing, and terrestrial data (Noël et al., 2016; Bamber et al., 2012).

2.2.2 Passive Lagrangian Particle Tracking

Lagrangian trajectories of virtual particles are calculated using a three dimensional particle tracking package developed by Koszalka, Haine, and Magaldi, 2013 and Gelderloos et al., 2016 in MATLAB (Reichelt and Shampine, 2010). For this study, the code is extended to compute the trajectories at a single

depth level in isobaric mode as well. The algorithm employs a MATLAB built-in Ordinary Differential Equation (ODE) solver to solve for particle position at each time step. The particles at each time step are advanced with the two- or three-dimensional velocity field linearly interpolated to the instantaneous position of the particle. The code does not have explicit diffusion, as we assume all the information about the flow is contained in the velocity field output of the MITgcm model. The velocity component normal to boundaries is zero and the particles slide along the solid boundaries of the domain. The evolution of tracer fields such as salinity and temperature along the Lagrangian paths are obtained by nearest-neighbor interpolation of the model output to the particle positions. The model equation of state (Jackett and Mcdougall, 1995) is then used to compute the density of the particles.

2.2.3 Observations

Several observational data sets are compared to the model output to build confidence in the realism of the model. Shipboard data, moorings, and hydrographic sections are used to perform the comparison in an Eulerian frame, while RAFOS float trajectories and properties (Jong et al., 2018) are used to perform the comparison in a Lagrangian frame.

2.2.3.1 Kögur mooring array

In order to perform model-data comparison upstream of Denmark Strait, data from the Kögur mooring array is used. Harden et al., 2016 analyzed

results from a year-long densely instrumented mooring array upstream of the Denmark Strait, across the Blosseville Basin and along the Kögur section (shown in Figure 2.1). Each of the 12 moorings was equipped with instruments measuring temperature, salinity, pressure, and current velocity. The data coverage is from 29-Aug-2011 to 30-Jul-2012. The hydrographic and the velocity data are interpolated into a structured grid with a spatial resolution of 8 km in the horizontal and 50 m in the vertical direction. The temporal resolution of the gridded product is 8 hours. Harden et al. (2016) explain the details of the data and interpolation scheme used for gridding the data in their Appendix A and B.

2.2.3.2 RAFOS float and shipboard data

In order to make a direct comparison between the model Lagrangian trajectories and the floats, we use isobaric RAFOS floats deployed near 70°N on a zonal section in July 2014 (Jong et al., 2018). The complete RAFOS dataset contained 52 floats, but only the 11 floats that drifted near the Denmark Strait are considered here. The information about these floats studied here is listed in Table 2.1. They are isobaric subsurface drifters ballasted for the depth of interest and the hydrographic properties of the study region (Rossby, Dorson, and Fontaine, 1986). The floats were tracked by acoustic signals on a daily schedule from six sound sources moored in the Iceland Sea (Jong et al., 2018). They provide pressure, temperature, and arrival times of acoustic signals along their trajectories. They were deployed in water with σ_θ >28.0 kg m^{-3} in order to be embedded in the overflow water. At the RAFOS float deployment locations, shipboard conductivity-temperature-depth (CTD) measurements

were taken. The CTD data are used to make a direct comparison of temperature and salinity at the initial positions of the RAFOS floats and the modeled Lagrangian particles.

2.2.3.3 Hydrographic data

Data provided by the Marine and Freshwater Research Institute (Malmberg and Valdimarsson, 2003) are used to verify the realism of the model at the Látrabjarg section. The data are from a monitoring project in Icelandic waters that has been ongoing since 1990 (Malmberg and Valdimarsson, 2003), and the research on the Icelandic waters hydrographic variability and environmental effects on Icelandic fisheries (Palsson, Astthorsson, and Valdimarsson, 2012). In addition, hydrographic profiles from year 1980-2017 on the Iceland shelf are collected from various databases such as Unified Database for Arctic and Subarctic Hydrography (Behrendt et al., 2017), World Ocean Database (WOD, 2013), and International Council for the Exploration of the Seas (ICES, 2006). These data are used to better understand the characteristics of water on the Iceland shelf.

2.3 Results

2.3.1 Comparison with observations

2.3.1.1 Moorings at Kögur

The model results are compared with the year-long mean hydrographic properties and orthogonal velocity from the Harden et al., 2016 Kögur mooring deployment (Figure 2.2).

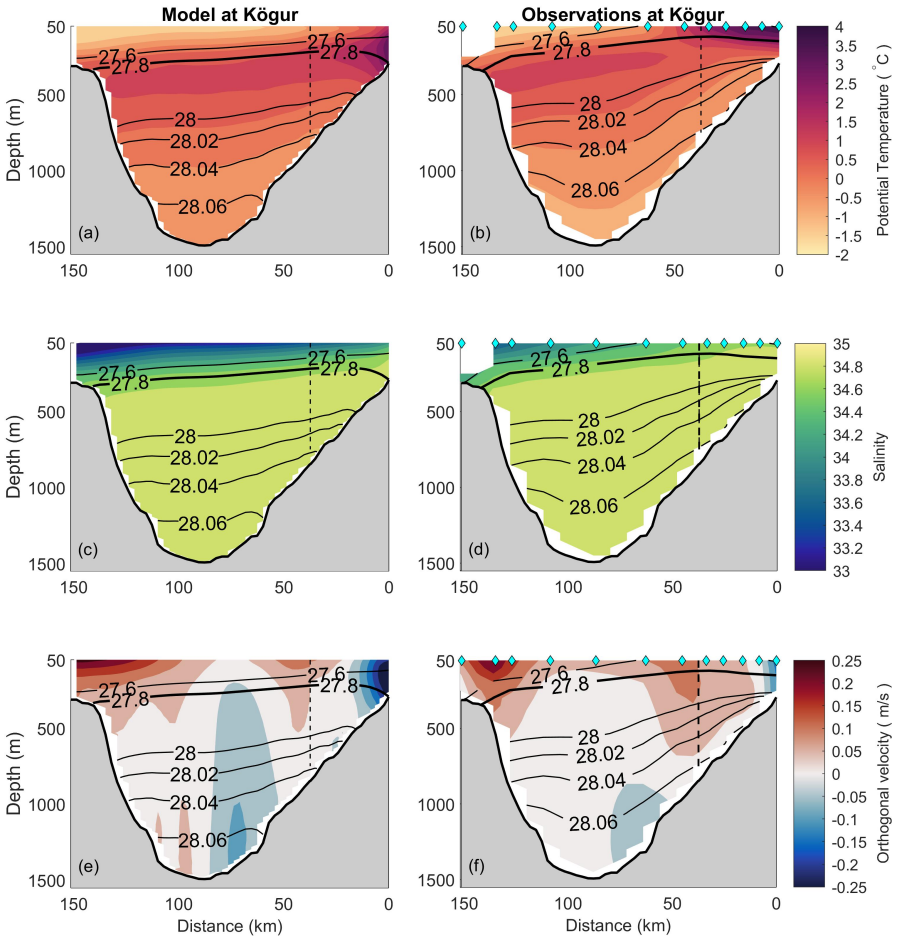

Figure 2.2: Comparison of year-long mean hydrographic properties and orthogonal velocity from model (a), (c) and (e) with mooring observations (b), (d), and (f) at the Kögur section. Distance is measured along the section from the Iceland shelf break. The mooring locations are marked by cyan diamonds. Isopycnals are contoured in black. The 27.8 kg m^{-3} isopycnal is highlighted by the bold black contour. The vertical dashed line indicates the location where the orientation of the section changes (see Figure 2.1). The equatorward orthogonal velocities in panels (e) and (f) are positive.

Although the year of observation (2011-2012) does not coincide with the modeled year (2007-2008), the hydrographic structures from the model (panels (a) and (c)) match the observations (panels (b) and (d)) well. The transition

from warm and salty North Atlantic water with sub-tropical origin (referred to as Irminger Water) to the cold and fresh Polar Surface Water in the upper layer is evident in both the model and observations along the section from east to west. The cold and fresh Polar Surface Water extends across the section from the west in both cases. The Irminger Water region extends somewhat further in the observations than in the model.

Harden et al., 2016 observed two water masses below the 27.8 kg m^{-3} isopycnal: the Recirculated Atlantic Water and Arctic-origin Water. The Recirculated Atlantic Water, defined by potential temperature, $\theta > 0^{\circ}$ C, and salinity, $S > 34.9$, is observed between depths of 300 and 800 m. The Arctic-origin Water with $\theta < 0°$C and $\sigma_\theta > 28$ kg m^{-3} is found below 800 m closer to Greenland, but it can also be seen at shallower depths on the Iceland slope. These two water masses can be seen in the model, too; however, the model mean potential temperature is higher by about 0.2°C in the deeper part of the section (below 1200 m), and also the Arctic-origin Water is less extended to the Iceland side of the Strait (see supplementary material for comparison of model with observations in $\theta - S$ diagram).

The isopycnal structure in the model is similar to that of the observations in the middle and western parts of the section. However, the slope of isopycnals is steeper towards the Iceland shelf in the observations which has dynamical implications for the strength of the NIJ. The model has a lower shear and slightly smaller orthogonal velocity in the year-long mean field as shown in Figure 2.2 (e) and (f). The individual snapshots (not shown) have better consistency with observations in isopycnal structure. Moreover, the isopycnals

are slightly deeper in the model, consistent with the deep warm bias found at Denmark Strait by Almansi et al., 2017.

The orthogonal velocity in both panels (e) and (f) consists of two main equatorward currents, one on the Greenland side and the other on the Iceland side. The model agrees well with the observations in capturing the surface-intensified East Greenland Current on the Greenland shelf break. The EGC maximum velocity at its core is 0.3 m s^{-1} in both model and observations. As Harden et al., 2016 describe, on the Iceland side there are two distinct currents that appear as a single feature in the mean field: the NIJ, a mid-depth intensified flow positioned near the 650 m isobath, and the sEGC, a surface-intensified current located seaward of the NIJ. In the annual mean field, the NIJ and the sEGC have one core in both observations and model. However, the two currents appear as distinct features with separated cores in some individual snapshots (not shown). Using orthogonal velocity to distinguish the two currents can be difficult due to the transient nature of the NIJ and sEGC. Below, the Lagrangian particles help us understand the pathways and variability of the two currents.

Besides the equatorward currents, there are two regions with mean poleward velocity. One is the NIIC on the Iceland shelf that carries warm subtropical-origin water into the Nordic Seas. The other is a weak flow on the Iceland slope that Harden et al., 2016 attributed to a signature of recirculation of water that previously passed through the section. The model orthogonal velocities are consistent with these observations (Figure 2.2 panels (e) and (f)), and the model Lagrangian particle trajectories confirm the recirculation (see section *b*

below).

2.3.1.2 Comparison with float and ship data

Figure 2.3 shows a comparison between data from the shipboard CTD survey on the release date of the RAFOS floats with the model results. The CTD survey took place on 12-Jul-2014 and 13-Jul-2014. As the observations comprise a single snapshot in time, in order for the comparison to be relevant, the mean potential temperature and salinity in the month of July from the model is used. The CTD data is also compared with daily snapshots in the month of July from the model (not shown), and no significant difference with the mean section was observed. The depth and overall structure of the isopycnals in the model are similar to the observations. The deepening and shoaling of 28.05 kg m^{-3} isopycnal varies in daily snapshots, but the average depth of the isopycnal is consistent with the observations. The surface temperature along the section is also consistent. East of 17°W the water column temperature and salinity structure are in good agreement with the data, but the model is slightly fresher. However, the subsurface temperature and salinity near the Greenland shelf from 50 to 380 m depth is higher by 1.15 ± 0.77 °C and 0.4 ± 0.27 in the observations. Between 380-750 m, which includes the depth range where the floats are released, the model agrees well with the observations.

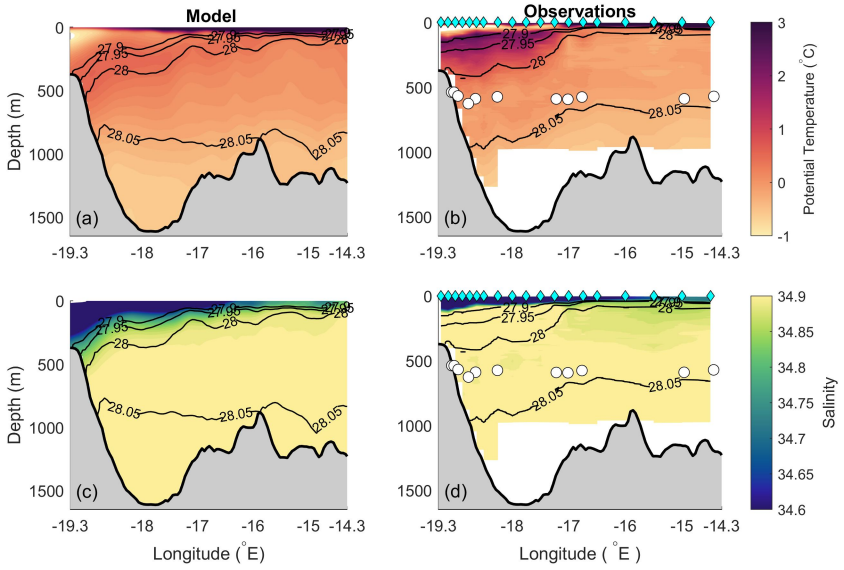

Figure 2.3: Comparison of hydrographic properties at 70°N from model (a) and (c) with CTD section (b), and (d) surveyed in July 2014 at the RAFOS float release date. The model vertical section is the mean of July 2008. The station positions along the section are marked by cyan diamonds. Isopycnals are shown with black contours. The release position along the section and depth of the RAFOS floats considered in this study are marked by white circles. Note that all of the floats are located deeper than 500 m.

In order to determine how the hydrographic properties evolve in time, we also compare the model with observations in a Lagrangian framework. A set of 400 particles seeded at 70° N are tracked forward in time in isobaric mode at 600 m depth. This mimics the constraint placed on the RAFOS float trajectories listed in Table 2.1. The depth of 600 m is used because it is close to the average depth of the floats (560 m). Figure 2.4 shows the float trajectories and simulated Lagrangian particle trajectories and the evolution of temperature and pressure along these paths. The RAFOS trajectories are compared with the modeled particle trajectories for 139 days during the same time of the year from mid-July to the end of November, which was the last

day at which the model outputs are available.

Table 2.1: RAFOS float information, namely the: float ID number, initial pressure (dbar), launch date (dd-mm-yyyy) and position (°N and °W), end date and position, and remarks. The float that was grounded in the Iceland Sea is marked as "Ground". The floats that surfaced within the Iceland Sea are marked "IcS". The floats that surfaced within the Labrador Sea are marked "LS". One float surfaced in the Irminger Sea, marked as "IrS".

Float ID	Pres $(dbar)$	$Date_{start}$ (dd-mm-yyyy)	Lat_{start} $(°N)$	Lon_{start} $(°W)$	$Date_{end}$ (dd-mm-yyyy)	Lat_{end} $(°N)$	Lon_{end} $(°W)$	Remarks
1208	542	12-07-2014	70	19	29-05-2015	63.13	54.35	LS
1209	542	12-07-2014	70	19	29-05-2015	62.56	58.66	LS
1287	592	13-07-2014	69.99	16.76	29-05-2015	66.88	11.95	IcS
1288	572	13-07-2014	70	15	29-05-2015	66.88	11.02	IcS
1291	591	13-07-2014	69.99	18.62	29-05-2015	66.6	9.52	IcS
1293	595	13-07-2014	70	17.01	29-05-2015	66.25	10.93	IcS
1294	579	13-07-2014	69.99	17.76	29-05-2015	67.92	15.84	IcS
1297	569	13-07-2014	70	18.88	29-05-2015	64.68	34.39	IrS
1298	630	13-07-2014	70	18.75	29-05-2015	67.35	23.57	Ground
1301	576	13-07-2014	69.99	18.24	29-05-2015	59.80	55.18	LS
1302	593	13-07-2014	70	17.25	29-05-2015	67.87	15.21	IcS

The observed float trajectories are within the range of the modeled particle trajectories. The EGC is visible in both the observed and modelled particle trajectories. The model particles also reveal a northward flow offshore of the EGC. This pathway is due to intermittent eddies visible in the Eulerian velocity field at 600 m depth, which was not likely to be captured by only the two floats released close to it. In Figure 2.4 (a) and (b), the evolution of temperature and pressure for the 11 selected floats are shown. The $\mathcal{O}$(100m) spikes in one float's (RFS1209) pressure record occurred when that float was traveling along the east slope of Greenland, embedded in the EGC (Figure 2.4 (b)). These pressure excursions are coincident with the float measuring warmer temperatures ($\sim$ 0.5°C warmer, Figure 2.4 (a)), and were likely due to the float being pushed up-slope by strong upwelling. Evidence of up-slope excursions, measured by other floats included in the complete RAFOS data set, were found in other locations in the Iceland Sea, and most prevalent along the northwest slope of Iceland (Jong et al., 2018). Some of the float temperature measurements fall within the envelope of model particle temperatures. However, some others are colder than model particles by 0.1 ± 0.045°C, which is well within the range of observed interannual variability (Lauvset et al., 2018). The RAFOS floats were not equipped with conductivity sensors; therefore, salinity evolution along the float trajectories is not possible.

2.3.1.3 Comparison at the Látrabjarg section and Evidence of Dense water on the Iceland shelf

The fidelity of the model has already been studied at the Látrabjarg section by Almansi et al., 2017, who showed that the model hydrography resembles

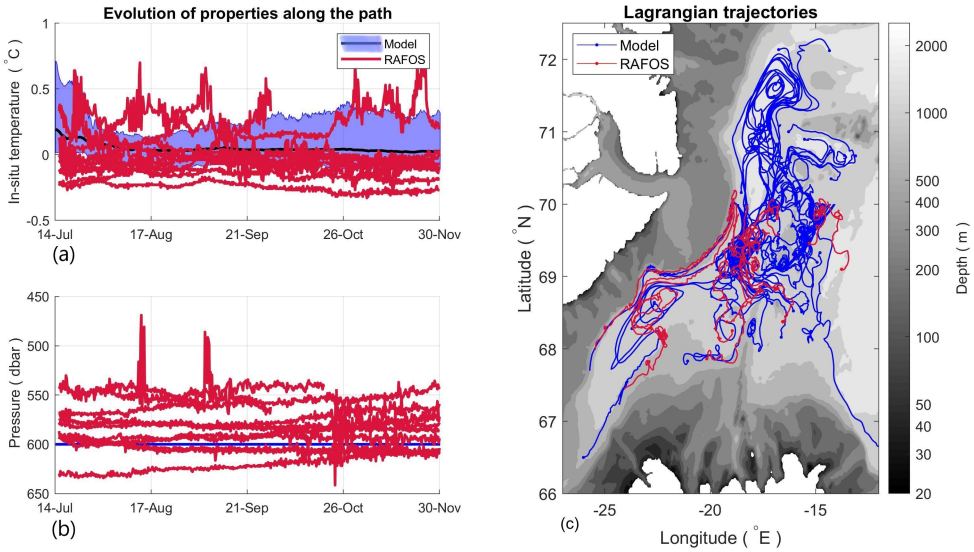

Figure 2.4: Evolution of (a) in-situ temperature and (b) pressure of model Lagrangian particles and RAFOS floats. The blue shade shows the 5th and 95th percentile ranges of the particle temperatures. The solid black line shows the mean particle temperature. The red lines show the RAFOS float time series. All the modeled particles are confined to 600 m depth (the blue line in panel (b)). (c) Lagrangian trajectories of the model particles (blue) and the RAFOS floats (red). Only 50 model trajectories are shown.

shipboard CTD observations between 1990 and 2012 at Látrabjarg (Figure 4 in Almansi et al., 2017). That study concluded that the model captures all of the major currents (the NIIC, the NIJ, and the EGC) along the section. The hydrographic structures are shown to be consistent with the detailed observational studies performed by Mastropole et al., 2017 at Denmark Strait. The comparison by Almansi et al., 2017 was focused on the western side of the Denmark Strait where the bottom intensified DSO is located. The DSO is the dense ($\sigma_\theta \geq 27.8$ kg m^{-3}) southward flow banked against the Greenland side of the trough in Denmark Strait. However, observations show evidence for the existence of dense water (satisfying the DSO density criterion) on the Iceland shelf occasionally in winter (Våge et al., 2015).

In Figure 2.5 the model-mean section in February is compared with observations from February 1997. They both show steep isopycnals from 27.6 to 27.8 kg m^{-3} on the Iceland shelf. The 27.8 kg m^{-3} isopycnal on the Iceland shelf lies further westward in the model than the observations by approximately 70 km, and it continues through the trough and changes slope on the Greenland side. The same isopycnal structure is evident from the observations but for the 27.6 and 27.7 kg m^{-3} isopycnals. The continuity of isopycnals from the Iceland shelf to the trough is seen from January to March in the model with the isopycnals being steep and outcropping to the surface by the end of February and early March. The model shows biases in the surface salinity (about + 0.1 or less) which could be the potential reason why the dense water at the shelf appears to occupy a larger area than the observations. The dense water on the Iceland shelf has been observed in other years as well, however it is sparse in

winter.

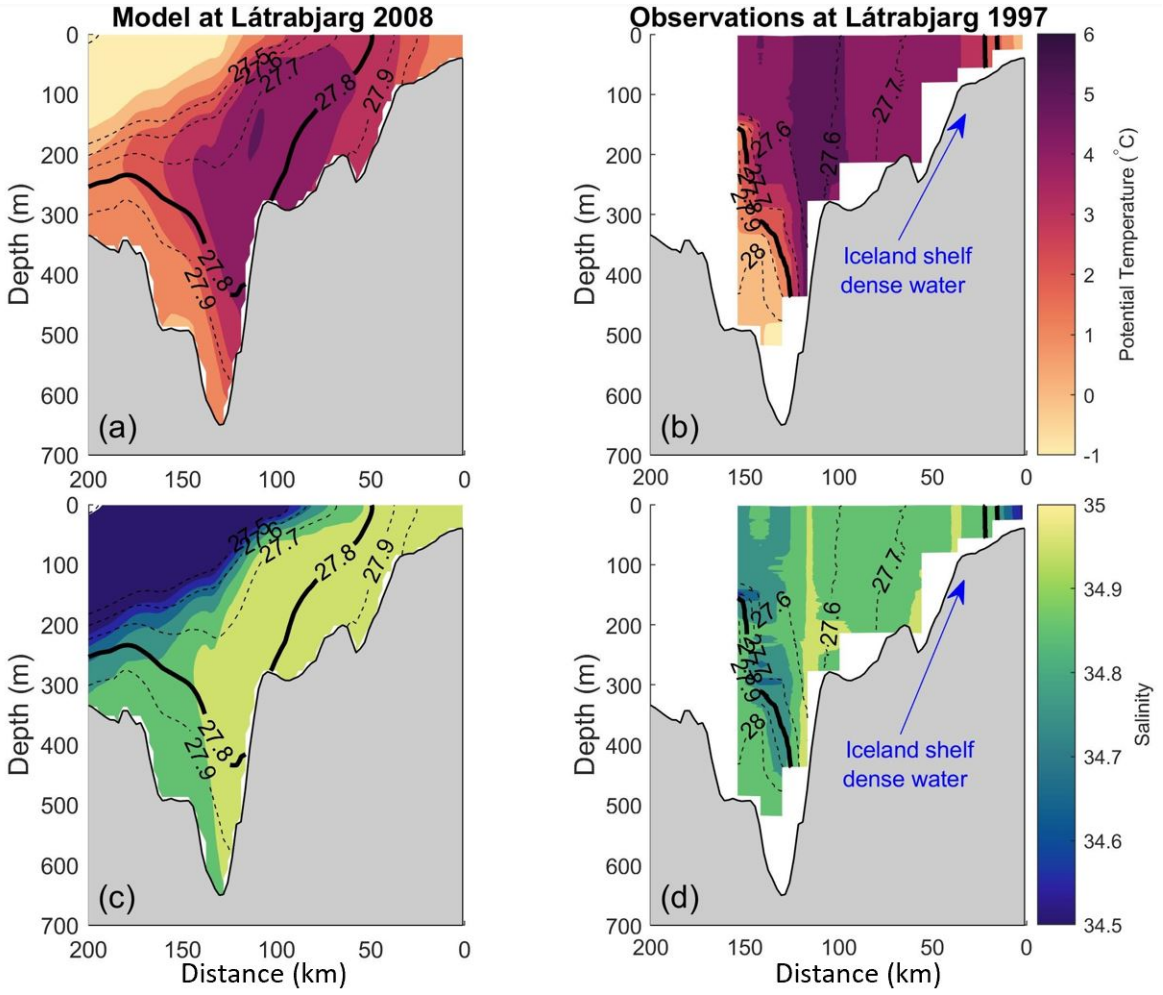

Figure 2.5: Comparison of hydrographic properties from model (a) and (c) with CTD sections (b) and (d) surveyed in February 1997 at the Látrabjarg section (see Figure 2.1). The model vertical section is the mean of February 2008. The February 1997 is selected as the observational evidence for the dense water on the Iceland shelf. Isopycnals are contoured in black. The 27.8 kg m^{-3} isopycnal is highlighted by the bold black contour. The Iceland shelf dense water in the observations is annotated by the arrows.

Our exploration of the Unified Database for Arctic and Subarctic Hydrography (Behrendt et al., 2017), World Ocean Database (WOD, 2013), and International Council for the Exploration of the Seas (ICES, 2006) database

revealed that out of 3700 individual profiles near the Iceland shelf (within about 100 km periphery of Iceland's west coast) spanning from 1980-2018, about 800 of them were collected in the winter (JFM). Despite the limited winter observations, 20 out of 200 profiles show the dense water ($\sigma_\theta \geq 27.8$ kg m^{-3}) on the shelf along Látrabjarg section (in depths shallower than 230 m). These 20 profiles are spread over the years 1981-1984, 1990, 1993, and 1995 which have relatively high North Atlantic Oscillation (NAO) index.

2.3.2 Backward tracking of particles released at Látrabjarg

To determine the near-field origins and pathways of the DSO, passive particles are released at the Látrabjarg section at the end of each month from 30-Nov-2007 to 31-Oct-2008. There is an ensemble of twelve particle release experiments (see Table 2.2). Each ensemble member is tracked backwards in time for three months in three-dimensional space. This length of time was chosen because it is the shortest time period at which the geographical distribution of pathways, the watermasses and properties of the DSO sources can be identified. We explored backtracking of longer time-period (4,5, and 6 months) to be sure 3 months was an appropriate time-scale. The particle seeding resolution is 0.5 km in the horizontal and 25 m in the vertical direction. All particles are seeded below the 27.8 isopycnal satisfying the conventional overflow threshold in the literature, which we refer to as dense particles (see Table 2.2). The total number of backward tracked dense particles over all ensemble members is 18399.

Table 2.2: Particle information, namely the: release ID, release date at Látrabjarg section, date at 90 days prior to reaching the Látrabjarg section (date at the origin), date 30 days after passing the Látrabjarg section (date at the end), the number of particles that have $\sigma_\theta \geq 27.8$ kgm^{-3} (dense particles), and the number of particles that eventually end up south of the Denmark Strait (DSO particles).

Release ID	Release Date at Látrabjarg	Date at the origin	Date at the end	Dense particles #	DSO particles #
I	30-Nov-2007	01-Sep-2007	30-Dec-2007	514	466
II	31-Dec-2007	02-Oct-2007	30-Jan-2008	856	773
III	31-Jan-2008	02-Nov-2007	01-Mar-2008	1800	1041
IV	29-Feb-2008	01-Dec-2007	30-Mar-2008	2442	1694
V	31-Mar-2008	01-Jan-2008	30-Apr-2008	2024	1006
VI	30-Apr-2008	31-Jan-2008	30-May-2008	1852	1225
VII	31-May-2008	02-Mar-2008	30-Jun-2008	1508	1120
VIII	30-Jun-2008	01-Apr-2008	30-Jul-2008	1341	1153
IX	31-Jul-2008	02-May-2008	30-Aug-2008	1791	1427
X	31-Aug-2008	02-Jun-2008	30-Sep-2008	1647	1380
XI	30-Sep-2008	02-Jul-2008	30-Oct-2008	1726	1612
XII	31-Oct-2008	02-Aug-2008	30-Nov-2008	898	811

The backward tracking alone does not reveal what fraction of the dense water eventually cascades over Denmark Strait. Therefore, each ensemble member is also advanced forwards for 30 days. Particles that appear south of Denmark Strait after 30 days are considered to have participated in the DSO, regardless of their final density. The total number of these so-called DSO particles is 13708, which is 74.5% of all the dense particles. It is found that the ratio of the DSO to the dense particles varies between ensemble members. The information about each ensemble member is listed in Table 2.2. Notice that although the number of dense particles is highest in February and March, the number of DSO particles does not increase proportionally. In fact, the ratio of the DSO to the dense particles decreases in March. This is because the Irminger Current is colder in winter and spring (by 1.8 °C, Mastropole et al. 2017), and becomes denser as it moves northwards until some of it satisfies the $\sigma_\theta \geq 27.8$ kg m^{-3} criterion. This dense water continues northward and mixes with surrounding water, namely the southward flowing EGC and NIJ, and some fraction of it cascades over Denmark Strait within 30 days. This splitting and retroflection of the Irminger Current in the vicinity of the Denmark Strait was demonstrated by Valdimarsson and Malmberg, 1999 and discussed in Rudels et al., 2002 as well. However, in that study, the location of the splitting was not fully identified. The Lagrangian trajectories in the following section reveal the time-varying location of this bifurcation. For the rest of the paper, the DSO particle trajectories and hydrographic properties are discussed; studying the properties and pathways of dense water that does not cascade over the Denmark Strait (the difference between columns 5 and 6 in Table 2.2) is beyond the scope of this research.

The backward trajectories of the DSO particles reveal different sources for the DSO. Figure 2.6 (a) shows the geographical distribution of the particles three months before reaching the Látrabjarg section, at their origin, color coded by ensemble member (see also Table 2.2). The DSO particles come from both north and south of the Denmark Strait, with 83.6% originating from the north. The geographical distribution of the DSO particles at their origins are nearly identical throughout the year between all ensemble members, but the fractions from north and south of the sill vary. To study this variability for each ensemble member, the DSO particles are categorized into different subsets, based on geographical origin. They are naturally broken down into the northern- and southern-origin subsets. The southern origin subset is further separated into two groups, depending on whether they arrive at the Icelandic side of the Látrabjarg section east or west of 26.5°W (star marker on Figure 2.6 (a)). Figure 2.6 (b) shows the variation in the fraction of the DSO particles flowing from the north (abbreviated as N), the south and west of 26.5°W (abbreviated as S), and the south and east of 26.5°W, on the Iceland shelf (abbreviated as ISh) for each ensemble member. In summary, the DSO particles are categorized into N, S, and ISh subsets based on where they originate. The trajectories and properties of the particles in each individual subset are now discussed in detail.

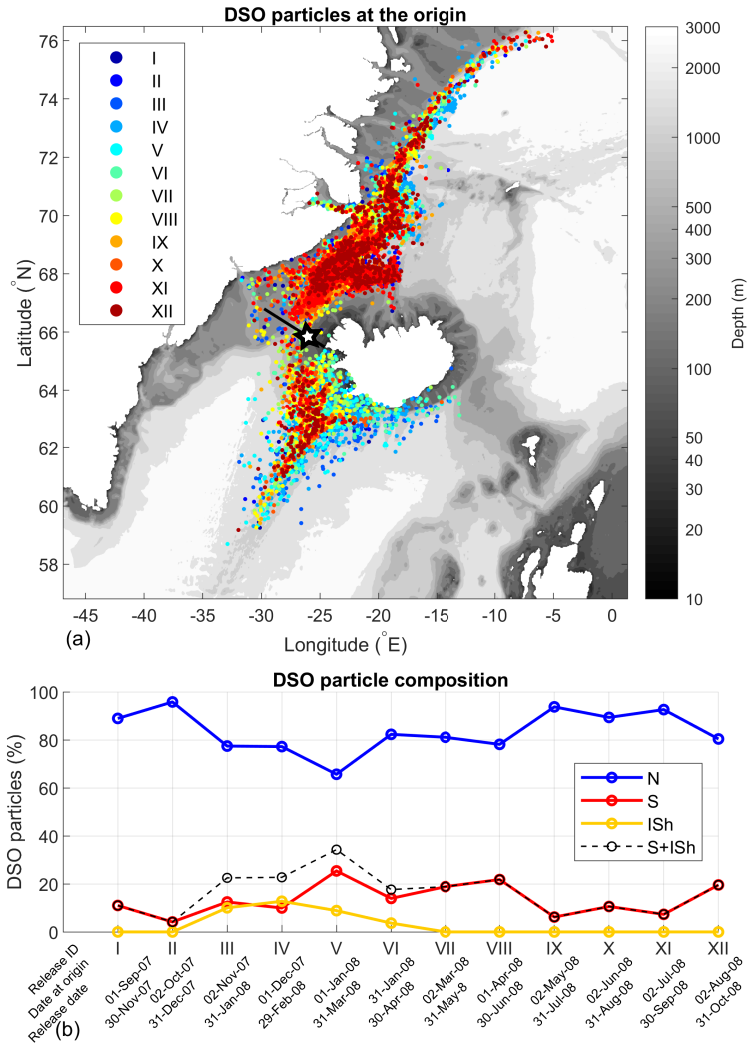

Figure 2.6: (a) The geographical distribution of the DSO particles at their origins color coded by ensemble member ID. (b) The fractions of the DSO particles in each subset. The fractions are variable for each ensemble member. N, S and ISh in the legend mark the north (blue), the south and west of 26.5° W (red) and the south and east of 26.5° W on the Iceland shelf (yellow) subsets, respectively (see Figure2.15 for the subsets). The 26.5° W is marked with the star. The dates at the origin and the release dates at Látrabjarg are shown below the abscissa. The total contribution from the south is highest for release V.

The fraction of the DSO particles from the south (S + ISh) which is persistent throughout the year, is highest at the end of March (ensemble member V), with a mean contribution of 16.3 %. The contribution from the ISh subset is present only between December 31st to April 30th (ensemble members III, IV, V, and VI) with a peak of 12.8% of DSO particles at the end of February. The depth-longitude positions of the DSO particles at the Látrabjarg section can be seen in Figure 2.7, color coded by the origin subsets. Note that the S and N subsets both occupy the western side of the section and the ISh subset, separated from the others, occupies the eastern side of the section. The presence of DSO particles in depth-longitude space is consistent with the observations of dense water at the Látrabjarg section, discussed earlier (Figure 2.5).

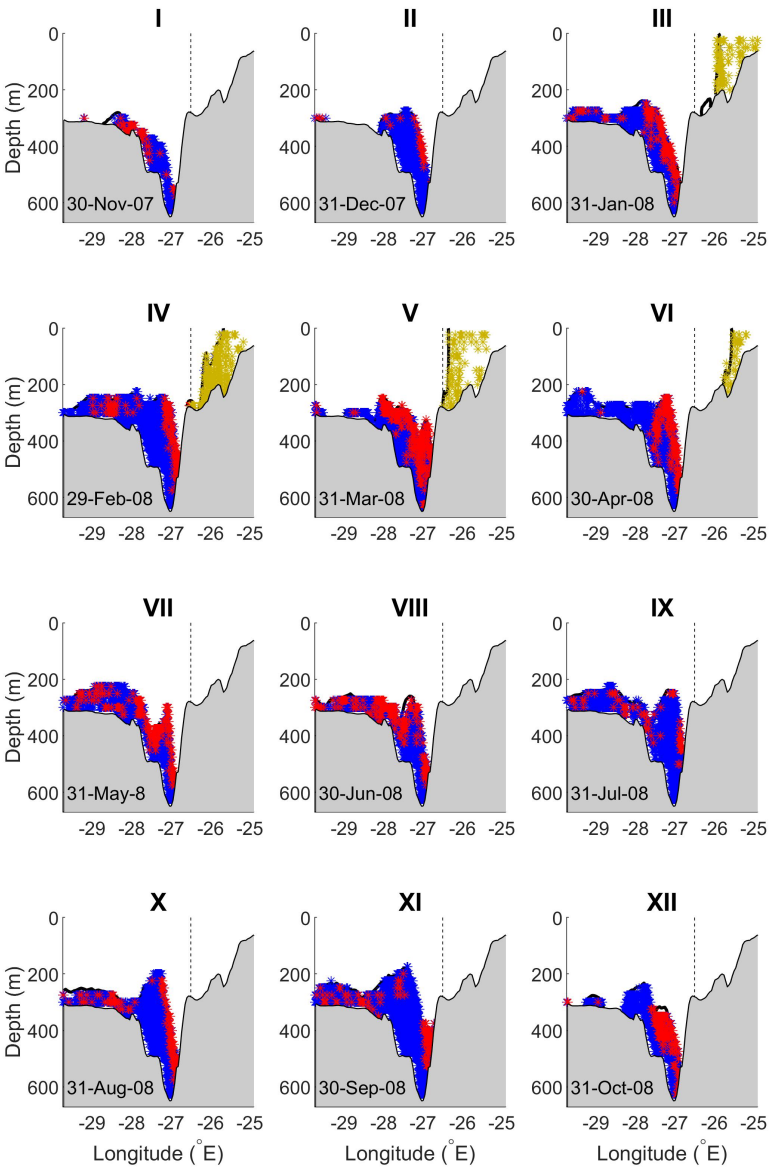

Figure 2.7: Depth-longitude distribution of the DSO particles at the Látrabjarg section. The particles are color coded by the origin subsets for each ensemble member as in Figure 2.6 (b) (particle trajectories in N, S, and ISh subsets are colored in blue, red and yellow). For clarity, the release dates of particles at the Látrabjarg section are shown (also see Table 2.2). The 27.8 kg m^{-3} isopycnal is highlighted by the bold black contour. The vertical dashed lines at 26.5° W separate the ISh subsets from the the rest of the south particles (the S subsets) for each ensemble member.

The DSO particles are tracked backwards from their release point at the Látrabjarg section. However, for the sake of visualization, analysis, and discussion their trajectories are plotted forward in time to the Látrabjarg section. Figure 2.8 shows the trajectories of the DSO particles approaching Denmark Strait. To avoid clutter, instead of plotting the full trajectories of individual particles, 10 day long pathlines of every 5th DSO particle in each subset are plotted. The visualized trajectories are representative of trajectories of all the DSO particles. Note that, not all the DSO particle trajectories at all times look like the trajectories in Figure 2.8 (see the supplementary animations). The northern pathway (in blue) is present in all months. The DSO particle trajectories in subset N depict the conventional route of the DSO along the east Greenland shelf break; that is, the EGC. The bifurcation of the EGC is also evident from the trajectories (and better visualized in the animations): sometimes the separation takes place north of the Kögur section ($\approx 68^{\circ}$N in ensemble members I, IV, VI, and IX), and other times the separation takes place south of it within the southern part of the Blosseville Basin ($\approx 67^{\circ}$N in ensemble members V and VIII).

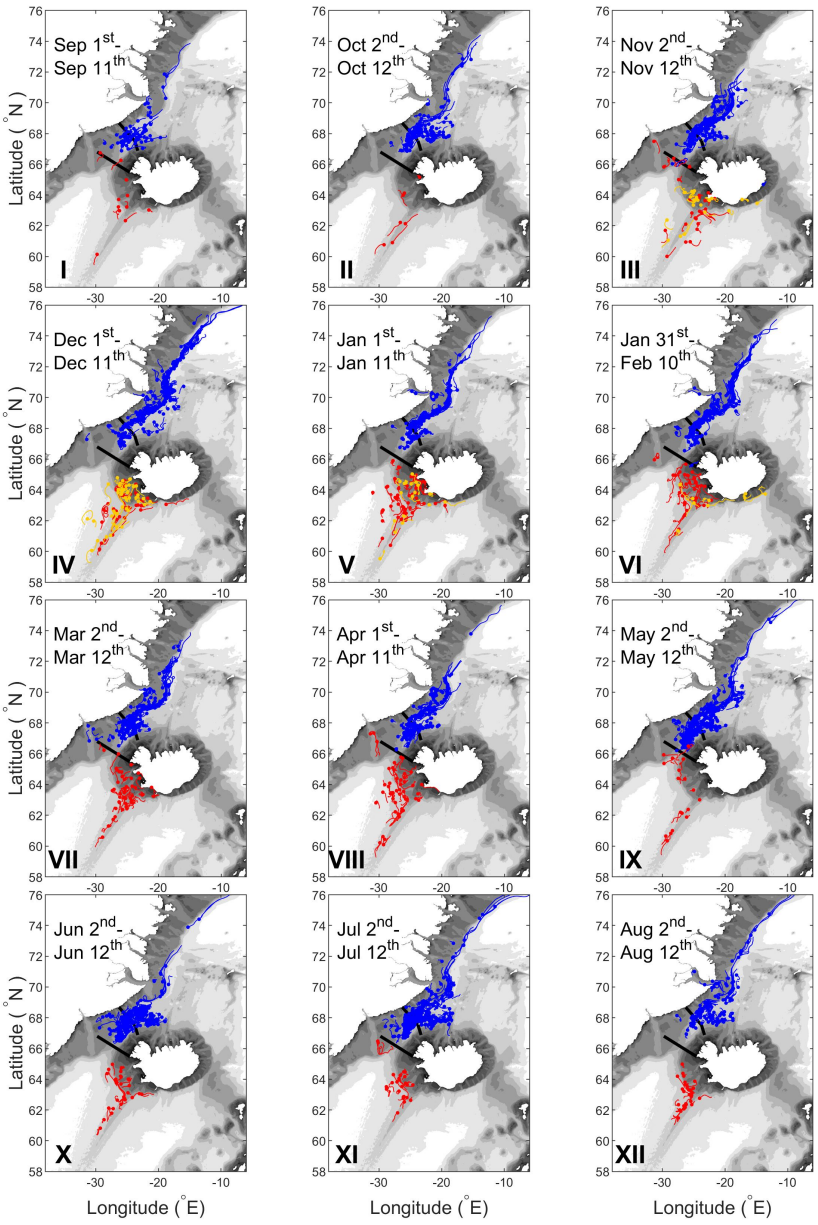

Figure 2.8: The upstream trajectories of every 5th DSO particle in each subset moving toward the Látrabjarg section. Trajectories are plotted as pathline segments trailing behind particle markers for 10 days. The top date on each subplot shows the date at the origin (see also Table 2.2, column 3). The bottom date shows the date when particles are at their marker location. The faster the particles move, the longer are their tails. The particles are color coded by the origin subsets for each ensemble member as in Figures 2.6 (b) and 2.7 (see also the supplementary animation).

The particle trajectories show that the separation from the EGC takes place in multiple locations along the east Greenland shelf (mostly south of $\approx 70^{\circ}$N). The trajectories of DSO particles in the N subset show that sometimes the bifurcated branches reunite with the EGC (e.g. in ensemble members III and IX), and other times they shift to the middle of the basin and continue south. Concurrently, the NIJ is evident from the Lagrangian particle trajectories on the northwest Iceland slope: sometimes very close to the Kolbeinsey Ridge (e.g. in ensemble members I, IV, X, XI, and XI) and sometimes about 130 km southwest of the ridge, closer to the Kögur section (e.g. in ensemble members V-VII). The DSO particle trajectories also reveal that sometimes the sEGC swings toward the Iceland shelf, interacts with the NIJ and the two currents merge and continue south along the Iceland shelf. This interaction is clearly visible from the animations of particle trajectories, provided as supplementary material. Notice that, although the particles follow the currents, they do not necessarily stay in one current at all times. In other words, the Lagrangian trajectories are in principle distinct from the currents (velocity maxima). The separation from the EGC and its interaction with the NIJ is also observed by Våge et al., 2013. The interaction happens at different times and places along the path for each ensemble member. As the simulated trajectories cover only one year, detecting the sEGC and the separation frequency is hard; nevertheless, there is no strong evidence of seasonality. Besides, as discussed above, the sEGC appears to be intermittent.

The DSO particles in the S and ISh subsets have a similar spatial distribution at their origins for ensemble members III - VI (Figure 2.8). The majority of

particles in the ISh subsets, however, move along shallower isobaths (depth $\leq$ 300 m, Figure 2.12 (c)) than the particles in the S subsets (depth $\approx$ 400-800 m, Figure 2.11 (c)). Particles in both subsets flow northward toward the Denmark Strait. The particles in the S subset then encounter the southward flowing particles in the N subset, retroflect, and flow south again, to reach the western side of the Látrabjarg section. In contrast, the northward flowing ISh particles arrive at the eastern side of the Látrabjarg section and predominantly continue northwards with the NIIC. Most of these particles return south within 20 days of crossing the Látrabjarg section in the forward run. Figure 2.9 shows the particle trajectories at the end of the forward run for each ensemble member. The particles in the S and N subsets cascade over Denmark Strait and trace multiple recirculations in the Kangerdlugssuaq Trough. These cyclonic recirculations are also detected by Koszalka, Haine, and Magaldi, 2013. Finally, the recirculated particles continue to flow south along the east Greenland shelf following the traditional DSO path (Dickson and Brown, 1994). Similarly, the particles in the ISh subsets cascade over Denmark Strait but with a time lag of about 20 days compared to the other subsets. They then follow a similar path to the particles from the N and S subsets. Notice that very close to the Látrabjarg section immediately before and after cascading the Denmark Strait, the particles from all subsets follow nearly identical pathways. If the particles of each subset were not color coded differently, they would be indistinguishable. Here, the backward Lagrangian particle tracking elucidates the origins and trajectories of the DSO even in the regions of high mixing.

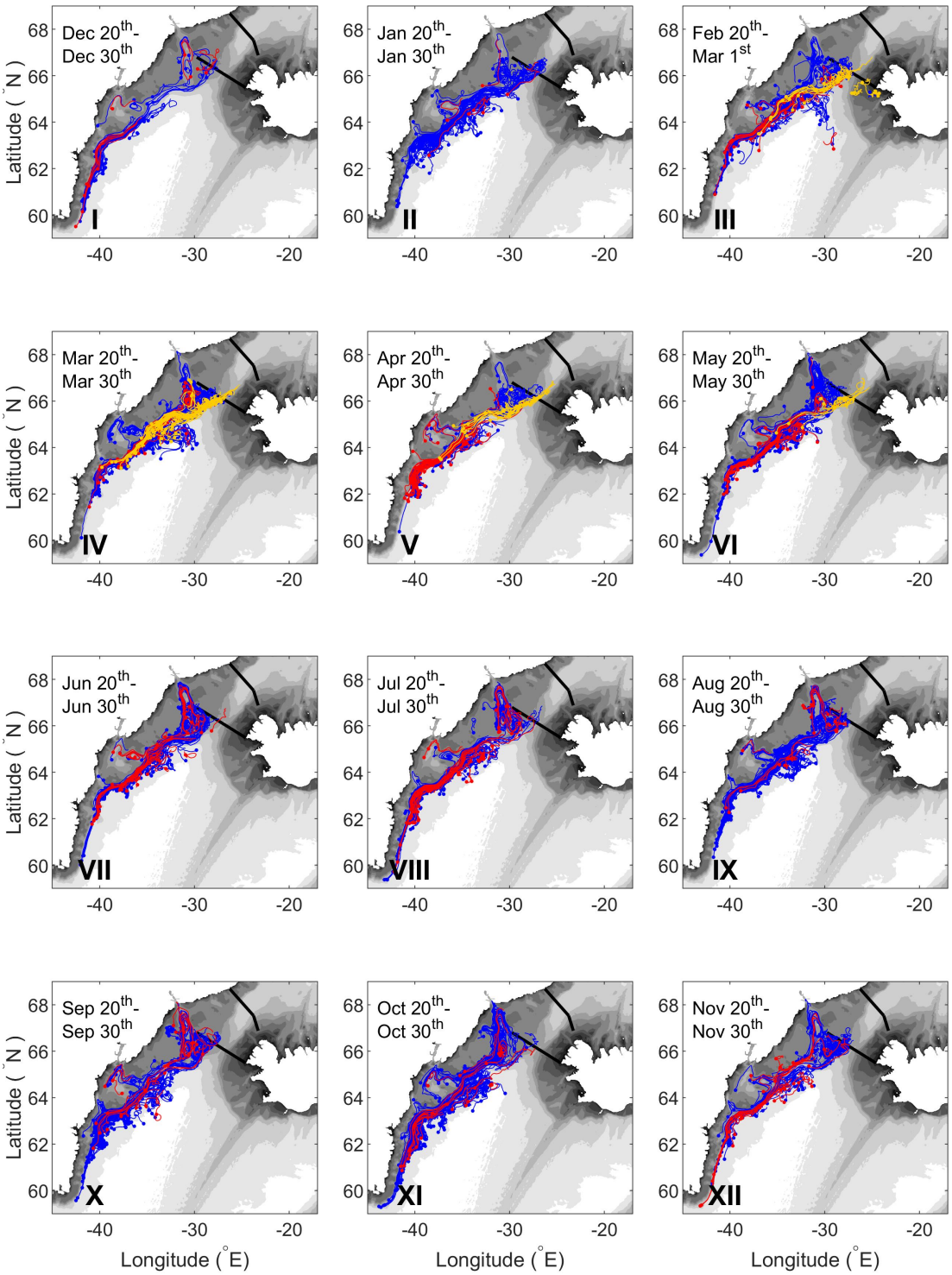

Figure 2.9: As Figure 2.8 except after passing the Látrabjarg section.

The evolution of hydrographic properties of DSO particles in the N, S, and ISh subsets are shown in Figures 2.10, 2.11, and 2.12, respectively. The mean temperature and salinity of the DSO particles in the N subset over all ensemble members (dash-dotted black lines) are nearly constant, with a slight increase ($\Delta\overline{T} = 0.4°$C, $\Delta\overline{S} = 0.05$) approaching the Denmark Strait sill (from -90 to 0 days). After cascading there is an increase in their temperature ($\Delta\overline{T} = 1.2°$C) and salinity ($\Delta\overline{S} = 0.1$) due to entrainment of the surrounding warmer and saltier watermass. The range of temperature before cascading is narrower (-0.11 °C to 2 °C) and it gets wider after cascading the Denmark Strait (1 °C to 4.5 °C). The range of salinity however, is wider at the origin (34.3 to 34.9) and narrows approaching the Denmark Strait and after the cascade (34.7 to 35). The abrupt change is also evident in their potential density and depth. The DSO particles' mean potential density is nearly constant (less than 0.06 kg m^{-3} increase along the path) with the value of $\overline{\sigma_\theta} \approx 27.9$ kg m^{-3} from the origin until they reach the Denmark Strait. After cascading, their mean potential density decreases by about 0.15 kg m^{-3}. The depth of the DSO particles is also nearly constant approaching the Denmark Strait and they sink (900 m on average) as they cascade over the cataract. Notice that the DSO particles in ensemble members VI - IX are shallower than particles in ensemble members I - V at their origin and along their path to the Denmark Strait, but after cascading the DSO particles in all ensemble members experience similar initial deepening at least for the first fifteen days (from approximately 360 m to 1000 m).

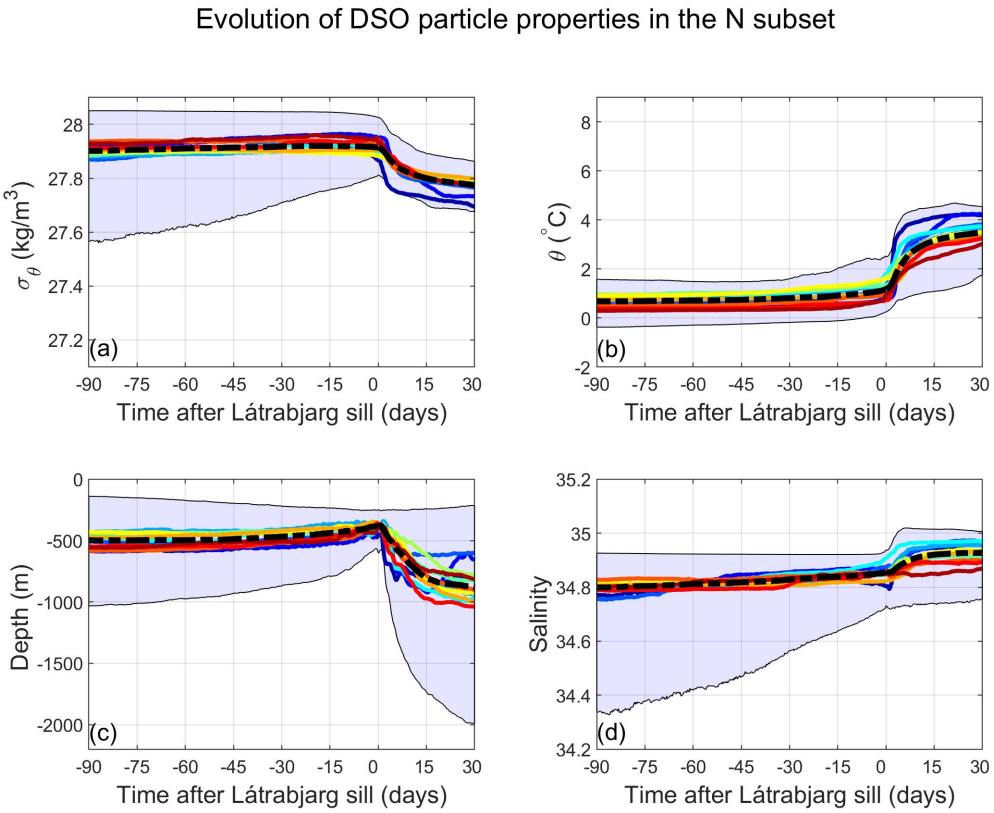

Figure 2.10: The temporal evolution of (a) potential density, (b) potential temperature, (c) depth, and (d) salinity of the DSO particles in the N subset color coded by ensemble member (see Figure 2.6 (a)). The shading in each subplot marks the 5th and 95th percentiles of the DSO particle properties over all ensemble members. The individual colored solid lines show the mean properties for each ensemble member (consistent with the color codes in Figure 2.6 (a)). The black dash-dotted lines show the mean properties over all ensemble members. The abscissa shows the time line for the particles from the origin moving toward the Látrabjarg sill section (days 0) and after crossing it.

The properties of the DSO particles in the S subset evolve differently (Figure 2.11). Initially, the particle properties are warmer and saltier than the DSO particles in the N subset at their origin location, but the S subset particles cool and freshen as they move toward the Denmark Strait. The rate of change

of temperature is steeper for the I - V ($\Delta\overline{T} = -3.51°C$) than for the VI - XII ensemble members ($\Delta\overline{T} = -2.35°C$) . The rate of change of salinity over all ensemble members is similar with an average of 0.15 decrease approaching the Denmark Strait from the origin. The DSO particles in the S subset are shallower and lighter at their origin in comparison to the DSO particles in the N subset but they rapidly densify while meeting the southward flowing DSO particles in the N subset (compare Figure2.10 (a) and (c) with Figure 2.11 (a) and (c)). After cascading, the DSO particles in the S subset have slightly higher average potential density (0.08 kg m^{-3}) than those in the N subset within the first 15 days after cascading. Ultimately, their properties become indistinguishable from the N subset. This is expected considering the intense mixing downstream of Denmark Strait shown earlier in Figure 2.9.

The DSO particles in the ISh subset exist only in winter, for ensemble members III - VI (Figure 2.12). They exhibit a similar cooling and freshening of their properties as the S subset, but the changes in their temperature happen at much faster rates. The cooling rate is more rapid for ensemble members III, IV, and V ($\Delta\overline{T} = -3.57°C$), and slower for ensemble member VI ($\Delta\overline{T} = -0.67°C$). The changes in the salinity are relatively small; the DSO particles in ensemble members III and IV slightly freshen ($\Delta\overline{S} = -0.03$) but those in ensemble members V and VI slightly salinify ($\Delta\overline{S} = 0.03$). The DSO particles in the ISh subset are generally shallower than the particles in the S subset (mean depth of 250 m) and they rapidly densify approaching the Denmark Strait. After crossing the sill (0 day) the DSO particles in the ISh subset still experience cooling, freshening and densification for approximately 15-20 days as opposed

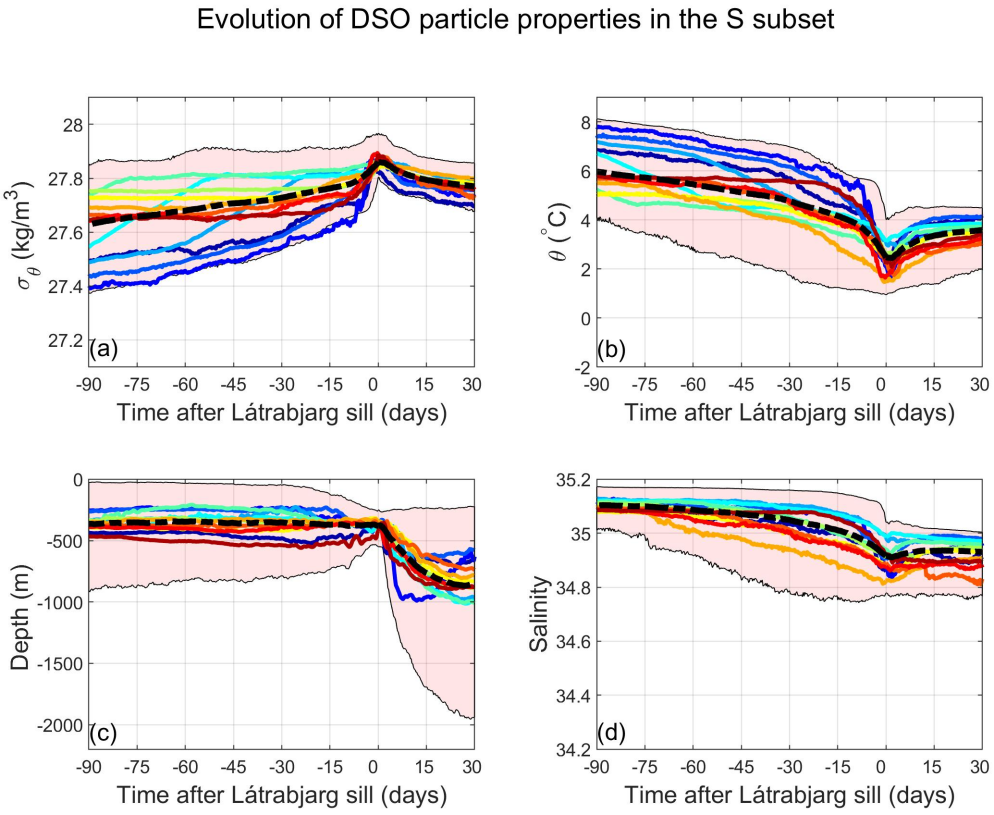

Figure 2.11: As Figure 2.10 but for the DSO particles in the S subset.

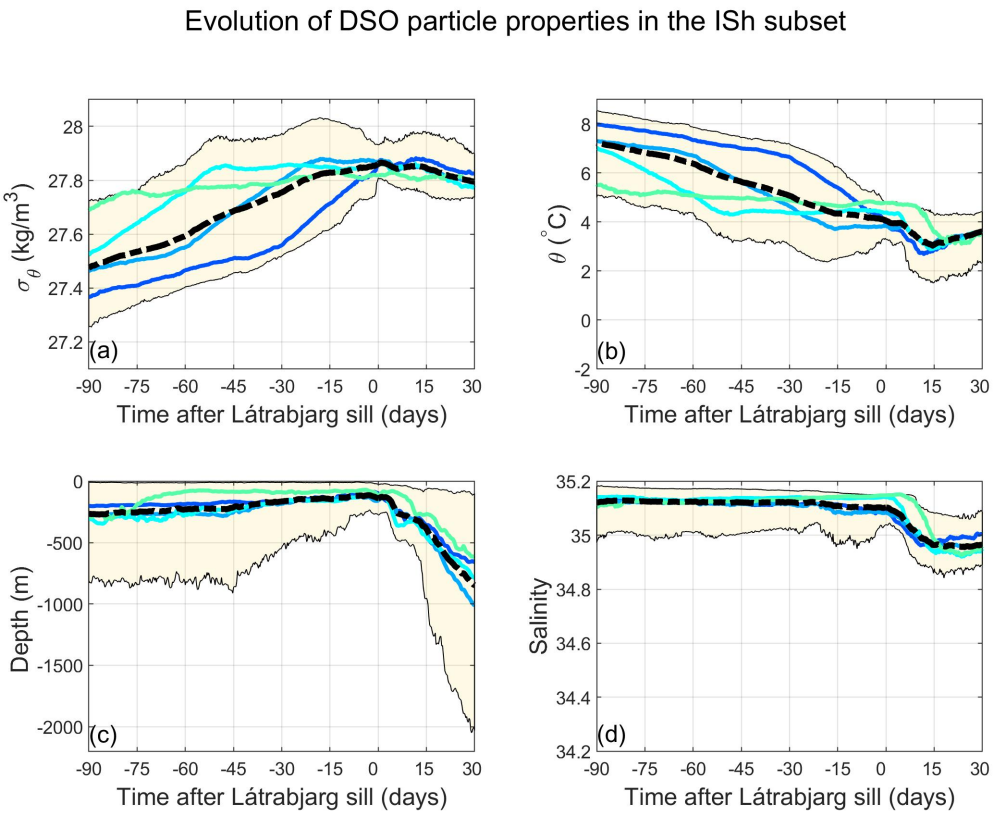

Figure 2.12: As Figure 2.10 but for the DSO particles in the ISh subset. Note that the particles in this subset are only present in ensemble members III - VI.

to the particles in the S subset. That is because the ISh subset particles still move northward along the shelf after crossing the Látrabjarg section and meet the southward flowing particles from the N subset, mix, and return south by cascading over the Denmark Strait within about 20 days of their forward run trajectories. Therefore, there is a lag in their property evolution with respect to the S and N subsets downstream of Denmark Strait.

In order to identify the watermasses that the DSO particles carry, their distribution in potential temperature-salinity (θ-S) space are plotted in Figure

2.13 for all ensemble members, color coded based on their origins. The θ-S diagrams represent the watermasses of the DSO particles at three different times: (a) at the origin, (b) at the release time at Látrabjarg, and (c) at the end point, 30 days after crossing the Denmark Strait. The DSO particles in the N subset at the origin (Figure 2.13 (a)) mark two hydrographic branches that indicate the conventional watermass end members observed north of Denmark Strait: the recirculated Atlantic Water, Polar Water, and Arctic Water (Harden et al., 2016). The particles in the ISh and S subsets contain the Irminger Water end member. These water masses are not distinguishable anymore at the Denmark Strait and further downstream (Figure 2.13 (b) and (c)).

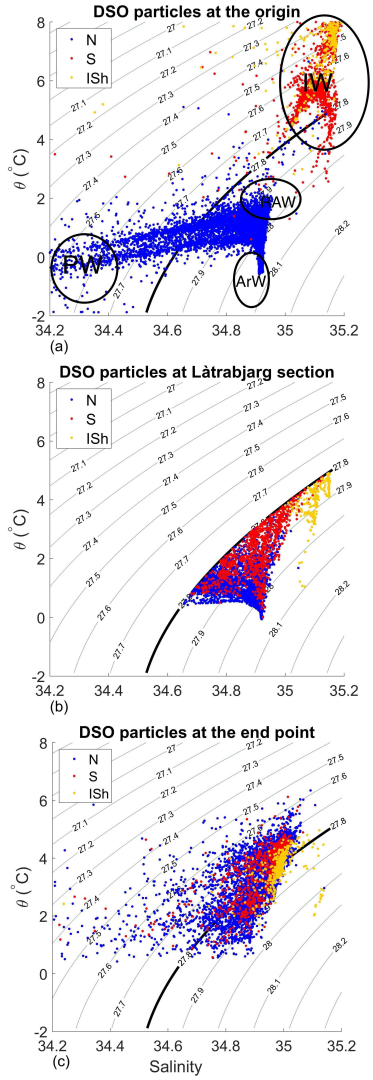

Figure 2.13: Potential temperature-salinity (θ-S) diagrams for all of the DSO particles in all ensemble members at (a) the origin, (b) the Látrabjarg section, and (c) the end point, color coded by their origin. The water masses marked in panel (a) are Irminger Water (IW), Recirculated Atlantic Water (RAW), Arctic Water (ArW), and Polar Water (PW). The 27.8 kg m^{-3} isopycnal is highlighted by the bold black line.

In order to identify when and where along the trajectories the watermass transformation takes place, the mean geographic location of the DSO particles in the latitude-longitude space as well as their mean trajectories in θ-S space

are plotted (Figure 2.14). The DSO particles in the N subset trace a short trajectory in θ-S space nearly along the 27.9 kg m^{-3} isopycnal from their origin to the Denmark Strait (Figures 2.14 (b), blue). This indicates that the changes in their properties are small (Figure 2.10 (a)). However, their trajectory (in θ-S space) after cascading the Denmark Strait is longer which means they have a larger and faster change of properties due to the mixing downstream of the Denmark Strait. The DSO particles' mean trajectory in the θ-S space crosses the 27.8 kg m^{-3} isopycnal and the DSO particles become lighter within 17 days after their cascade and continue to become more buoyant until the end of the simulation. As the N subset DSO particle trajectories are present both along the east Greenland shelf and west Iceland shelf, their mean geographic trajectories pass the middle of the Blosseville Basin, and after they cascade they continue along the east Greenland shelf.

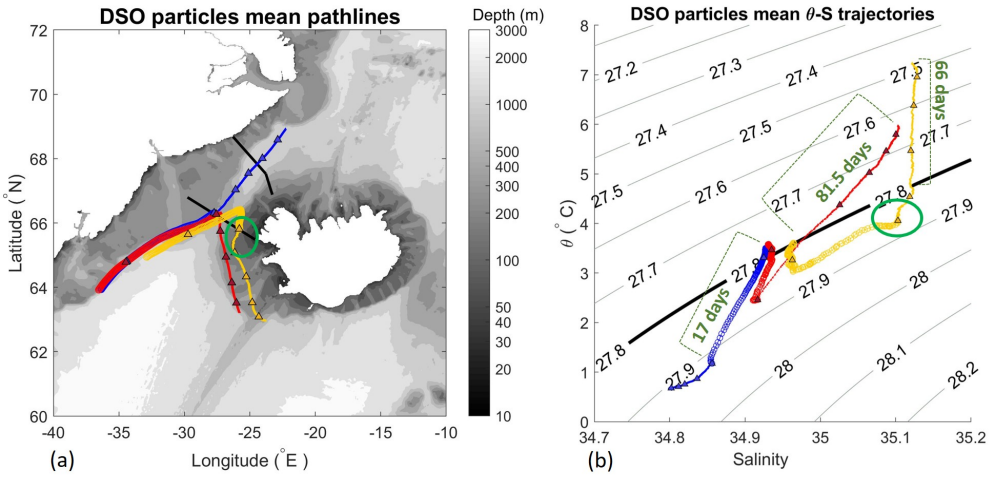

Figure 2.14: The mean DSO particle trajectories in (a) geographical space and (b) θ-S space. The trajectories are color coded by their origins. The marker size is smaller for each trajectory from the origin to the Denmark Strait and it is bigger after crossing the Látrabjarg section. The trajectories are annotated with time and every 20 days a triangle marker is added. The green circle marks the same timing both in geographical space and the θ-S space.

The DSO particles in the S and ISh subsets behave differently (Figures 2.14 red and yellow trajectories, respectively). The particles in the S subset cool and freshen along their trajectories from the origin to the Denmark Strait. They also densify until their potential density exceeds 27.8 kg m^{-3} approximately 9 days prior to reaching the sill. Their trajectories in θ-S space from the origin to the Denmark Strait are quite long, which implies that they experience a faster rate of change in their properties than the N subset particles. After the cascade, they experience a shorter mean trajectory in θ-S space and become slightly lighter until their properties as well as their spatial location converges to that of the N subset DSO particles.

While moving along the Iceland shelf, the DSO particles in the ISh subset keep their salinity constant and cool until they are densified enough to cross

the 27.8 kg m^{-3} isopycnal. This transformation takes place within 66 days of traveling from their origin to within about 50 km from the Denmark Strait. They still densify until they reach the Strait (green circle in Figure 2.14). Then they continue along the 27.85 kg m^{-3} isopycnal for 24 days until they cross the Látrabjarg section while flowing northward along the Iceland shelf. They still continue moving north (in geographical space) and along the 27.85 kg m^{-3} isopycnal (in θ-S space). The mean trajectory continues along that isopycnal even after cascading for about 10 days. Finally, the mean trajectories of the ISh subset of DSO particles converge to that of the N and S subsets both in geographical and in θ-S space. This reflects the mixing downstream (compare Figures 2.9 and 2.13 (b) with Figure 2.14). Note that the particles in the ISh subset, although starting as the shallowest, warmest and saltiest, become, after cascading, nearly as cold and fresh as the DSO particles in the N and S subsets.

2.4 Summary and Conclusions

In this paper we presented a detailed analysis of upstream sources and pathways of the DSO. To do so, we performed a Lagrangian analysis on the output of a high resolution ocean model to investigate the origins and pathways of the DSO. The model time period is from 01-Sep-2007 to 30-Nov-2008 and its outputs are evaluated by comparison with observations. This kinematic study gives a comprehensive understanding of the time-varying contribution to the overflow and evolution of previously identified northern pathways, i.e., the NIJ, the EGC, and the sEGC (blue curve in Figure 2.6 (b)). It also reveals an

additional pathway from south of the Denmark Strait which contributed to the DSO. This southern pathway itself is divided into two subsets, depending on whether the Lagrangian particles arrive at the sill east or west of 26.5°W. Those that arrive to the east of 26.5°W are shallower than 300 m and are present only during the winter. The average contribution from the south is 25.8% during the winter (JFM) of 2008, which has a relatively high NAO index. The entrainment south of Denmark Strait suggested by the literature, (e.g. cold entrainment of the northward Labrador Sea Water (McCartney, 1992), and warm entrainment of Irminger Current (Appen et al., 2014) into the overflow at mid-depth and further south of the sill) are different from the southern pathways we discovered. This sub-surface southern pathway could potentially mark a shortcut for northward-flowing waters that densify and turn around to cascade over the Denmark Strait and eventually feeding the NADW. Although observations show evidence for the existence of the dense water on the Iceland shelf (Figure 2.5, Våge et al. 2015) as well as presence of Irminger Water in the deep overflow (Mastropole et al., 2017), these southern pathways need more confirmation from observations. Future studies will benefit from models that incorporate coastal runoff on the Iceland shelf, and are several years long to account for interannual variability and to elucidate the relevance of these southern pathways in a changing climate.

The evolution of hydrographic properties of particles from each subset were also presented. The northern origin DSO particles (N subset) transform to become warmer, saltier and slightly less dense, but the southern origin DSO particles (S and ISh subsets) transform to become colder, fresher and denser

along their path to the Denmark Strait. The DSO particle properties in all subsets converge after cascading over the Denmark Strait (Figure 2.13 (b) and (c)), and they have overlapping pathways (Figure 2.9). Therefore, watermass analysis would not be able to discern the DSO sources at the Látrabjarg sill section or south of it. This study shows that the combination of backtracking and along-track watermass analysis can locate the watermass transformation sites continuously along the pathways (Figure 2.14). In this way both time evolution and spatial distribution of pathways are required to determine the *origins* of the DSO water masses (see the introduction).

Finally, the schematic of the overflow water is updated by incorporating direct pathways of the DSO (Figure 2.15). The circulation schematic shows that the separation from the EGC happens at multiple locations and it is intermittent. The DSO particles represent a clear distribution of pathways but they do not necessarily stay in one current (i.e. EGC, sEGC, and NIJ) at all times. Therefore, they do not indicate the currents, but rather trajectories of the particles. The particle pathways did not reveal an enduring source for the NIJ to the east of Kolbeinsey Ridge, but some particles show an intermittent eastern pathway (marked by dashed blue line in Figure 2.15). The particle trajectories clearly marked the NIJ pathway from the north and west of Kolbeinsey Ridge toward Denmark Strait (e.g. Figure 2.8, ensemble members II, IV, XI and XII). This is similar to what was observed with the RAFOS floats (Jong et al., 2018). We also see the core of the NIJ to the east of Kolbeinsey Ridge in the model mean Eulerian velocity field, consistent with Semper et al., 2019. Therefore, it is possible that an eastern source would be found if the Lagrangian simulation

was multi-years long.

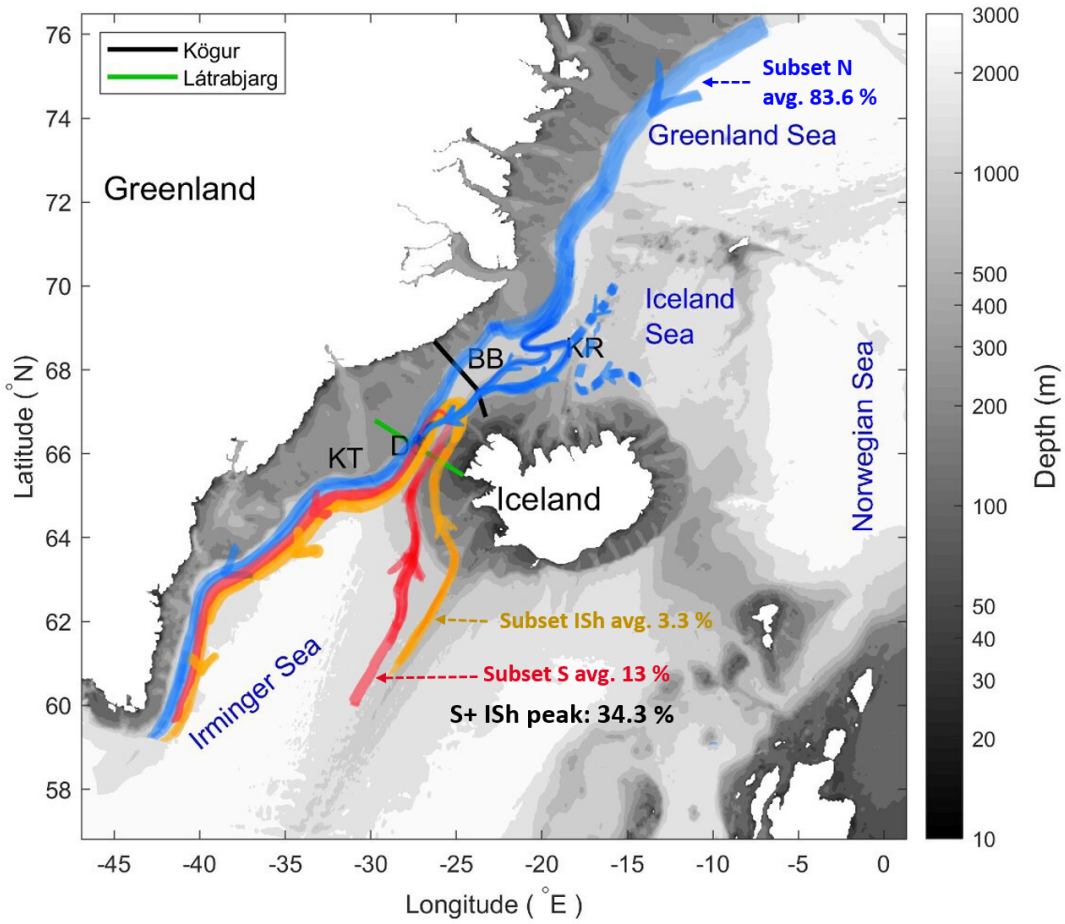

Figure 2.15: The upstream and downstream schematic pathways of the DSO in the model. The annual average contribution (avg. %) from each subset and maximum contribution from the south (S+ ISh) to the DSO origin are annotated.

The southern pathways (revealed by the S and ISh subset particles) are the main addition to the previous schematics by Våge et al., 2013, Harden et al., 2016, and Jong et al., 2018 although this contribution is likely to vary inter-annually depending on the local surface forcing. These newly identified pathways (S+ ISh) are shown to supply up to 34.3 % of the DSO water, and is

an important contribution to understanding the overflow water sources and composition. The highest contribution from the south is seen when there is more dense water on the Iceland shelf. The sparse in-situ observational evidence suggests that there is a correlation between the existence of dense water ($\sigma_\theta \geq 27.8$ kg m^{-3}) on the shelf and a high winter NAO index, consistent with strong atmospheric cooling. However, the dynamical relationship between the atmospheric state and variability of dense water on the shelf needs more investigation and is left for future work. These dense water observations are mostly from 1980s and 1990s when a warming trend of 0.2-0.4 °C/decade close to the bottom in the depth range of 100-250 m on the Iceland shelf is observed (Jochumsen, Schnurr, and Quadfasel, 2016). The warming can be another explanation for the missing dense profiles in recent years, in addition to the phase of the NAO. Determining the formation mechanism of the southern DSO sources is beyond the scope of this study, and could be a fruitful topic of future research.

Chapter 3

Using hydraulic theory to monitor dense overflows in a parabolic channel

> This broken bowl that is thrown away on the road, was once beautifully fashioned
> Be aware you tread not on it wantonly, for this bowl has been made from the bowl of human's mind.
>
> Omar Khayyam, Rubaiyat.

3.1 Introduction

The deep oceans are partitioned by submarine ridges into basins that are often connected by deep passages. The watermass exchange between these basins is an important process in the global overturning ocean circulation. For example, overflows of dense water across the Greenland-Scotland Ridge feed the lower limb of the Atlantic meridional overturning circulation (AMOC). The overflow

transport is controlled by the topography and by the width of the passages. It has been shown that the flow is hydraulically controlled at the topographic sills that lie within the passages, meaning that the sills exercise some degree of influence over the volume flux and upstream stratification (Pratt and Whitehead, 2008). These choke points are strategic places to monitor the volume flow rates and ultimately estimate the state and variability of the thermohaline circulation (Helfrich and Pratt, 2003).

The pathway and the volume flux of the water approaching a sill are affected strongly by the geometry of the sill and the Earth's rotation. Rotating hydraulic theory provides insight into the pathway of the flow as it approaches the sill as well as establishing formulae for calculation of volume flux. Stern, 1972 pioneered the use of rotating hydraulics in oceanography. Whitehead, Leetmaa, and Knox, 1974 developed the first analytical model of hydraulic behavior in a steady rotating channel flow with rectangular cross-section and performed a set of laboratory experiments to test the transport relations. The assumption in their work was that the flow is fed from a deep quiescent reservoir (with infinite layer thickness) and therefore, zero potential vorticity (pv). Gill, 1977 introduced a unifying framework for rotating hydraulics for a finite basin with constant (nonzero) pv. The Gill model provided insight about how the water approaches the sill from the upstream basin. For a sufficiently wide reservoir (relative to the Rossby deformation radius), the upstream flow is divided into two independent boundary layers. For a given sill geometry and rate of supply of fluid to the reservoir, the Gill model provides ranges of steady controlled solutions (Gill, 1977; Pratt and Whitehead, 2008). Whitehead,

1989; Whitehead, 1998; Borenäs and Nikolopoulos, 2000 modified hydraulic models in order to make the transport relation easier to apply. Killworth and McDonald, 1993 developed bounds on transport in terms of upstream flow measurements. None of these studies considered various types of inflow and their effect on the controlled flow in the channel, however, nor did they consider effects of dissipation or friction. Helfrich and Pratt, 2003 developed an idealized model of a basin-strait system with three different inflows introduced into a bowl-shaped basin in order to investigate how the pathways of overflow is affected by the basin circulation. They considered boundary inflows as well as localized, and uniform downwelling. Their simulations also accounted for bottom friction. The different inflows resulted in different circulation patterns and interface heights within the basin, but their study revealed that the flow in the channel is remarkably independent of the type of inflow in the basin and thus the potential vorticity in the channel (a key quantity in rotating hydraulics) is also independent of the location of the upstream mass source. This simplification allowed them to relate the transport to an upstream measurement of interface height. As opposed to the Gill model, the upstream measurement is made at the entrance of the channel rather than in the basin interior which is advantegous considering the dependence of interface height to the type of the circulation within the basin. Their study was restricted to a channel with rectangular channel cross section, bounded by vertical walls, as in most of the previous studies. Despite mathematical convenience in considering a rectangular cross-section, it becomes difficult to apply the results in real oceanic channels, where the topography varies smoothly and where the layer thickness vanishes at the edges. Moreover,

the physics of the hydraulic processes potentially changes when the layer depth goes to zero at the edges: for one thing, the character of the edge waves that transmit hydraulic control to the upstream basin changes from that of a Kelvin-wave to that of a slower frontal-wave (Pratt and Whitehead, 2008). The parabolic channel cross-section greatly increases the chance of flow instability (Pratt, Helfrich, and Leen, 2008) and flow reversal which is more realistic in nature (Borenäs and Lundberg, 1986).

In this study, we follow-up on Helfrich and Pratt, 2003 by using a more realistic strait geometry and considering comparisons with non-zero uniform pv theory. We address the following questions: What are the transport pathways from the mass source through the basin, into the narrow strait and over the shallow sill? How do these pathways change as the location of the mass source changes? Does it remain true that the flow in the strait depends primarily on the volume flow rate, and is independent of the circulation in the upstream basin as in the case of rectangular channel geometry? How far into the strait does the fingerprint of the upstream circulation penetrate? What features characterize velocity distribution and interface shape in the region where the flow encounters the obstacle, spills over the crest of the obstacle, and descends downstream? What are some possible monitoring strategies that take advantage of the fact that hydraulic control and hydraulic criticality exist at or near the sill? What is the best location to conduct monitoring with fixed instruments? Are there any trade-offs in terms of convenience and accuracy between possible strategies? We start by expanding on the theory formulated

by Borenäs and Lundberg, 1986 for the parabolic channel with uniform pv and then compare the theory with our numerical simulations.

3.2 Theory

The hydraulics theory for steady flow of a 1.5 layer (reduced-gravity) model with uniform non-zero pv in a rotating channel with rectangular cross section was described by Gill, 1977. In the Gill model, the flow was assumed to come from a wide upstream basin and funnel through a narrow channel into a downstream basin. Borenäs and Lundberg, 1986 extended the Gill theory into a more geophysically realistic case by considering a parabolic cross-section resembling the rounded nature of real-world sea-straits. In this case, there is no distinction between the sidewalls and the bottom boundary of the channel. In the following subsection, we expand on the theory by solving the critical condition and providing graphical tools to interpret the solution. Then we compare the predictions from the theory with the results from numerical simulations for a range of parameter values.

3.2.1 parabolic channel cross-section

The basin-channel geometry considered in this study is sketched in Figure 3.1.

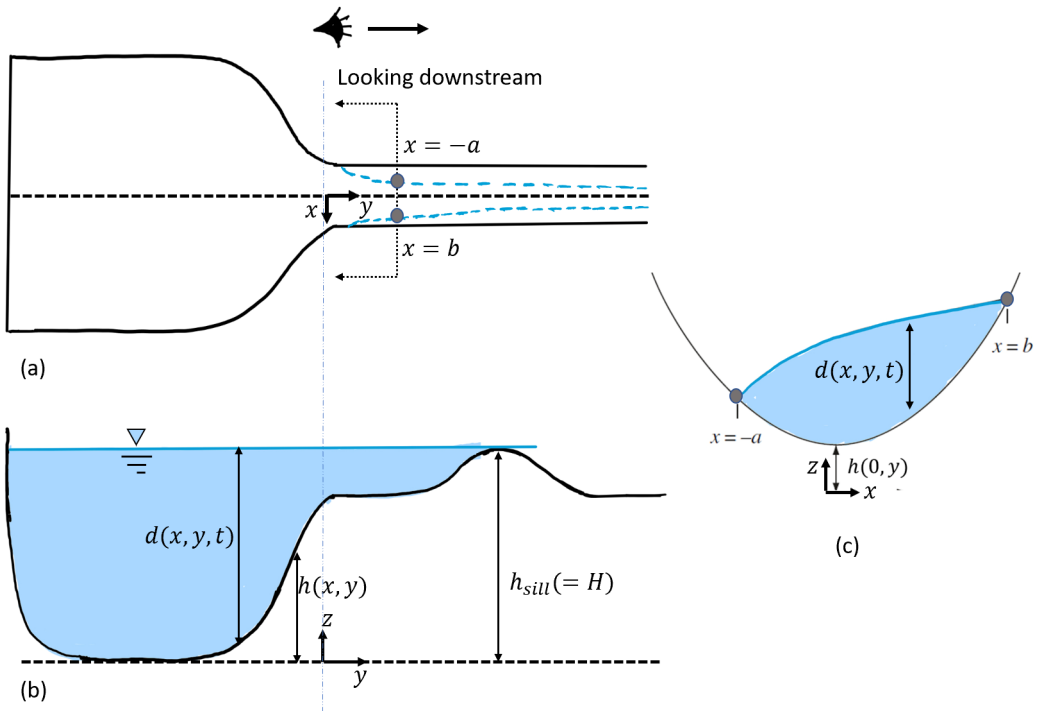

Figure 3.1: Sketch of the domain geometry (a) plane and (b) side view of basin-channel geometry considered for the numerical model. In (a), the schematic wetted edges of the flow are marked as blue dotted dashed lines along the channel (c) channel cross section upstream of the sill looking downstream. The water interface intersects the bottom at $x = b$ and $x = -a$ marking the wetted edges of the flow. Note that the origin of the Cartesian coordinate is located at the entrance of the channel. The $h(0, y)$ function is the bottom elevation at the center of the channel.

The channel bottom elevation in dimensional form is:

$$h^*(x, y) = h^*(0, y) + \alpha(y){x^*}^2, \tag{3.1}$$

where $h^*(0, y) = h_0^*(y)$ is the bottom elevation at the center of the channel and $\alpha(y)$ is the dimensional parabolic curvature, a parameter that can vary along the channel. If we scale the h^* with layer depth scale H (this can be considered to be the sill depth), and x^* with the Rossby radius of deformation

($L_d = \sqrt{g'H/f}$), then the nondimensional equation for the bottom elevation becomes:

$$h(x,y) = h(0,y) + x^2/r(y), \tag{3.2}$$

where $r(y) = f^2/g'\alpha(y)$ is the non-dimensional radius of curvature. Pratt and Whitehead, 2008 interpret $r(y)$ in the following way: suppose that the fluid is at rest, so that the interface is horizontal, and that the channel is filled to a depth D, measured at the center $x = 0$. Then the half width of the interface is $(\frac{D}{\alpha(y)})^{1/2}$ and the ratio of the square of this length to L_d is then r which is small for narrow channels and large for wide channels.

For the rest of the paper, all equations are non-dimensional (unless stated otherwise). Considering geostrophic balance in the cross channel direction, the non-dimensional shallow water equations in the x-direction reduce to the velocity in the y direction

$$v(x,y) = \partial d/\partial x + \partial h/\partial x, \tag{3.3}$$

and the potential vorticity becomes,

$$q(x,y) = \frac{1 + \partial v/\partial x}{d}. \tag{3.4}$$

If we combine equations 3.3 and 3.4, an equation for variation of depth in the x-direction can be derived:

$$\frac{\partial^2 d}{\partial x^2} - qd = -1 - \frac{\partial^2 h}{\partial x^2} \tag{3.5}$$

Substituting equation 3.2 for the parabolic bottom profile into equation 3.5 results in a second order ordinary differential equation:

$$\frac{\partial^2 d}{\partial x^2} - qd = -1 - 2/r(y) \tag{3.6}$$

Assuming q is constant (uniform pv with no forcing or dissipation), the solution has the form:

$$d(x,y) = C_1 e^{\sqrt{q}x} + C_2 e^{-\sqrt{q}x} + \frac{1+2r^{-1}}{q} \tag{3.7}$$

The y-dependent coefficients C_1 and C_2 can be determined by the boundary conditions at $x = -a, b$ where the interface intersects the bottom of the parabola (see Figure 3.1 (c)). Therefore, $d(-a) = d(b) = 0$, leading to:

$$d(x,y) = \frac{1+2r^{-1}}{q}\left(\frac{\sinh\sqrt{q}(x-b) - \sinh\sqrt{q}(x+a) + \sinh\sqrt{q}(a+b)}{\sinh\sqrt{q}(a+b)}\right). \tag{3.8}$$

Substituting $d(x,y)$ in equation 3.3, leads to the corresponding geostrophic velocity:

$$v(x,y) = \frac{1+2r^{-1}}{\sqrt{q}}\left(\frac{\cosh\sqrt{q}(x-b) - \cosh\sqrt{q}(x+a)}{\sinh\sqrt{q}(a+b)} + 2r^{-1}x\right). \tag{3.9}$$

The volume transport is:

$$\begin{aligned} Q &= \int_{-a}^{b} d(x,y)v(x,y)dx \\ &= \frac{(r+2)(a-b)}{qr^2}\left(\frac{2(\cosh\sqrt{q}(a+b)-1)}{\sqrt{q}\sinh\sqrt{q}(a+b)} - (b+a)\right) \\ &= \frac{(r+2)(a-b)(2\cosh\sqrt{q}(a+b)-2-(b+a)\sqrt{q}\sinh\sqrt{q}(a+b))}{q^{3/2}r^2\sinh\sqrt{q}(a+b)}. \end{aligned} \tag{3.10}$$

The Bernoulli function is:

$$B = v(x,y)^2/2 + d(x,y) + x^2/r + h_0(y), \tag{3.11}$$

where $h_0(y) = h(0,y)$ is the topographic height at the center of channel and only depends on y. The Bernoulli function is conserved along streamlines, including the streamlines corresponding to the edges of the flow. Evaluating the Bernoulli function at the intersections of interface height with the parabolic bottom leads to

$$\begin{aligned} B(-a) &= v(x,y)^2/2 + d(x,y) + a^2/r + h_0(y) \\ &= \frac{1}{2}\left(\sigma - 2r^{-1}a\right)^2 + 0 + a^2/r + h_0(y) \end{aligned} \tag{3.12}$$

and

$$\begin{aligned} B(b) &= v^2/2 + d + b^2/r + h_0(y) \\ &= \frac{1}{2}\left(\sigma - 2r^{-1}b\right)^2 + 0 + b^2/r + h_0(y), \end{aligned} \tag{3.13}$$

where:

$$\sigma = (1 + 2/r)\frac{\cosh\left(\sqrt{q}(a+b) - 1\right)}{\sqrt{q}\sinh\left(\sqrt{q}(a+b)\right)}. \tag{3.14}$$

Notice that $d(-a, y) = d(b, y) = 0$. Then the average of the Bernoulli function on the two edges becomes:

$$\begin{aligned} \bar{B} &= \frac{B(-a) + B(b)}{2} \\ &= \frac{2}{r^2}(a^2 + b^2) + \sigma^2 - \frac{2(a+b)\sigma}{r} + \frac{a^2 + b^2}{2r} + h_0(y) \end{aligned} \tag{3.15}$$

A complete description of the flow at any section (y-value) of the channel is provided by the variables $a(y)$ and $b(y)$, along with the potential vorticity and the local geometric parameters $h_0(y)$ and $r(y)$. The evolution of the flow in the y-direction is governed by the statements of conservation of the volume flux Q and the Bernoulli function B-bar. The condition for hydraulic criticality of the flow can be obtained from these conservation statements using the multivariate approach described in Pratt and Whitehead, 2008. We consider the two Gill functions G_1 and G_2 to be the volume transport relation, and the average Bernoulli function. The two dependent variables describing the state of flow are considered to be $\gamma_w = a + b$ which is the wetted width and $\gamma_c = a - b$ which is twice the centerline position of the flow at any cross-section. Therefore, the transport, G_1, and the Bernoulli function, G_2, can be

rewritten in terms of variables γ_w and γ_c, and parameters, q and r as:

$$Q = G_1(\gamma_w, \gamma_c; q, r) = \frac{(r+2)\gamma_c}{qr^2}\left(\frac{2(\cosh\sqrt{q}\gamma_w - 1)}{\sqrt{q}\sinh\sqrt{q}\gamma_w} - \gamma_w\right), \tag{3.16}$$

from equation 3.10 and

$$\bar{B} = G_2(\gamma_w, \gamma_c; q, r) = \sigma^2 + \frac{\gamma_w^2 + \gamma_c^2}{r^2} - \frac{2\sigma\gamma_w}{r} + \frac{\gamma_w^2 + \gamma_c^2}{4r} + h_0(y), \tag{3.17}$$

from equation 3.15, where $\sigma = (1 + 2/r)\frac{\cosh\sqrt{q}\gamma_w - 1}{\sqrt{q}\sinh\sqrt{q}\gamma_w}$.

The critical condition corresponds to the requirement that the flow supports a stationary wave and occurs when:

$$J_{\gamma_w,\gamma_c}(G_1, G_2) = \frac{\partial G_1}{\partial\gamma_w}\frac{\partial G_2}{\partial\gamma_c} - \frac{\partial G_1}{\partial\gamma_c}\frac{\partial G_2}{\partial\gamma_w} = 0. \tag{3.18}$$

Taking derivatives of G_1 and G_2 with respect to γ_w and γ_c, and substituting them in equation 3.18 results in:

$$\frac{\left(\gamma_w\sqrt{q}\,\mu_1 - 2\,\mu_2 + 2\right)\left(2\,r - 2\,\mu_2 + \gamma_w\sqrt{q}\,\mu_1 + 2\right)}{q\mu_1\left(2\,\mu_1 + \sinh\left(2\,\gamma_w\sqrt{q}\right)\right)} - \frac{{\gamma_c}^2}{2(\mu_2 + 1)} = 0, \tag{3.19}$$

where, $\mu_1 = \sinh\left(\gamma_w\sqrt{q}\right)$ and $\mu_2 = \cosh\left(\gamma_w\sqrt{q}\right)$. Borenäs and Lundberg, 1986 arrived at the same condition using perturbation analysis. Equation 3.19

implies a relationship between γ_w and γ_c at the critical section for given values of q and r. Therefore, a reduction in the number of independent measurements is established. From the multi-variable approach, the critical section is shown to be located at the sill section (Pratt and Whitehead, 2008). In the next section, we solve for the critical solution for any given sets of q and r matching our theoretical simulations.

3.3 Numerical Solver

The model solves the non-dimensional 1.5 layer shallow-water momentum and continuity equations on the f-plane just as in Helfrich and Pratt, 2003 but the coordinate system is rotated (270° counterclockwise) to be consistent with the theory. The momentum and continuity equations are:

$$\frac{\partial \mathbf{u}}{\partial t} + \mathbf{u}.\nabla_h \mathbf{u} + \hat{\mathbf{k}} \times \mathbf{u} = -\nabla_h (d+h) + \mathbf{D} + \mathbf{M}, \tag{3.20}$$

and

$$\frac{\partial d}{\partial t} + \nabla_h.(\mathbf{u}d) = -w, \tag{3.21}$$

where ∇_h is the horizontal gradient operator, $\hat{\mathbf{k}}$ is the unit vector in the vertical direction, the symbols for variables such as the bottom topography $h(x,y)$ and interface height $d(x,y)$ are consistent with Figure 3.1. The horizontal velocity vector $\mathbf{u}(x,y)$ is scaled with $\sqrt{g'H}$, the vertical downwelling velocity $w(x,y) < 0$ is scaled by Hf, the lengths in the horizontal x-y plane

and in z direction are scaled with deformation radius ($\sqrt{g'H}/f$), and H, respectively. The time t is scaled with f^{-1}. D is the friction operator which is a linear bottom drag $D = -\epsilon\mathbf{u}$ with constant coefficient ϵ (scaled with f). $\mathbf{M}$ is momentum flux due to downwelling in the basin with $\mathbf{M} = w\mathbf{u}\Theta(-w)/d$. The $\Theta(w)$ is a step function which is equal to 1 for $w < 0$ and 0 for $w > 0$. The scaling is consistent with the theory, however the numerical model includes extra terms such as friction. The dissipation is necessary to reach a steady state solution and make comparisons with the theoretical derivations discussed earlier.

The basin is bowl-shaped with topographic height $h(x, y)$ as in Figure 3.1. It has a flat bottom and is smoothly connected to the channel through a Gaussian slope region between $-5 < y < 0$. The basin's back wall is located at $y = -15$. The basin width is 8 along the x direction and it narrows with a Gaussian shape centered at $y = 0$ to a channel with parabolic cross section. The sill is located at $y = 6$. The numerical domain is necessarily finite. The parabolic cross section is tall enough that the active layer never reaches the edges of the domain, however, vertical walls are placed as numerical boundary conditions. Thus the parabolic channel is contained by vertical walls that are spaced sufficiently widely that contact is never made with the active layer. The vertical walls of the numerical grid are symmetric about $y = 0$ marked by black boundaries along the channel in Figure 3.1 (a)). As the layer thickness changes along and across the channel, the dynamic width of the flow changes as well. The edges of the dynamic width along the channel are shown as blue

dotted dashed lines in Figure 3.1 (a). The interface height at an arbitrary upstream section is shown in Figure 3.1 (c). To avoid abrupt geometric changes at the channel entrance, the parabolic channel has a slowly varying radius of curvature $r(y)$ ramping up from zero to a constant value $r(y) = r_0$ with an inverse Gaussian function at the mouth of the channel entrance ($0 < y < 1$) and then the curvature remains constant throughout the channel afterwards ($r(y \geq 1) = r_0$).

The flow can enter the basin in three different ways similar to Helfrich and Pratt, 2003 to mimic conditions in nature: uniform downwelling or localized downwelling to represent convection, or inflow through a segment of the basin boundary, representing drainage from another basin. The uniform downwelling $w < 0$ is imposed throughout the basin ($y < 0$), the localized downwelling is placed at the upstream wall of the basin with uniform w in the x direction and a Gaussian function of width $\sqrt{(2)}/2$ centered at $y = -15$. The boundary inflow enters through the upstream wall between $-0.5 < x < 0.5$ with uniform volume flux in x.

The numerical model solves equation 3.20 in flux form and equation 3.21 using a second-order finite volume method that handles complexities such as grounding (fluid depth going to zero), shocks and hydraulic jumps. The details about the numerical algorithm and its implementation are explained in Helfrich and Pratt, 2003 and Helfrich, Kuo, and Pratt, 1999. The model solves for the velocities on an orthogonal generalized quadrilateral grid. The

solution is mapped back to a Cartesian grid using conformal mapping.

The transformation is described by Knupp and Steinberg, 1993 and the details of its algorithmic implementation which solves the velocity field in the mapped domain is explained by Bell, Solomon, and Szymczak, 1989. The numerical width of the channel varies in different simulations depending on r, but because the variations are small, the number of grid cells does not need to be changed to sustain the numerical stability and the Courant-Friedrichs-Lewy (CFL) condition. The number of the grid cells for all simulations is the same with 220 cells in the y direction and 80 cells in the x direction. The average grid cell sizes are $\Delta y \approx 0.11$ and $\Delta x \approx 0.1$. The flow exits the domain at $y = 9$ through an open boundary set by the Orlanski radiation condition (Helfrich, Kuo, and Pratt, 1999). All other boundaries are set to no-flux condition.

The numerical solutions are initialized with the basin filled with motionless fluid up to the sill crest as shown in Figure 3.1 (b). The specified imposed volume flux enters the basin at $t = 0$ and the model is integrated until a steady solution is obtained. For certain parabolic curvatures, Q, and ϵ, a steady state may not be achieved.

3.4 Results

3.4.1 Simulations

We ran several experiments with ranges of parameter values. The range of imposed non-dimensional mass flux is $0.01 \leq Q \leq 0.1$. The range of drag coefficient is $0.001 \leq \epsilon \leq 0.05$, but most cases shown here are run with

$\epsilon = 0.01$. All experiments have the same basin geometry and sill height but different parabolic channel curvatures. For a parabolic channel the width of the flow is not specified by the width of the channel (as opposed to rectangular channel) and it is a dynamically determined variable depending on the value of the imposed Q and the curvature of the parabola. However, one must choose an appropriate width for the numerical grid in the first place to make sure the water does not reach the vertical walls that bound the parabola. This is one of the complexities of introducing a realistic bottom channel topography.

We discuss two specific geometries: a relatively wide and a relatively narrow channel which represent the parameter space we explored. The first (relatively wide) case study has $r_0 = 2/3$ which resembles the bottom topography at Faroe Bank Channel (Borenäs and Lundberg, 1988).

The relatively narrow case has $r_0 = 1/6$ resembling bottom topography of narrow gaps such as fracture zone canyons along mid-Atlantic ridges (Clement, Thurnherr, and Laurent, 2017), and the western pathway of the Samoan passage (Alford et al., 2013).

Figure 3.2 shows the numerical solutions of interface height, and transport (depth-integrated) velocity (or equivalently gradient of streamfunction) for $r_0 = 2/3$ with $Q = 0.05$ introduced in the form of boundary inflow, uniform and localized downwelling at the steady state ($t = 6000$).

The Gill theory predicts that the inflow splits into two boundary currents that flow around the basin boundary to rejoin at the strait. Unlike the Gill

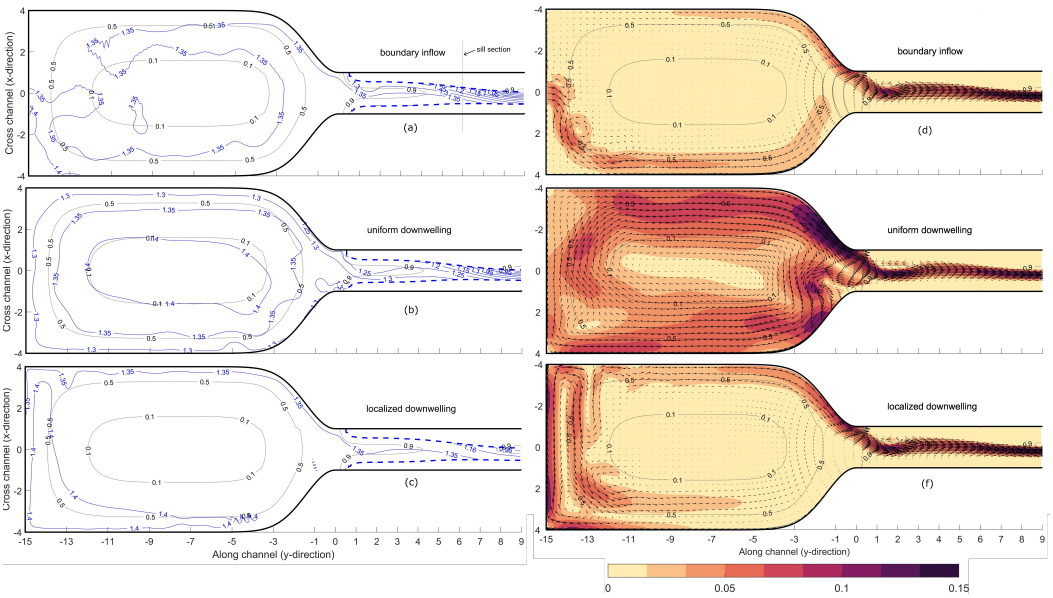

Figure 3.2: (a), (b), and (c) show the contours of interface height $h + d$ for the basin and channel with $r = 2/3$, $Q = 0.05$, $\epsilon = 0.01$ at the steady state $t = 6000$ for the three types of inflows: boundary inflow, uniform downwelling, and localized downwelling. (d), (e), and (f) show the transport velocity, $\mathbf{u}d$. The dotted lines are contours of topography. The dashed line in panel (a) marks the sill section at $y = 6$, which is the same for all panels. The colorbar shows the transport velocity magnitude and the vectors have non-dimensional scale of 1.

model, the potential vorticity in the numerical simulations is non-uniform, in part due to the bowl shaped topography of the basin. Although, boundary currents are present in the basin we see additional features. For the case of boundary inflow shown in Figure 3.2 (a) and (e), the flow in the basin approaches the strait as boundary currents, but additionally we see that the flow recirculates around the closed contours of interface height. The branch approaching the strait along the right wall ($x > 0$), crosses to the left wall as it approaches the channel entrance. The reason for this diversion is that the flow acquires cyclonic circulation due to the decrease in layer thickness as the flow gets closer to the mouth of the channel. Although the planetary vorticity is constant, the vortex squashing set by the decrease in layer thickness causes an increase in the relative vorticity of the flow close to the left wall. This veering to the opposite wall is also observed in laboratory experiments and is believed to account for the observation that the overflow carried by the North Icelandic Jet (NIJ) upstream of the Denmark Strait sill hugs the Iceland coastline, its dynamical western boundary (Pratt and Whitehead, 2008). The separated East Greenland Current steering toward the Iceland coastline can potentially be explained by this veering as well.

For the case of uniform downwelling (Figure 3.2 (b) and (e)), the flow in the basin is mostly anticyclonic. The flow approaches the channel mostly from the left wall. At the channel entrance, some of the flow returns back to the basin forming an asymmetric anticyclonic circulation. When the downwelling is localized at the back wall (Figure 3.2 (c) and (f)), the flow is again fed to the channel from the left wall with very little reverse flow into the basin. The

basin circulation is still predominantly anticyclonic, but is localized near the back wall. In general, the basin circulation has some qualitative similarities to what Helfrich and Pratt, 2003 showed in their simulations for the rectangular channels, however, the flow in the channel especially at the entrance is different.

In all three cases, the flow enters the parabolic channel from the left wall, but is diverted toward the channel center forming a recirculation upstream of the sill and localized near the entrance ($1 < y < 2.5$) as is evident from Figure 3.2 (d), (e), and (f). This feature is persistent regardless of the inflow type in the basin. The case of uniform downwelling (Figure 3.2(b) and (d)) creates a larger flow reversal resulting in a strong jet flow toward the middle of the channel and a large reverse flow toward the right wall at the entrance. Eventually, the transport velocity profile in the channel becomes nearly the same for all three cases downstream of the localized recirculation ($y > 2.5$). Several experiments with wider channels showed similar behavior but with a stronger recirculation and flow reversal near the entrance. Previous theoretical studies showed that the flow reversal happens for channels with $r_0 \geq 2/3$ (Borenäs and Lundberg, 1986; Pratt and Whitehead, 2008) consistent with our simulations, though the location of the reversal is not always specified.

The interface height profile along the centerline of the channel and at two upstream cross-sections are shown in Figure 3.3. The depression in the interface height due to recirculation at $0.8 < y < 3.6$ is visible for all three inflow types, but it is larger for uniform downwelling. The height profiles for all

three cases coincide with each other after about $y > 3.6$. Notice that at the $y = 2$ cross-section (Figure 3.3 (b)), although the height profiles differ in the middle of the channel, the heights are nearly identical at the right and left edges for all three types of inflow. This is also true all along the channel after $y > 3.6$. Although the basin circulation intrudes into the entrance, it does not affect the channel flow down the channel.

Plots of potential vorticity (pv) for these cases (Figure 3.4) show that at the flow edges, where the layer depth approaches zero (e.g., $d < 0.08$), the pv becomes unrealistically large, therefore we removed the contours near the boundary from the plot (in this paper, the pv values where the layer thickness is $d < 0.08$ are omitted). As expected, the pv distribution is nonuniform along and across the channel. The pv contours get closer together as the edges of the flow narrows along the channel. The influence of mass source type can be seen again near the channel entrance. For the case of boundary inflow and localized downwelling (Figure 3.4 (a) and (c)), the pv contours near the left wall are continuous along the channel. But for the case of uniform downwelling, (Figure 3.4 (b)) because of the return flow discussed earlier (Figure 3.2 (e)), some of the contours are diverted from the left wall back into the basin. Note that the pv contours down the channel (e.g. at $y > 3.6$) are nearly identical for all three mass source types.

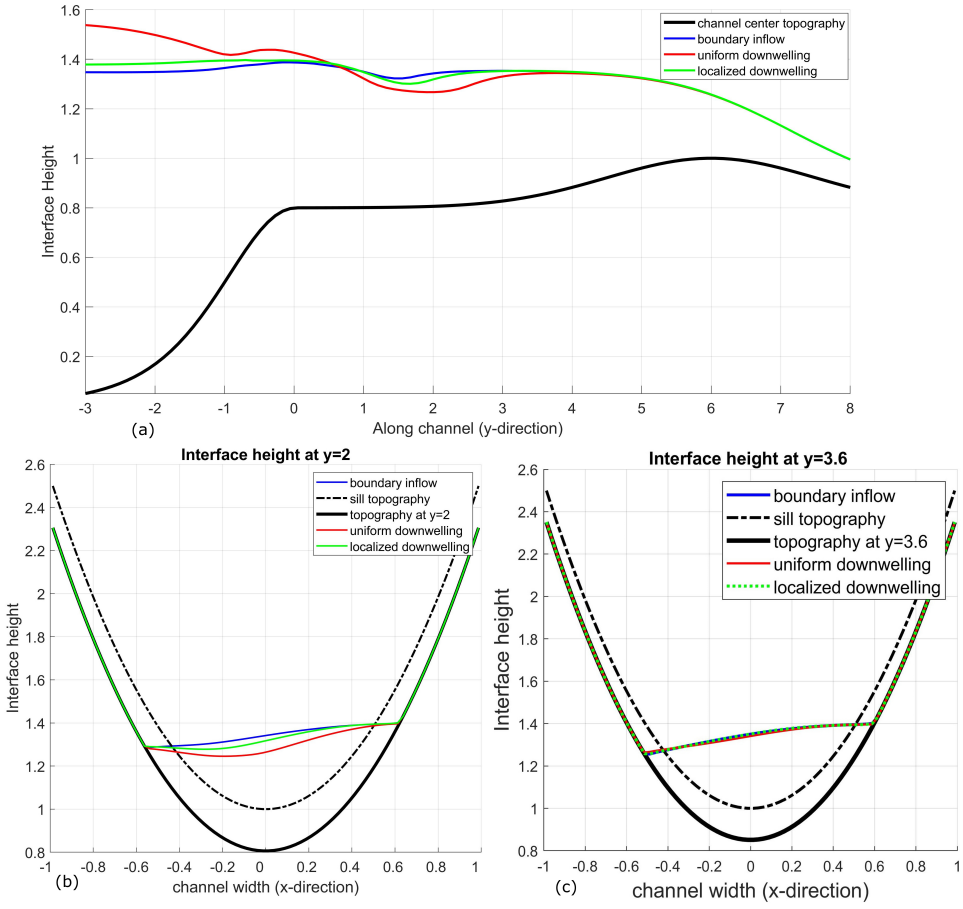

Figure 3.3: The interface height (a) along the channel centerline (b) at channel cross section at $y = 2$, (c) at $y = 3.6$ for the three types of inflow at the steady state ($r_0 = 2/3$, $Q = 0.05$, $\epsilon = 0.01$).

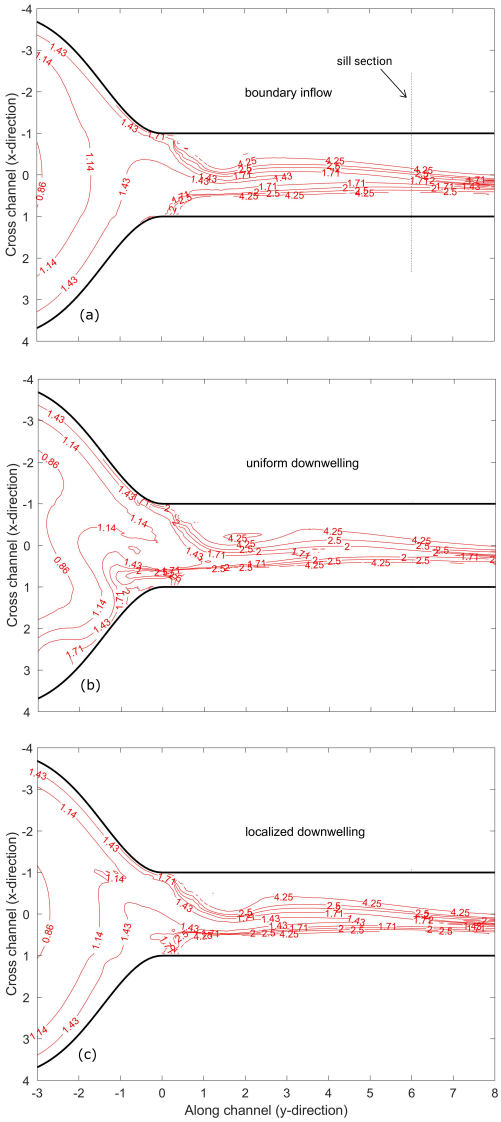

Figure 3.4: The pv contours near the entrance and in the parabolic channel with $r_0 = 2/3, Q = 0.05,\ \epsilon = 0.01$ at the steady state with different types of inflow.

Parabolic cross-sections with higher curvatures (narrower channels) show a different regime of behaviors. We ran several experiments with radius of curvatures such as $r_0 = 1/3, 1/6$, and $1/15$. But we only show figures from

our second case study with $r_0 = 1/6$ as it is representative of all narrow channels. Figure 3.5 (a) shows the interface height for the case of boundary inflow. We omit showing the plan view of the height contours for the case of uniform downwelling and localized downwelling as they are similar to that of boundary inflow with the difference that the flow approaches the channel mainly from the left boundaries. Figure 3.5 (b) shows the interface height profile at $y = 2$ for three mass source types. The three interfaces are indistinguishable and independent of mass source type. They also have a higher cross-channel slope in comparison to the first case study ($r_0 = 2/3$, Figure 3.3 (b)) which has the same Q but a wider stream. Also the interface height slopes more linearly than the first case study which had a depression in the middle of the cross-section.

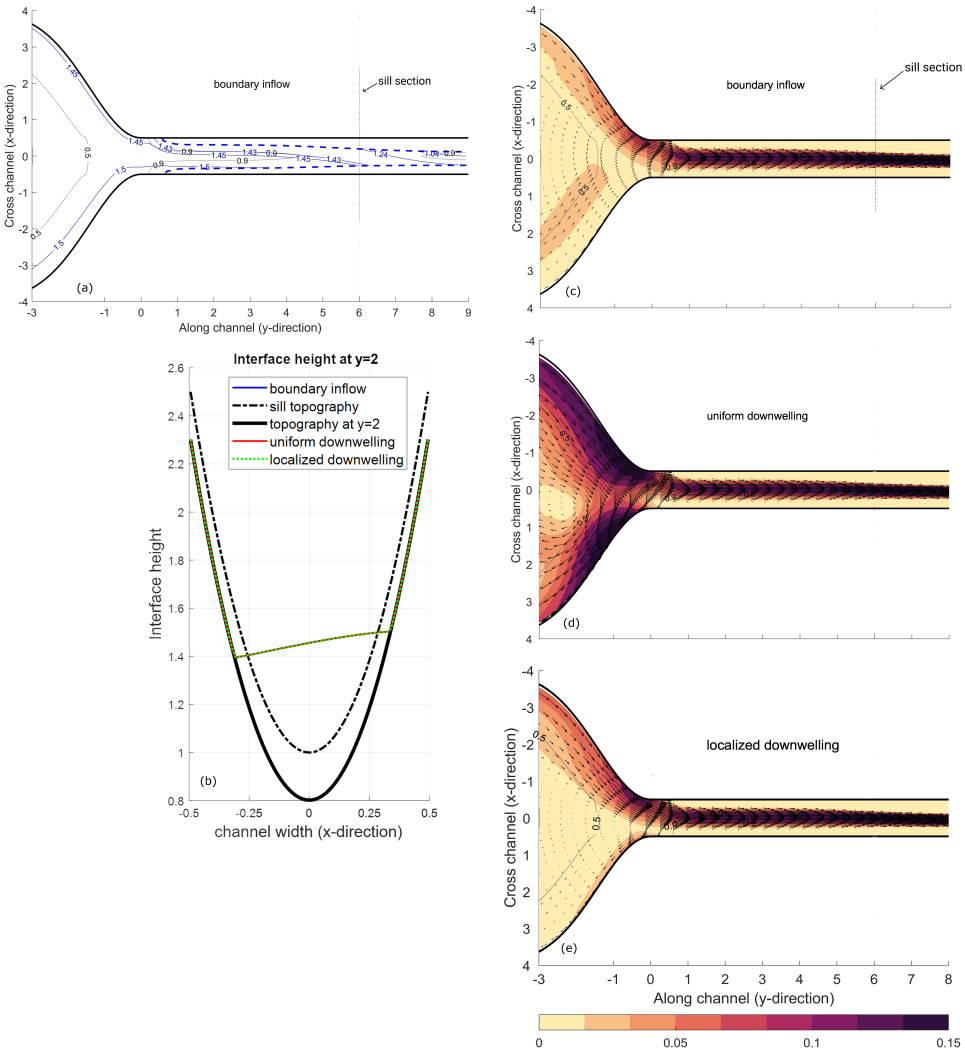

Figure 3.5: (a) Contours of interface height for boundary inflow (b) interface height profile in the channel cross section at $y = 2$ for the three types of inflow. The bottom topography at the sill and at the entrance are also shown by the black dashed and solid lines. (c), (d), and (e) transport velocity for the case of boundary inflow, uniform downwelling, and localized downwelling, respectively. All panels are for $r_0 = 1/6$, $Q = 0.05$, $\epsilon = 0.01$ at the steady state.

Comparing the transport velocities in Figure 3.5 (c), (d), and (e) for three mass source types with those of Figure 3.3 (d), (e), and (f), we see that the flow in the narrow channel is diverted toward the middle of the channel soon after

it passes the entrance. Therefore, the basin circulation does not intrude into the channel further than $y = 0.5$, and the mass source type does not affect the flow further in the channel. Besides, the flow reversals in the mouth of the channel on the right wall ($-1 \leq y \leq 0.5$) are localized and quite smaller in comparison to the first case study. For the experiments we ran with even narrower parabolas (e.g. $r = 1/15$), the channel flow is independent of basin circulation even at the entrance (e.g. $y \leq 0.5$).

The friction coefficient ϵ in the cases discussed above was 0.01. We performed a sensitivity study to the friction coefficient by running experiments with $0.0001 \leq \epsilon \leq 0.05$. The flow becomes unsteady for small values of friction coefficient. The critical ϵ which makes the flow to transition to an unsteady state depends on mass source type similar to what Helfrich and Pratt, 2003 found. For example, for the case of $r_0 = 2/3$, $Q = 0.05$, and (uniform or localized) downwelling mass source with $\epsilon < 0.005$, the flow does not reach steady state, whereas for boundary inflow the cutoff for transition to unsteady regime is $\epsilon < 0.0025$. The steady state flow at the entrance has some sensitivity to the friction coefficient. As we saw earlier in Figure 3.3, the steady state flow at the entrance is sensitive to the mass source type. As ϵ increases (e.g. from 0.01 to 0.04), the sensitivity to the inflow at the channel entrance decreases, and the interface height slopes more linearly. Similar to the interface height, the pv contours become more uniform along the channel for larger ϵ. Also, sensitivity to ϵ is less in narrow parabolas. Further study of the properties of the unsteady flow is beyond the scope of this thesis.

3.4.2 Comparison of Simulations with Theory

Although the theory for constant pv flow in a parabolic channel is known, graphical tools that help with interpreting the solutions have been lacking. In order to better understand hydraulic behavior of the theoretical flow, we turn to a diagram that shares some features to the Froude number plane developed by Armi, 1986 for two-layer flows. Instead of the Froude number plane, we use the $\gamma_w - \gamma_c$ plane as in Figure 3.6 (a). Recall that γ_w can be interpreted as the width of the flow and γ_c as twice the centerline position of the flow, respectively, at any given cross-section. There are three sets of theoretical curves in Figure 3.6 (a). The thick black dashed-line is the solution of the critical condition (equation 3.19) for a specified parabolic geometry with radius of curvature, r, and a fixed pv value, q. The blue and red curves correspond to the contours of constant Q and $\bar{B} - h_0(y)$ for the same fixed r and q, as evaluated using equations 3.16 and 3.17. Note that the critical solution and the $\bar{B} - h_0(y)$ contours are symmetric with respect to the γ_w axis, and the Q contours are anti-symmetric (the mirror image for $\gamma_c < 0$ is not shown).

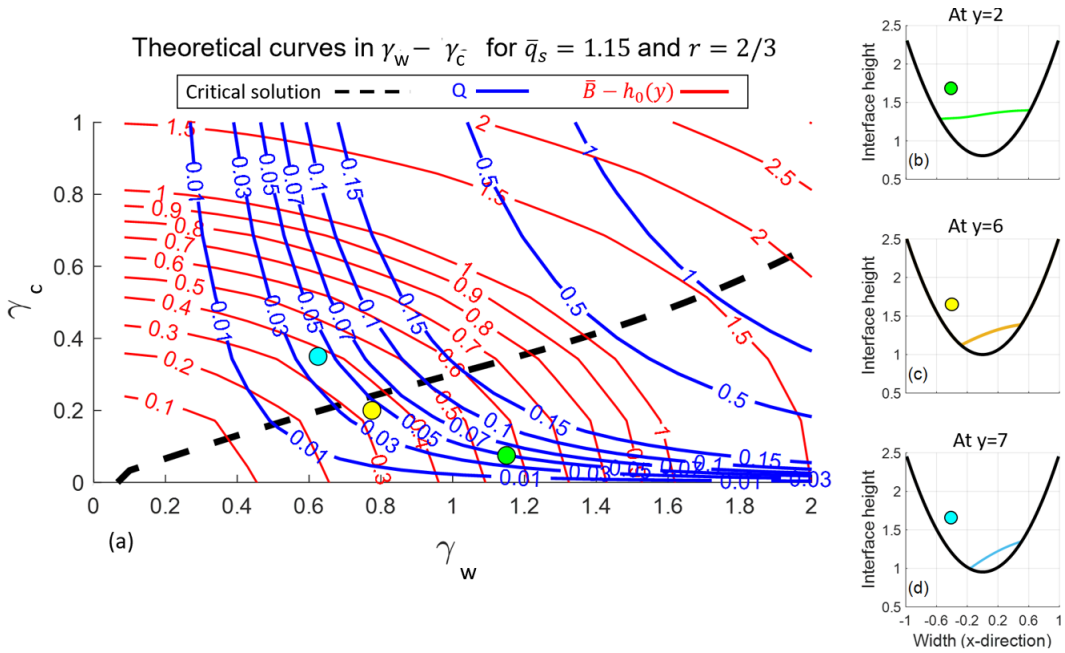

Figure 3.6: (a) Simulation- theory comparison in $\gamma_w - \gamma_c$ space. Theoretical curve of the critical solution is shown with the thick black dashed line. The contours of constant Q and $\bar{B} - h_0(y)$ are shown in blue and red, respectively. The numerical solutions upstream near the entrance ($y = 2$), at the sill section ($y = 6$), and downstream ($y = 7$) are shown with green, yellow, and cyan circles, respectively. The interface height profiles and bottom topography at the corresponding (b) upstream, (c) sill, and (d) downstream sections are shown. Note that the numerical solution corresponds to the imposed $Q = 0.05$.

The graph can be used to develop intuition about the behavior of the flow as the fluid passes through the channel and encounters a varying bottom elevation by tracing along the constant Q curves. The position on any constant Q curve is determined by the local topographic elevation at the channel center, as given by the $\bar{B} - h_0(y)$ curves. Since the flow is steady, $\bar{B}$ is constant everywhere. Therefore the contours of $\bar{B} - h_0(y)$ represent changes in topographic height $h_0(y)$ as γ_w and γ_c vary along the channel. Notice that the contours of constant Q and $\bar{B} - h_0(y)$ are tangent to each other along the critical solution (the black dashed-line) implying that the critical flow can only occur where

h_0 is not changing in y: i.e. at the sill. Additionally, the two sets of curves suggest that the critical flow occurs where $h_0(y)$ reaches a maximum (i.e. at the sill). Below the dashed-line the flow is subcritical and above it the flow is supercritical.

Tracing a constant Q curve, the dynamic width of the flow tends to be wide at the channel entrance (large γ_w), and it narrows as the flow moves along the channel, passes over the sill, and then becomes supercritical. Also, the centerline position of the flow ($\gamma_c/2$) tends to increase as the fluid moves downstream. Thus the flow veers to the right and rides higher up on the right-hand bank of the channel. Figure 3.6 also shows comparisons to the numerical simulations for the specific case study with $r = r_0 = 2/3$ and constant $q = 1.15$. As shown earlier (Figure 3.4), the pv varies within the basin and along the channel. We replace the constant q in the theory by a representative average value $\bar{q}$ from the simulation. The average pv near the entrance is different from the average pv near the sill section. We choose to use the average pv both near the channel entrance region $2.5 < y < 3.5$ away from the recirculation region, and around the sill section at $5.5 < y < 6.5$ to compare the differences. Since the flow width dynamically changes along the channel, the integration width in the cross-channel direction changes as well. As discussed before, the pv value becomes unrealistically large near the wetted edges. To avoid this, the integration is calculated only in the portion of the channel width where the layer thickness, d, is larger than 0.08:

$$\overline{q_E} = \frac{1}{(x_R - x_L) \times 1} \int_{y=2.5}^{y=3.5} \int_{x_L(d>0.08)}^{x_R(d>0.08)} q(x,y) dx dy \tag{3.22}$$

For the boundary inflow of $Q = 0.05$ the average values of pv become $\overline{q_E} = 2.08$ near the entrance and $\overline{q_S} = 1.15$ around the sill from the simulation. We use the average value of pv near the sill to construct Figure 3.6 (a). The simulation with imposed $Q = 0.05$ results in the interface height profiles shown in Figure 3.6 (b), (c), and (d) near the entrance at $y = 2$, the sill section at $y = 6$, and a downstream section at $y = 7$. Pairs of γ_w and γ_c are calculated by finding the intersection of the interface height with the bottom topography at these three sections and are mapped on to the theoretical graph as green, yellow and cyan circles in Figure 3.6 (a). Note that as the flow moves along the channel from the upstream section to the downstream section (from panel (b) to (d) in Figure 3.6), the flow regime changes from subcritical to supercritical. Also, the three circles in Figure 3.6 (a) show that the stream narrows (γ_w decreases) and the centerline of the flow shifts to the right (γ_c increases) consistent with theoretical predictions. The circles fall along (or close to) the theoretical curve of constant $Q = 0.05$ demonstrating the ability of the theory to predict the transports, given pairs of gammas measured at any section along the channel. From the simulation, we know the topographic height difference between the three sections. For example, the topographic height of the entrance section (Figure 3.6 (b)) is 0.8 and that of the sill section (Figure 3.6 (c)) is 1. By looking at the location of the green and yellow circles on the curves of constant $\bar{B} - h_0(y)$, we see that the theory also captures the difference in the topographic height (0.2) as the flow moves along the channel from the upstream section (panel (b)) to the sill section (panel (c)).

We ran several simulations with various imposed Q and mass source types.

The results reveal that the theoretical curves in Figure 3.6 are helpful in estimating the transport given pairs of γ_w, γ_c measured at any section along the channel. However, the experiments with different Q values tend to produce different q distributions, and the figure itself is constructed using one constant q value. Changing the constant pv used to construct the graph to some other value (e.g., from $\overline{q_S} = 1.15$ to $\overline{q_E} = 2.08$) results in a similar graph, however the offset of simulation data points (the circles in Figure 3.6(a)) from the theoretical curves changes. Therefore, despite the graph being helpful in interpreting the theory, it is less convenient to be used for model-theory comparison and making transport estimates.

3.4.3 Monitoring sill transport

In order to monitor climate change, it is important to obtain accurate estimates of volume flux at locations upstream of regions of entrainment. Such locations often include the sill itself, where the flow is relatively stable. The number of moorings deployed at sill sections are usually limited and do not provide a complete spatial coverage of the section. The sparse coverage, can sometimes cause an inaccuracy in transport estimates. For example, Jochumsen et al., 2017 provided a revised estimate of transport at Denmark Strait based on corrections they made to their earlier regression methods after a few more moorings were installed. An aspirational goal is to exploit the hydraulic theory to infer transport with minimal number of measurements. Therefore, it is desired to relate the transport at the sills to one (or a few) parameters that can

be measured close to the sill or perhaps at an upstream location. Our simulations showed that the flow in the channel sufficiently far from the entrance is independent of the basin circulation. As a result, upstream measurements of the wetted edges within the channel away from the channel entrance are a good candidate to consider for transport estimation. If measurements are available only at the sill, we can recast the $\gamma_w - \gamma_c$ space into a q-Q space for the critical values of gammas. To do so, equations 3.16 and 3.19 are solved simultaneously to obtain pairs of critical gammas $(\gamma_w^c,\ \gamma_c^c)$ for a range of q and Q values. The two equations are of the general form

$$Q = G_1(\gamma_w^c, \gamma_c^c; q, r) \tag{3.23a}$$

$$J_{\gamma_w,\gamma_c}(G_1, G_2) = J(\gamma_w^c, \gamma_c^c; q, r) = 0, \tag{3.23b}$$

and an example showing curves of constant γ_w^c and γ_c^c in (q, Q) space is depicted in Figure 3.7 (a) for $r = 2/3$. The theory is derived for uniform pv, therefore, from the theoretical point of view, the pv at the sill is the same as anywhere else in the channel. However, this is not true in our simulations where variation in pv is allowed. To compare the uniform pv theory with our simulations, we compute the average pv both near the sill (from $5.5 < y < 6.5$ in equation 3.22) and also upstream (from $2.5 < y < 3.5$ in equation 3.22) to study the sensitivity of the theoretical estimation to the choice of pv in the q-Q space. The yellow symbols in Figure 3.7 (a) refer to the simulation data points when the averaged pv is calculated at the sill. The green symbols refer to the

simulation data points when the averaged pv is considered near the entrance. Notice that there is a predictable drop in pv from the entrance section to the sill section. The shapes of the symbols refer to the mass source type. The values of γ_w^c and γ_c^c for each Q are nearly identical regardless of the inflow type, implying the insensitivity of the flow at the sill to the basin circulation. The theoretical values of γ_w^c and γ_c^c are then compared with the mapped simulation points in the (q, Q) space. The results reveal that the simulated γ_w^c and γ_c^c are well predicted by the theory as shown in Figure 3.7 (b) and (c). The simulated γ_c^c values are less than those of the theory for all the data points. This could be due to the effect of friction in the model resisting the flow tendency to pile up more on the right wall. The simulation-theory difference in estimating γ_w^c and γ_c^c is within 1-11% and 10-20%, respectively, regardless of whether the average pv is considered at the upstream or at the sill section. Running simulations with different friction coefficients (ϵ) revealed that the pv increases slightly as ϵ increases. However, the values of the gammas at the sill remain nearly unaffected. This minimal sensitivity to the choice of averaged pv in (q, Q) space makes Figure 3.7 (a) more promising than Figure 3.6 (a) for the purpose of transport estimation at the critical section as it is less sensitive to the average pv.

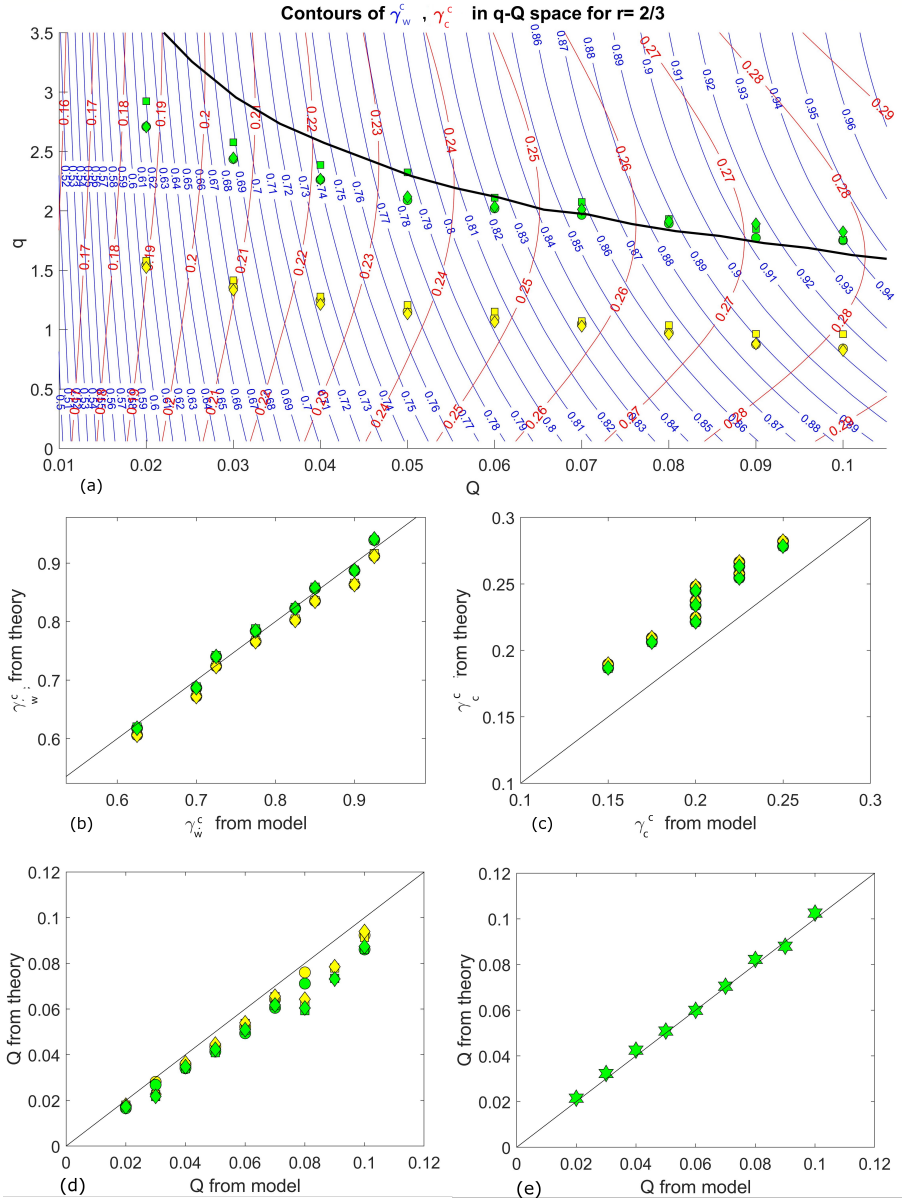

Figure 3.7: Simulation- theory comparison in (q, Q) space. (a) The blue and red contours are the theoretical curves of γ_w^c and γ_c^c, respectively. The circles, squares, and diamonds are the simulation data points at the sill for boundary inflow, uniform downwelling, and localized downwelling, respectively. The thick black curve traces the extrema of γ_c^c curves. (b) and (c) show the theory versus model γ_w^c and γ_c^c, respectively. The colors refer to whether the average pv is calculated near the entrance (green) or the sill section (yellow). (d) The estimated transport from model vs theory obtained by substituting the modeled values of γ_w^c, γ_c^c, and q into equation 3.23 (a). (e) The estimated transport when the critical solution is considered and the pv is eliminated from equation 3.23.

Figure 3.7 (a) suggests various possible monitoring strategies. For example, the first strategy is to measure γ_w^c, γ_c^c, as well as the averaged pv to substitute in the transport relation (equation 3.23 (a)) without using the critical condition (equation 3.23 (b)). To show the sensitivity of the transport estimate to the differences in γ_w^c and γ_c^c from the model and theory, the values of transport from theory are compared with those of the simulations by substituting the modeled value of pairs of γ_w^c and γ_c^c in the theoretical formula for the transport along with a choice of averaged pv. Figure 3.7 (d) shows that the model-theory difference in estimating the transport is within 8-18 %.

The second monitoring strategy exploits the critical condition (equation 3.23 (b)) to eliminate pv, and only measure the γ_w^c and γ_c^c (or equivalently a_c and b_c). Therefore, one can estimate the theoretical pairs of γ_w^c and γ_c^c by finding their intersection from the contours in Figure 3.7 (a), and compare them with the model data points. Since the critical gammas are nearly identical regardless of mass source type, the closest intersections of gammas to the model data points are shown with green stars (the closest intersection to each of them results in the same point). Doing so, results in Figure 3.7 (e) which shows 7% difference between theoretical prediction of Q and the modeled values. The second strategy is more advantageous as it only requires two measurements and provides more accurate estimates by eliminating the need to measure pv. The green symbols in Figure 3.7 (a) fall close to the extrema of the γ_c^c contours (shown by the black thick curve), suggesting that for a given Q, the value of pv is selected so as to maximize γ_c^c. This is true for other parabolic curvatures (both narrow and wide parabolas) we tried and it suggests that (for reasons

unknown) the flow tends to maximize its potential energy. Similarly, Helfrich and Pratt, 2003 found that the flow chooses a pv that maximizes an upstream parameter (upstream height on the right wall in their case). This is advantageous as it suggests a third monitoring strategy allowing for prediction of the overflow transport solely based on measuring one of the wetted edges, a_c or b_c. We replot Figure 3.7 (a) using contours of a_c or b_c as in Figure 3.8 (a). The black curve which marks the extrema of γ_c^c intersects with contours of a_c and b_c which allows for estimating the transport based on only one of the wetted edges as in Figure 3.7 (b) and (c). The spread of simulation data points suggest that measuring a_c is more accurate but less precise, and measuring b_c is more precise but less accurate in comparison to the theoretical result. The difference between model and theory in estimating transport is between 1-15% when the right wetted edge (Figure 3.8 (b)) is used and 5-25% when the left wetted edge (Figure 3.8 (b)) is used to estimate the transport. Note that the third strategy stems from the assumption that the flow chooses a pv along the extrema of γ_c^c, as some of our simulations suggest. This emphasizes the dynamical importance of γ_c^c as the centerline position of the flow for transport estimation.

3.4.4 Application of monitoring strategies to observations at FBC

The theoretical graphs in Figures 3.7 and 3.8 can be used to estimate transport for a given sill section with $r_0 = 2/3$ such as Faroe Bank Channel. Let us begin with the second monitoring method.

The second monitoring strategy, estimates the transport based on the γ_w^c

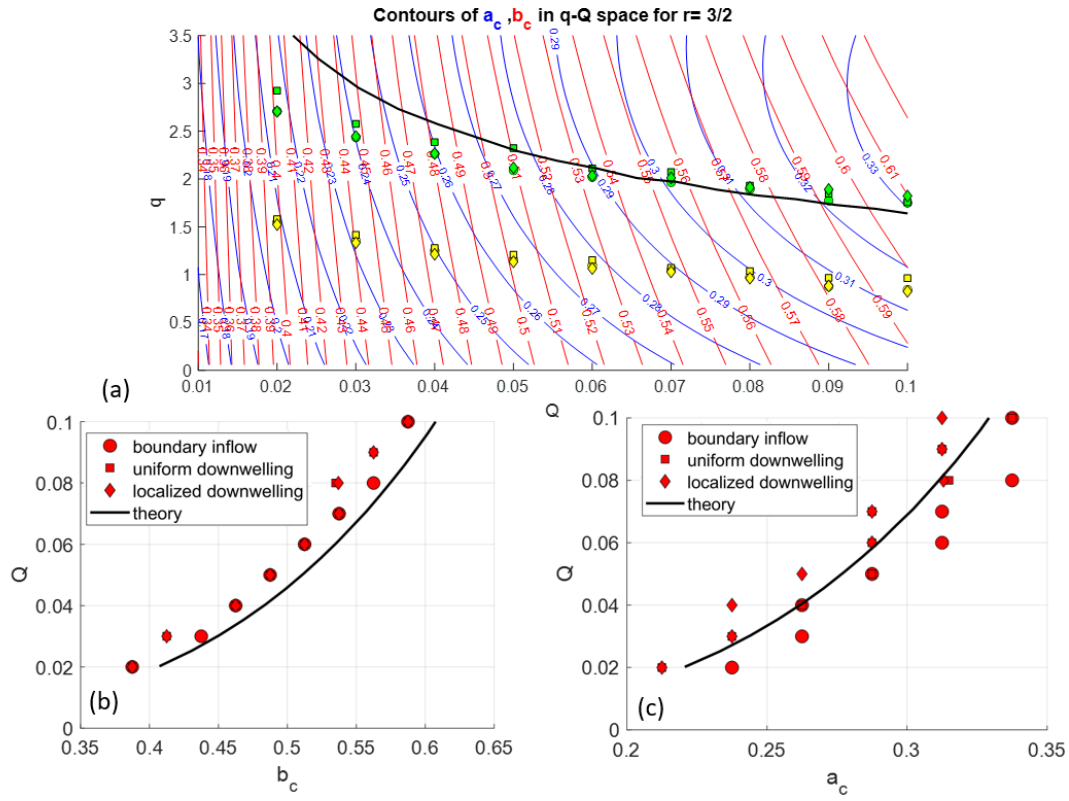

Figure 3.8: (a) Simulation- theory comparison in (q, Q) space. The blue and red contours are the theoretical curves of the wetted edges at the sill a_c and b_c, respectively. The symbols and color codes for the model data points are the same as in Figure 3.7. (b) The transport Q versus b_c for $r_0 = 2/3$. (c) The transport Q versus a_c for $r_0 = 2/3$. The thick black curves in all panels trace the extrema of γ_c^c curves. The red symbols show the model data points that are close to the γ_c^c extrema for different types of inflow.

and γ_c^c. To apply the theory, we first need to fit a parabola to the FBC sill section and find the wetted edges of the flow. Lake, Borenäs, and Lundberg, 2005 made an estimate of interface height at the FBC sill section by fitting an idealized parabolic topography. The wetted edges from their estimate is $a^* = 5\ km$ and $b^* = 8\ km$. They also estimated pv from daily averaged ADCP records (see their figures 11 and 13). The corresponding scaling parameters for FBC are $f = 1.3 \times 10^{-4}\ s^{-1}$, $g' = 0.004\ ms^{-2}$. We use the depth scale $H = 1000\ m$. This results in a deformation radius of $L_d = 16.6\ km$ that can be used to nondimensionalize the wetted edges of the parabolic fit to the Faroe Bank Channel sill section. Therefore, γ_w^c and γ_c^c are 0.78 and 0.18, respectively. If the value of γ_c^c is adjusted by 0.05, this pair of gammas intersect at $q = 2.64$ and $Q = 0.045$. We can recover the dimensional pv and dimensional transport as $pv^* = q \times f/H \approx 3 \times 10^{-7} m^{-1} s^{-1}$ and $Q^* = Qg'H^2/f \approx 1.7Sv$, respectively. These values are within the range of observed values at the FBC.

The first monitoring strategy requires the measurement of pv in addition to the wetted edges. The measured pv within the course of 70 days varies which makes it inherently ambiguous to apply the uniform pv theory. However, considering an average pv of $3 \times 10^{-7} m^{-1} s^{-1}$ yields the same results as the first monitoring strategy. Choosing a higher or lower averaged pv, between $2 - 4 \times 10^{-7} m^{-1} s^{-1}$ changes the estimated transport of $1.7Sv$ only by about 5%.

The third monitoring strategy eliminates the need to measure both wetted edges. Let us assume that only the left wetted edge ,$a^* = 5\ km$, is provided from observations. Considering the same $L_d = 16.6\ km$ from the scaling

parameters discussed earlier, the nondimensional wetted edge is $a = 0.3$. Figure 3.8 (c) gives $Q = 0.069$, therefore, $Q^* = 2.5sv$. Similarly, if only the measurement of the right wetted edge is available, then $b = 0.48$ yields $Q = 0.045$ from Figure 3.8 (b) and the dimensional transport is $Q^* = 1.7sv$.

3.5 Summary and Discussion

The dense flows in many deep passages in the ocean are the result of the funneling of much broader watermasses through narrow gaps and are often hydraulically controlled. Both these factors render the sites advantageous for long-term monitoring of transport. One goal of hydraulic theory is to estimate transport using the minimal number of measurements. Previous theoretical studies have been restricted to zero or uniform pv and to channels with rectangular cross sections. In this paper we explored the effect of continuously varying (parabolic) channel geometry on the rotating hydraulic behavior of a channel and basin system. To do so, we extended the existing theory for the parabolic channel (Borenäs and Lundberg, 1986) by creating a graphical representation that shows the solution behaviour more easily and by exploring different strategies for overflow monitoring. We also used a 1.5-layer, reduced-gravity numerical model of coupled basin-strait flow, thus freeing ourselves from the restriction of uniform pv and semi-geostrophic dynamics.

The results revealed some similiarities and some differences to rectangular channels in the flow structure and properties. Helfrich and Pratt, 2003 found that the flow in the rectangular channel with a specified width and imposed Q is independent of the mass source distributions in the basin. In the parabolic

channel the sensitivity of the flow to the mass source depends on the curvature of the parabola. The basin circulation intrudes more into the channel for parabolas with $r_0 \geq 2/3$. The intrusion extends from the entrance to up to one third the distance to the sill, but the flow further downstream and at the sill remains unaffected by the basin circulation, similar to the case of the rectangular channel. The flow characteristics in narrow parabolas are very much similar to the rectangular channel with little sensitivity to the basin circulation even near the channel entrance. The flow generally enters the channel from the left wall for both the rectangular and parabolic bottom topography. However, the parabolic geometry directs the flow to the center of the channel faster than the rectangular channel does (e.g., compare Helfrich and Pratt, 2003 Fig 3. (b) with the Figures 3.2 (d) and 3.5 (c)) so that a cell of recirculating fluid can arise in the left portion of the channel, just downstream of the entrance. Unlike the rectangular geometry, the parabolic cross section results in larger pv variations in the channel because of interface grounding. This makes direct comparison of simulation with uniform pv theory more difficult.

We recast the volume flux formula and Bernoulli potential in terms of variables such as the flow width and the position of the flow centroid for a given geometry. This illuminates the flow evolution and hydraulic control theory in the channel. We establish a dynamical connection between the sill section and the overflow transport by proposing three monitoring strategies. The strategies require measuring the intersection of the overflow interface height with the bottom at the sill section. The first method does not involve

solving the critical condition but it requires computing γ_w^c and γ_c^c from the measurement of the two wetted edges and also an estimate of averaged pv. The second method eliminates the need to provide pv measurements by solving the critical condition and only requires finding both wetted edges of the flow at the sill section. The third monitoring strategy requires only measuring one of the wetted edges. The comparison between simulation data points and the model suggests that the second monitoring strategy is more accurate. It is also more advantageous than the first monitoring strategy as it eliminates the error associated with inserting an average pv value in the uniform pv theory. The third monitoring strategy requires only one measurement, either the left or the right wetted edge. The third method is more accurate than the first method, and has the same range of accuracy as the second method. Measuring the right wetted edge yields a better agreement between simulations and theory than the left wetted egde. Although the third monitoring strategy is advantageous as it requires making only one measurement, it relies on the assumption that the pv of the flow is chosen (such that γ_c^c is maximized). Therefore, the second monitoring strategy makes fewer assumptions.

The pioneers of rotating hydraulics theory focused on relating the volume flux to hydrographic measurements made upstream of the sill. The motivation was mostly to avoid the difficulty of making direct observations at the sill section itself. Given that for major sills and passages in the global ocean, the modern monitoring and measurements are made at the sill section, it can be more advantageous to focus on relating the transport to the measurements made at the sill itself. All transport relations suggested in the literature assume

steady state condition. However, the conditions downstream of a sill are often turbulent and time-varying. Therefore, one advantage of monitoring the overflow at the sill is that flow there is being squeezed through a very small cross section and therefore less coverage is required to resolve the stream. The second advantage of estimating transport based on sill measurements is that the flow at the sill is hydraulically controlled.

As a result, theoretical predictions can provide a more accurate estimate of the transport. Our results revealed that for a continuously varying topography, the flow near the channel entrance is influenced by various mass source types and basin circulation. Therefore, relating the transport to upstream measurements may be less accurate compare to measurements made at the sill. We applied the three monitoring strategies to the case of Faroe Bank Channel and the results showed that the estimated transports are within the range of observed values. One issue with all three monitoring strategies is the practicality of finding the interface height from observations, and deploying instruments close to the bottom especially for passages with complex geometries. Nevertheless the theoretical progress still provides a transport estimate consistent with simulations and observed values with only 1-3 measurements and worth exploring in more complex models as a potential approach to enhance observing systems.

Chapter 4

Effect of Hydraulic Control on the Volume Flux Variability

> Oh the lover's home, spring
> zephyr comes thence
> be prompt and seize it,
> rhapsody's thine hence.
>
> Hafez, the Divān.

4.1 Introduction

Overflow transport at different passages in the global ocean can vary on different time scales such as seasonal and interannual. The exchange flow at the Bab al Mandab sill in the Red Sea is variable. The transport of the dense overflow at Bab al Mandab is strongly influenced by seasonal and intraseasonal variations in wind forcing with much weaker summer outflow (Peters et al., 2005). Pratt et al., 2000 studied changes in the hydraulic character of the flow at Bab al Mandab sill due to the strong time-dependent flow. The exchange flow through the Strait of Gibraltar is also variable (Bray, Ochoa, and Kinder, 1995).

Sannino et al., 2014 developed hydrostatic σ-coordinate and non-hydrostatic z-coordinate models of the exchange flow through the Strait of Gibraltar to study the role of nonlinearity and accuracy of hydrostatic assumption on the high amplitude internal solitary waves progressing toward the Mediterranean. They also studied the hydraulic behavior of the exchange flow to map the locations where the flow is subcritical, critical, and supercritical to evaluate the impact of the nonhydrostaticity on the simulated hydraulic regime (Sannino et al., 2014). Another example is the transport variability at the Faroe Bank Channel (FBC). Observations suggest that there is a seasonal variability in volume transport at FBC with maximum in August and minimum in February. The average transport of dense water ($\sigma_\theta > 27.8\ kgm^{-3}$) for the 1995-2005 period is 1.9 sv. The seasonal amplitude is about 10% of the average transport (Østerhus et al., 2008). In Chapter 3, we studied the hydraulically controlled flow at the sill section for a parabolic channel geometry and suggested monitoring strategies that relate transport to measurements made at the sill. The inflow transport was assumed to be constant. The sources of the overflows can vary in time which can result in variability in the total overflow transport. The variability in the overflow transport can happen at different time-scales for various sea straits. For example, in Chapter 2 we discussed multiple sources of Denmark Strait Overflow (DSO) and the volume transport of 3.2 Sv that varies by $\pm$ 0.5 Sv. The seasonal variability at Denmark Strait is weak and explains only about 5% of the variance in transport (Jochumsen et al., 2017). However, the transport of the DSO sources vary on intraseasonal time scales, and they tend to compensate each other such that the total transport remains fairly steady (Harden et al., 2016). At Faroe Bank Channel observations exhibit

a clear seasonality of about 0.25 Sv with average transport of 2.2 (Hansen et al., 2016).

This chapter aims to address the following questions: How does hydraulic control affect the variability in transport observed in the real world? Does hydraulic control suppress the seasonal signal in the overflow transport? Does narrowing and shallowing of topography lead to a local suppression of time dependence and, if so, to what extent does hydraulic control play a role?

To the best of our knowledge, there is no literature available on this topic. However, Pratt and Whitehead, 2008 discusses the time dependent flow and how disturbances generated upstream propagate for a hydraulically controlled versus subcritical flow. Pratt and Chechelnitsky, 1997 studied the upstream effects of the sill such as wave reflection with the purpose of providing insight for parameterization of unresolved constrictions in General Circulation Models. Helfrich, 1995 developed a theory for a hydraulically-controlled two-layer flow without rotation with gradual time dependence. They applied the theory to the Strait of Gibraltar and discussed the importance of time dependence in sea straits.

4.2 Methodology

To answer the question about the relationship between the hydraulically controlled flow and seasonal variability, we need to impose a time varying transport with seasonal periodicity in the upstream basin and study how the amplitude and frequency of the transport changes in the basin, along the channel, and at the sill section after time-dependent adjustment takes place.

To examine the effect of hydraulic control on the suppression of time dependence in the imposed transport, we run two series of experiments: (i) The flow is hydraulically controlled at the sill section (similar to what we had in chapter 3). (ii) The flow is subcritical at the sill after time dependent adjustment takes place. For both series we first impose constant boundary inflow. Then we impose simple time varying inflows such as sinusoidal functions. Lastly, we move on to the experiments with forcing amplitude and frequency that more realistically mimic the seasonal cycle. The numerical model we used for this study is explained in Chapter 3. The geometry carried out in this chapter is for a parabolic topography with $r_0 = 2/3$ (as in chapter 3) resembling FBC. We set up the model with a time-dependent imposed transport of the form $Q = Q_0(1 + A_0 sin(2\pi\ t/T))$. The $Q_0 = 0.05$ for all simulations. We explore ranges of values for A_0 and T in simulations listed in Table 4.1. The value of Q_0 and A_0 are chosen such that the value of transport remains roughly within the range of observed transport variability at FBC.

To create a subcritical flow, we made the channel 3 times longer and added a second sill at $y = 24$. The first sill has the same height as the simulations in Chapter 3 (sill height is $h_0 = 1$). The height of the second sill crest is higher than the first sill by 0.1 (about 100 m in dimensional scale) to ensure that the flow at the first sill remains subcritical.

To determine a proper forcing period, T, that has relevance to the seasonality of the Nordic Seas, we first find the intrinsic time scales for the upstream basin in our model in comparison to the size of the Nordic Seas basin. This is

done by matching the time-scale ratios between the Nordic Seas and the model basin. The residence time for the overflow water in the Nordic Seas is on the order of a couple of years. Considering one of the basins and strait systems, e.g. Iceland Sea and Denmark Strait, or Greenland Sea and the FBC, the residence time is roughly about 1-2 years. Therefore, the ratio of the seasonal time-scale to the residence time for the Iceland Sea (or Greenland Sea) is roughly $T_s/T_r = 365\ day/365\ day = 1$ or $T_s/T_r = 365\ day/(2 \times 365\ day) = 1/2$. For the model basin-channel system, the residence time of the basin is about 90 days, that is about 1000 in nondimensional time-scale. The ratio of the forcing period, T, for the model to the residence time, T_r, for the model basin should roughly match that of the Nordic Seas. Therefore, the appropriate period of the seasonal forcing in our model is between 500 and 1000. The Kelvin wave circumnavigation time in the basin is also computed and considered as another fundamental time to be used as the forcing period. Since the basin has sloping bottom, it is not straightforward to compute the exact Kelvin wave circumnavigation time scale, but its value is approximated by dividing the perimeter of the basin to the phase speed ($\sqrt{g'H}$). The value is about $T = 45$ (3.5 days in dimensional time scale) which is close to the basin's natural mode of oscillation that freely arises in the basin (this is discussed more in the Results). The period $T = 4000$ is also considered only to see the response of the basin-channel system to a low frequency forcing mimicking the interannual time scale. Since the observed seasonal amplitude of variation in transport at FBC sill section is about 10%, the variability in the upstream basin is presumably larger. A ranges of amplitudes between 10-75% are used for the forcing, but only simulations with amplitudes $A_0 = 0.25$ and $A_0 = 0.75$ are discussed

here (changes in the forcing amplitude does not make a significant difference in the results).

Observations suggest that the dense water formation in the Nordic seas does not occur year-around. The annual average outflow of dense water is about 6 Sv (Drange et al., 2005). The dense water is formed mostly in the winter over an intense period and is zero for the rest of the year (Aagaard, Swift, and Carmack, 1985; Ronski and Budéus, 2005). To mimic this behavior, we also run simulations in accordance with the time variability associated with the formation of overflow water in the upstream basin. This is done by setting a periodic forcing in Gaussian form. The mean and variance of the Gaussian function (listed in Table 4.1) is computed such that the same inflow to the basin is distributed over 4 months and is zero for 8 months. This cycle is repeated 3 times to account for 3 seasonal cycles. The amplitude of forcing is set such that the area under the Gaussian, that is the total (time-integrated) transport for 12-months period to be nearly the same as the value for other experiments in the same time range.

Table 4.1: The experiments are listed in the first column. The subscript c refers to hydraulically controlled flow regime and the subscript s refers to subcritical flow regime. The forcing type, amplitude, and forcing period are listed in the second column and third columns. The fourth column shows the ratio of the volume transport measured at the sill to that of the inflow at the boundary in the upstream basin. The fifth column shows the corresponding phase lag. The last two columns are discussed in the results.
* For the Gaussian forcing $\mu_1 = 1167$, $\mu_2 = 5167$, and $\sigma = 333$ take place of A_0.
$^+$ The period for the Gaussian is 4000.

ID	forcing type	A_0	T	amplitude ratio	phase lag (°)
A_c	constant	0.25	0	-	-
A_s	constant	0.25	0	-	-
B_c	periodic, sinusoidal	0.25	1000	0.58	40.3
B_s	periodic, sinusoidal	0.25	1000	0.73	35.6
C_c	periodic, sinusoidal	0.75	1000	0.54	42
C_s	periodic, sinusoidal	0.75	1000	0.57	34.14
D_c	periodic, sinusoidal	0.25	500	0.45	58.75
D_s	periodic, sinusoidal	0.25	500	0.65	34.8
E_c	periodic, sinusoidal	0.25	4000	0.8	9.63
E_s	periodic, sinusoidal	0.25	4000	0.96	10.69
F_c	periodic, sinusoidal	0.25	45	0.49	252
F_s	periodic, sinusoidal	0.25	45	0.96	219
G_c	periodic, Gaussian	*	$^+$	0.79	57.2
G_s	periodic, Gaussian	*	$^+$	0.78	64.9

4.3 Simulation results

We first compare simulations A_c and A_s with constant imposed transport. Panels (a) and (c) in Figure 4.1 show the interface height contours in the basin-channel system and panels (b) and (d) show the height along the centerline of the channel. When the flow is hydraulically controlled the boundary current

that moves along the right wall of the basin ($x < 0$) goes around the basin toward the left side ($x > 0$) before approaching the mouth of the channel (Figure 4.1 (a)). When the flow enters the channel, it continues along the left wall ($x > 0$), goes over the sill (at $y = 6$), and then diverts to the right side ($x < 0$). When the flow is subcritical, the boundary current approaches the entrance of the channel faster. The flow does not divert to the right side of the channel until it reaches the second sill (Figure 4.1 (c)). The interface height in the middle of the channel (Figure 4.1 (b) and (d)) has a dip near the entrance between $1 < y < 2.5$ in both cases. There is a permanent decrease in the layer thickness over the sill in the controlled case (Figure 4.1 (b)), whereas in the subcritical case the temporary change in the layer thickness (the ripples) change position along the channel even after the time dependent adjustment takes place (Figure 4.1 (d)). Note that the interface height is higher by about 0.15 when the flow is subcritical.

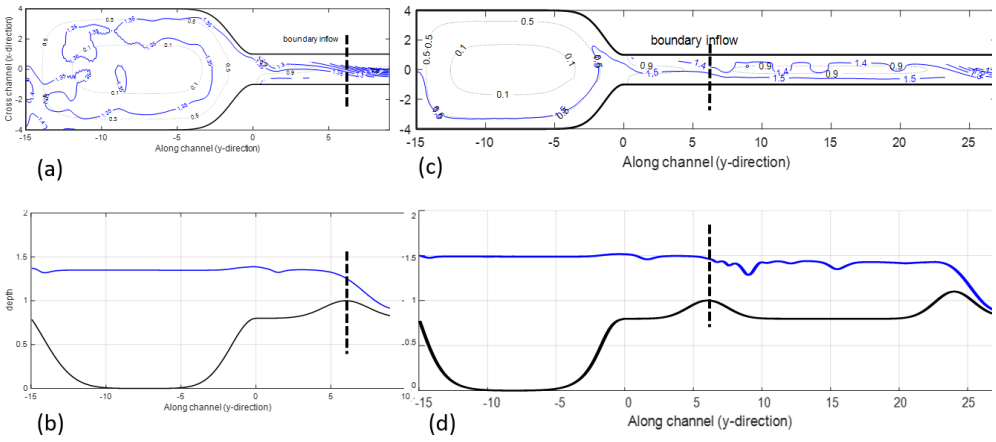

Figure 4.1: Panels (a) and (c) show the contours of interface height for simulations A_c and A_s. Panels (b) and (d) show the interface height along the channel centerline for simulations A_c and A_s.

The changes in transport Q as a function of time is shown in Figure 4.2 at

the far-left boundary where the flow enters the basin at $y = -15$ (black curve), in the middle of the channel at $y = -8$ (red curve), and at the sill sections $y = 6$ and $y = 24$ (the blue and green curves). For both cases of subcritical and the hydraulically controlled simulations the flow in the basin reaches the constant imposed value of $Q = 0.05$ by about $t = 3000$. The zoomed window shows that the amplitude of oscillation in the basin is larger for the subcritical flow (Figure 4.2(d)) than the controlled flow (Figure 4.2(c)). The basin's high frequency oscillation is damped when it reaches the sill but the suppression is stronger when the flow is hydraulically controlled. This can be seen by comparing the blue curves in Figures 4.2(c) and (d). We can also see the suppression in amplitude due to hydraulic control by comparing the blue and green curves in Figure 4.2(d) since the flow is subcritical over the first sill and critical over the second sill. In general, we can see that making the channel longer and the flow subcritical, makes the flow more variable. We omit showing the transport signal at the open boundary where the flow exits the domain (because it nearly coincides with the transport signal at the sill).

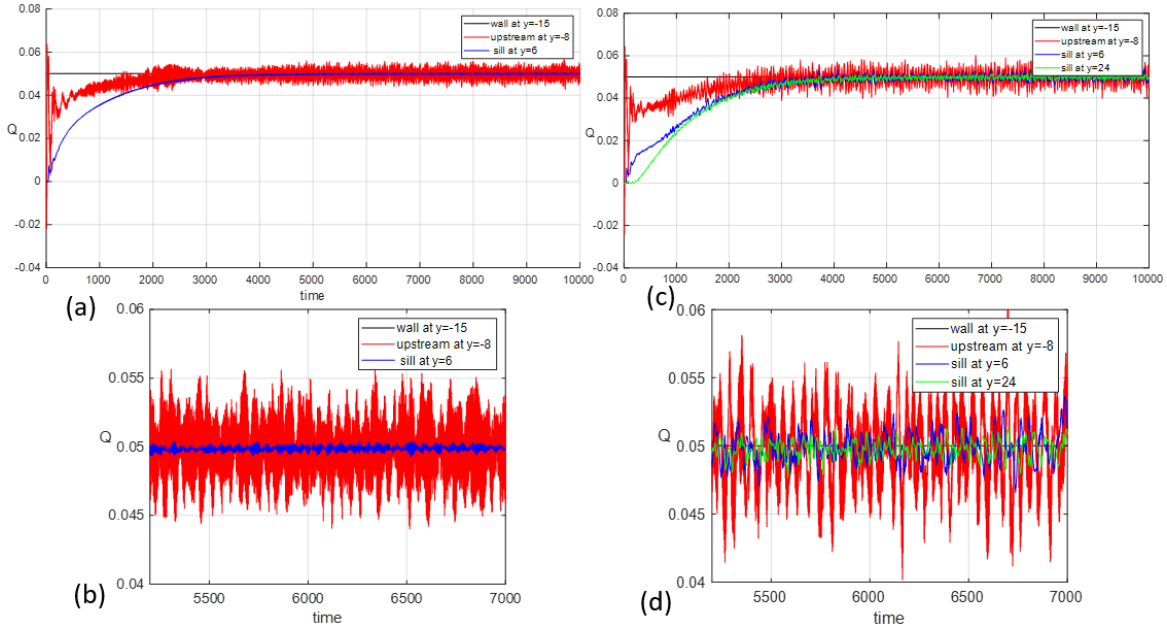

Figure 4.2: (a) and (c) Q vs time for similations A_c and A_s. (b) and (d) are the zoomed view of the time series.

With the insight we obtained from the effect of the flow regime on the layer thickness, we now can compare simulations B_c and B_s with periodic imposed transport. The black curves in Figure 4.3 show the imposed periodic forcing where the flow enters the basin. The time dependent adjustment begins at $t = 0$ and takes place between then and $t = 2000$ (which is earlier than what we observed for simulations A_c and A_s with constant forcing). The flow in the basin oscillates mainly with the forcing frequency but also has a high frequency oscillation that arises freely within the basin. It is not trivial to know what mechanism is responsible for the rapid oscillations. The analysis in the frequency domain (discussed in the following section) suggest that the rapid oscillation is potentially associated with the Kelvin wave propagation and is

present in the case of constant forcing as well (see simulations A_c and A_s in Figure 4.2). The Kelvin waves are generated by the boundaries of the basin's topography. The rapid oscillation could also be excited by an instability in the flow. The amplitude of the rapid oscillation decreases when the forcing is in its decreasing phase. Both the high and the low frequency motions are damped by the time the flow reaches the sill. However, the high frequency signal is more strongly damped for the hydraulically controlled case (Figure 4.3 (a) and (b)). The damping of the signal at the sill is partly due to the narrowing and shallowing of the strait as the sill is approached, but the hydraulic control causes some additional suppression of the signal.

To be able to compare and quantify the damping in the signal between different flow regimes with different forcing parameters, an amplitude ratio is defined. The ratio of the amplitude of the transport signal at the sill to the amplitude of forcing for the low frequency motion is computed as:

$$\frac{max(A_{sill}) - min(A_{sill})}{max(A_{inflow}) - min(A_{inflow})} \tag{4.1}$$

where A_{sill} and A_{inflow} are the amplitudes of the transport signal at the sill and at the left wall where the flow enters the basin. The magnitude of amplitude ratio is listed in Table 4.1 for each experiment. The amplitude of high frequency oscillation in the basin decreases when the magnitude of the periodic forcing approaches its minimum. This is only true when the flow is hydraulically controlled.

The forced oscillation at the sill has a time lag regardless of flow regime. The time lag between the forcing and the sill signal is quantified in degrees

and noted in the Table 4.1.

At the second sill in simulation B_s, we see further reduction in the high frequency amplitude. The low frequency amplitude is not changed very much at the second sill, but its phase is delayed in comparison to the first sill.

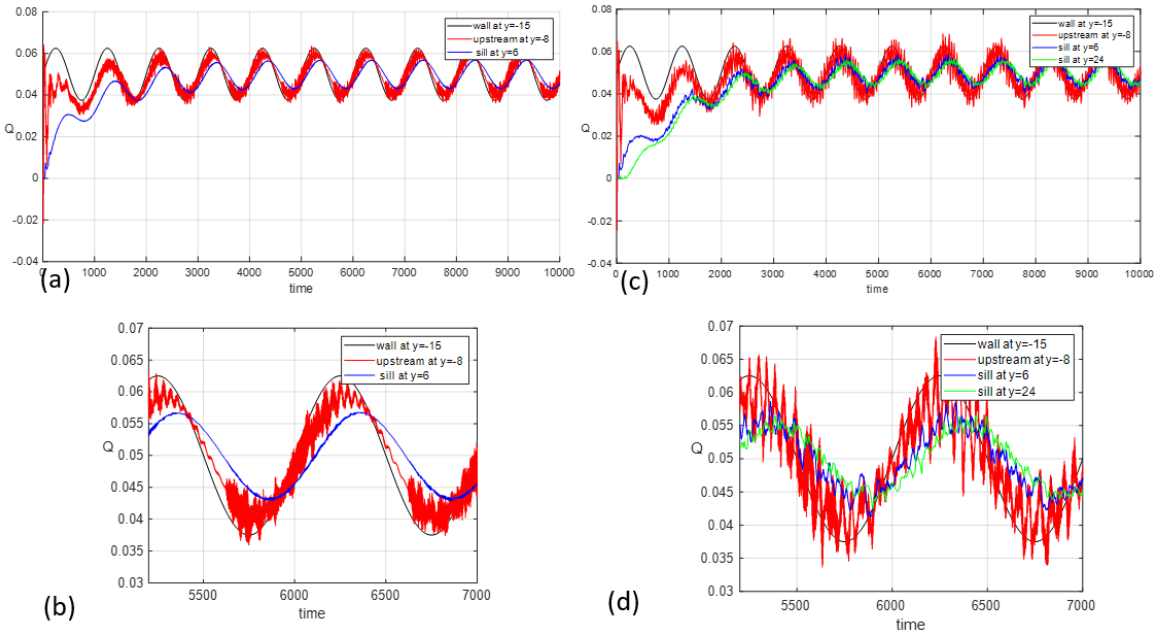

Figure 4.3: (a) and (c) Q vs time for similations B_c and B_s. (b) and (d) are the zoomed view of the time series.

To see the effect of forcing and flow regime on the interface height profile in the channel, the interface height near the entrance and at the sill section are plotted in Figures 4.4 and 4.5, respectively. The interface heights are plotted for the subcritical and hydraulically controlled flow with constant and periodic forcing. The interface height both at the entrance and at the sill are higher in the subcritical simulations than the hydraulically controlled simulations regardless of the type of forcing. When the forcing is periodic and the magnitude of the periodic forcing is at its minimum, the interface height

is slightly lower across the section at the entrance than when the forcing is constant, regardless of the flow regime (the solid curves are below the dashed curves in Figure 4.4 (a)). Similarly, when the periodic forcing is at its maximum the interface height stands slightly higher across the section at the entrance (solid curves are above the dashed curves in Figure 4.4). Although the interface is plotted for two specific peak and trough of the periodic forcing, the result is representative of other peaks and troughs after time adjustment takes place. This is not entirely true at the sill section in Figure 4.5. When the flow is subcritical, the interface height in relation to the forcing is different across the section (compare the blue curves in Figure 4.5 (a) and (b) for $x > 0$ versus $x < 0$). But in general, the changes in the interface due to the phase of the forcing is minimal in comparison to the changes due to the flow regime.

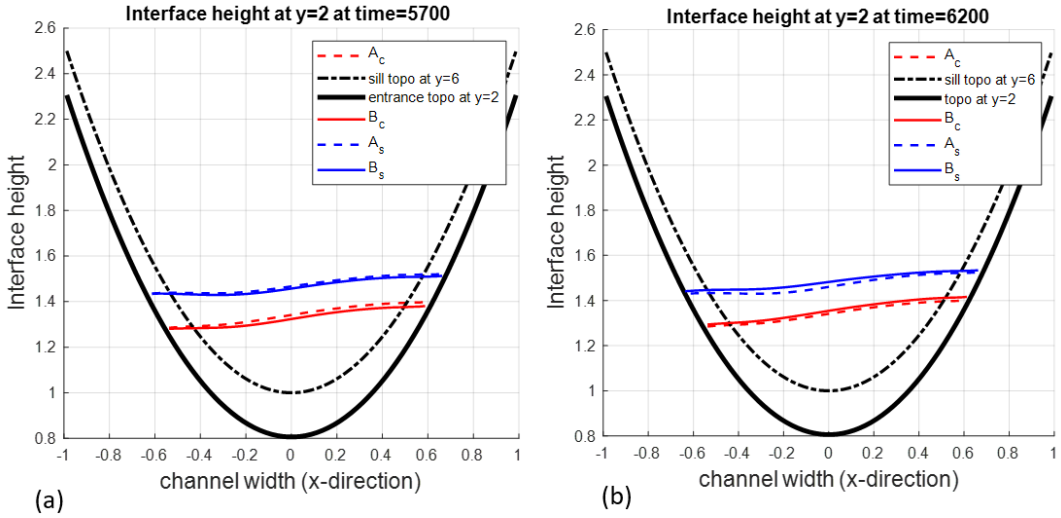

Figure 4.4: The interface height at $y = 2$ near the channel entrance for simulations A_c, A_s, B_c, and B_s. Panels (a) and (b) correspond to the height at the minimum and maximum of the periodic forcing, respectively.

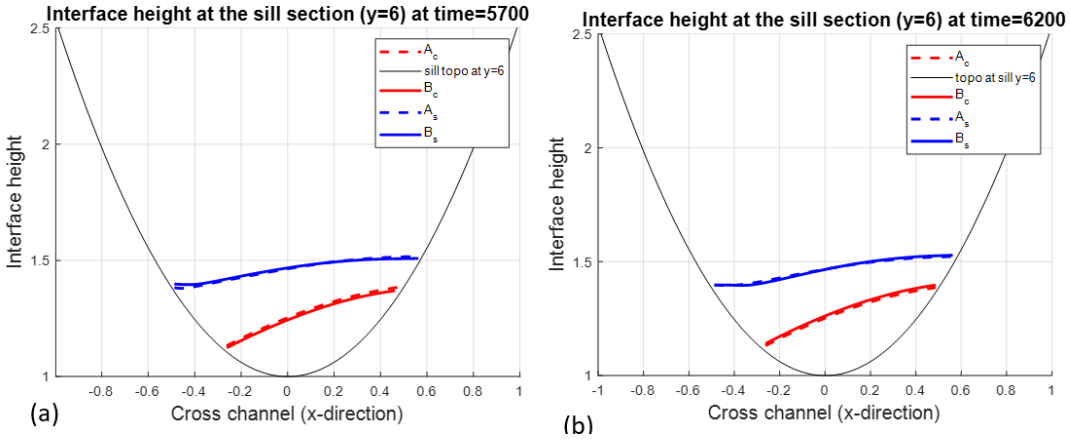

Figure 4.5: The interface height at the sill section at $y = 6$ for simulations A_c, A_s (dashed curves), B_c, and B_s (solid curves) (a) at $t = 5700$ when the forcing is at its minimum and (b) at $t = 6200$ when the forcing is at its peak.

The interface height along the centerline of the basin and the channel is plotted for all simulations in Figure 4.6. The interface is lower for the controlled cases than the subcritical simulations. The shape of the interface in the basin and near the mouth of the channel is similar regardless of forcing and flow regime. However, for the controlled simulations the profile of the water height permanently has changed. For the subcritical flow the ripples are formed after passing the first sill. These ripples are reminiscent of the stationary waves generated due to the flow going over two consecutive obstacles of nearly the same height (Pratt, 1984). The location of the ripples does not follow any specific pattern in relation to the phase of the periodic forcing.

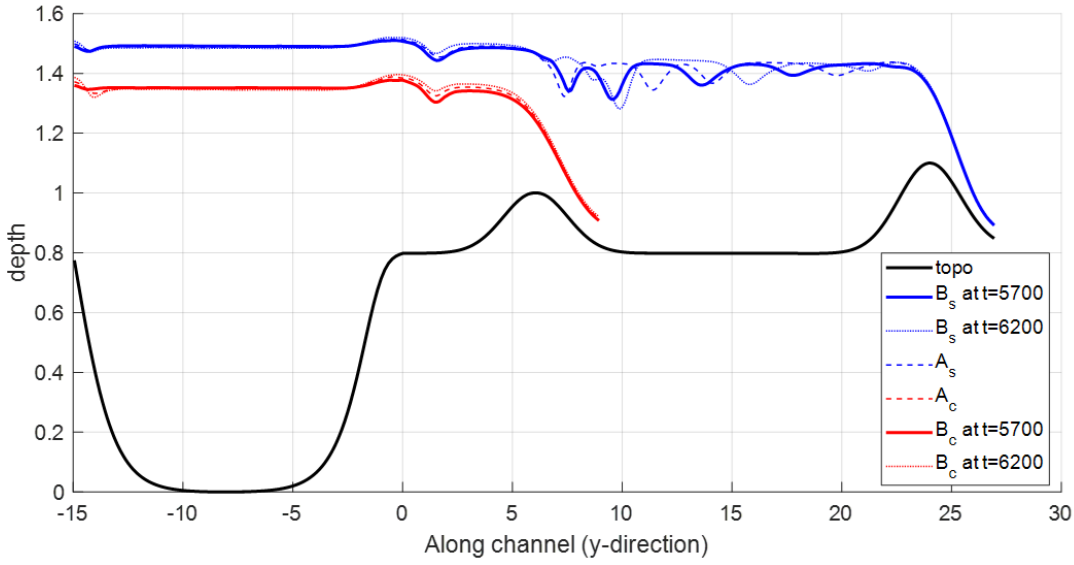

Figure 4.6: The interface height along the centerline for simulations A_c, A_s (dashed curves), B_c, and B_s at $t = 6200$ (dotted curves) when the forcing is at its peak and $t = 5700$ (solid curve) when the forcing is at its minimum.

To see the evolution of the transport signal from the basin to the sill, the basin and the sill response functions for the subcritical flow are plotted together in the frequency domain as in Figure 4.7. The basin and the sill both experience the same spectral range but the amplitude of oscillation at each frequency is different. The amplitude of oscillation at the forcing frequency ($\omega = 0.001$) is slightly higher in the basin than at the sill. The basin has its second large peak at around $\omega = 0.023$ which is about 3.8 days in dimensional magnitude. This value is nearly equal to the time it takes for Kelvin waves to go around the periphery of the basin. The range of spectrum is similar for the hydraulically controlled case, but the amplitudes both in the basin and at the sill are smaller (not shown here).

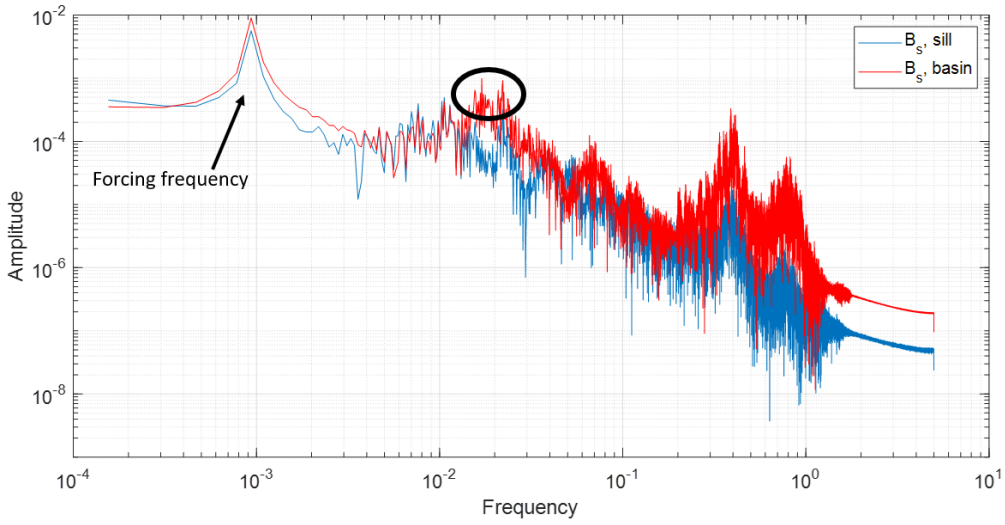

Figure 4.7: Transport signal in the frequency domain for simulation B_s in the basin (red) and at the sill section (blue). The oval highlights the Kelvin wave frequency in the basin.

To better understand the effect of flow regime on the variability in transport at the sill, we look at the transport signal in the frequency domain as in Figure 4.8 (a). The highest peak in the spectrum is at the forcing frequency $\omega = 10^{-3}$ and its magnitude is nearly the same for both the subcritical and the hydraulically controlled flow. Both flows experience the same spectral range, but consistent with the previous plots, the amplitude of variability at the sill for the subcritical flow is higher than that of hydraulically controlled flow. The peaks in the frequency range of $0.01 < \omega < 0.1$ are associated with Kelvin waves as it was seen earlier in Figure 4.7.

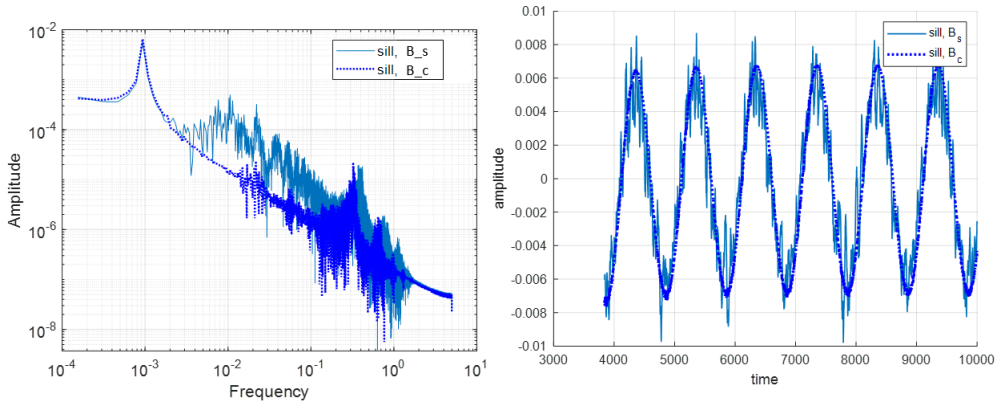

Figure 4.8: (a) The sill signal in the frequency domain (b) in the time domain for the case of controlled and subcritical flow, simulations B_c and B_s.

All the simulations shown until now have the period of $T = 1000$. The second time scale we consider is $T = 500$. As discussed earlier, this is chosen based on the assumption that the ratio of T_s/T_r is $1/2$. The overall behavior of the signal does not change by reducing the period from 1000 to 500 (therefore, I skip showing any image here). To see the effect of large forcing period, $T = 4000$ that is four times bigger than the residence time of the basin is also considered. Again, the overall behavior of the response signal at the sill and the basin is the same as previous forcing periods.

The Kelvin wave circumnavigation time scale around the basin, $T = 45$, is used as the period of forcing in simulations F_c and F_s listed in Table 4.1. Results show that the oscillation both in the basin and at the sill have a higher amplitude when the flow is subcritical than when it is critical. Also, notice that when the forcing is near its minimum, the sill response is close to its maximum for both simulations. The phase lag between the forcing and the response at the sill is larger in simulations F_c and F_s than in the previous simulations

with lower forcing frequencies. But consistent with the previous simulations, the phase lag is larger for the hydraulically controlled experiment than the subcritical flow.

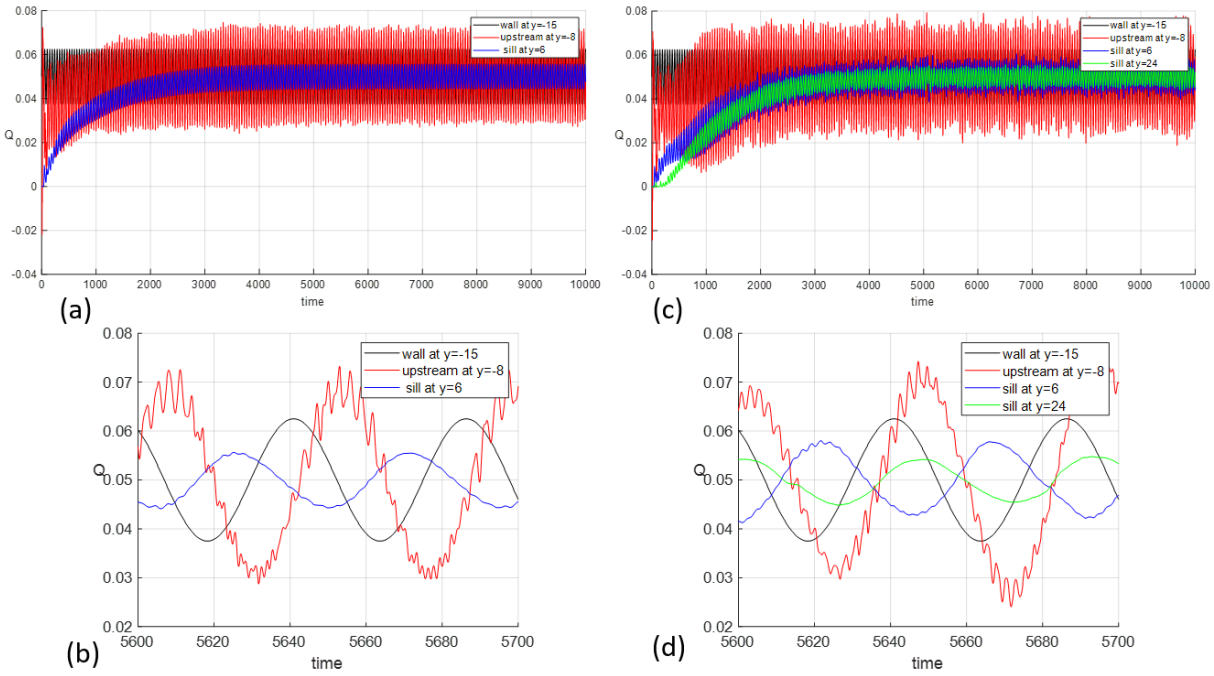

Figure 4.9: Q vs time for the (a) controlled and (b) subcritical flow with the period of $T = 45$ (simulations F_c and F_s).

To mimic the seasonal cycle of the Nordic Seas, the boundary inflow in the basin is imposed as a Gaussian function. The inflow is supplied over 4 months period with a peak at the second month and is zero over 8 months. As shown in Figure 4.10, this is done for three seasonal cycles to see the behavior of the response and to ensure that a time dependent adjustment takes place. The response functions in the basin and in the channel (at the sills and at the right wall where the flow exits the domain) closely follow the imposed Gaussian function of the inflow. For both flow regimes (hydraulically controlled and

subcritical) when the inflow decreases to zero (at approximate intervals of $2000 < t < 4000, 6000 < t < 8000, 10000 < t < 12000$), the transport at the sill gradually decreases but does not vanish. Similar to previous experiments, the high frequency oscillation in the basin is stronger in the subcritical flow than the hydraulically controlled flow. The maximum amplitude of the response function at the sill is nearly the same for the hydraulically controlled flow and the subcritical flow (see Table 4.1). The phase lag between the forcing and the sill response is larger for the controlled flow than the subcritical flow.

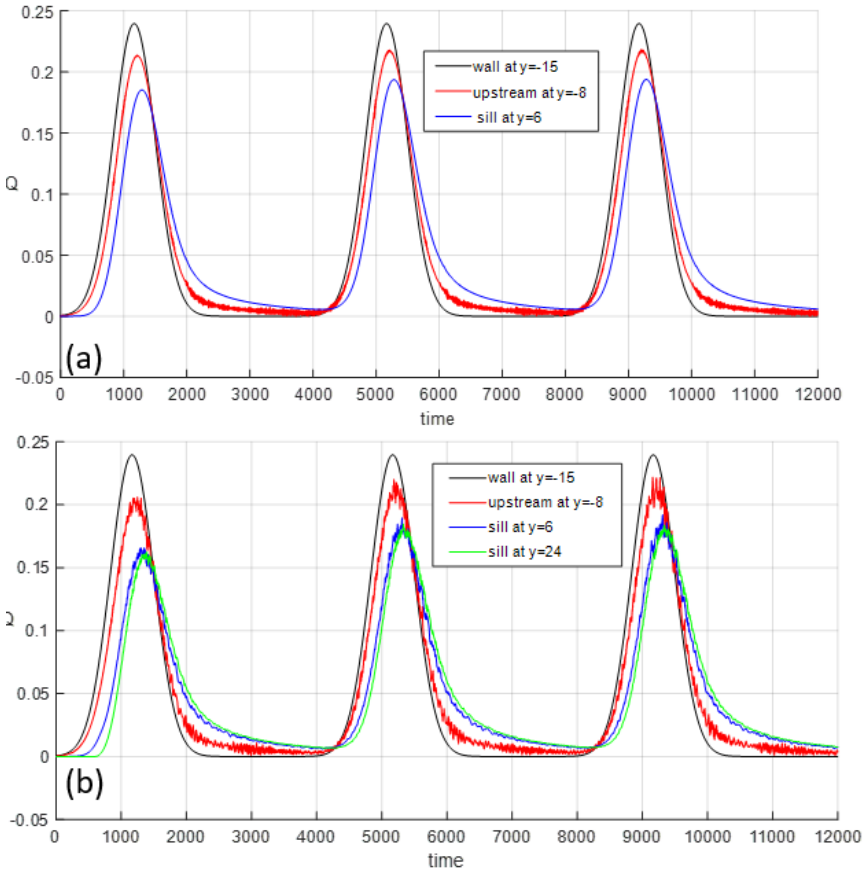

Figure 4.10: Q vs time for the (a) controlled and (b) subcritical flow with a Gaussian seasonal cycle (experiments G_c and G_s).

The transport signal at the sill in frequency domain (Figure 4.11) shows a higher amplitude for the subcritical flow than the controlled flow in frequency range of $\omega > 0.002$.

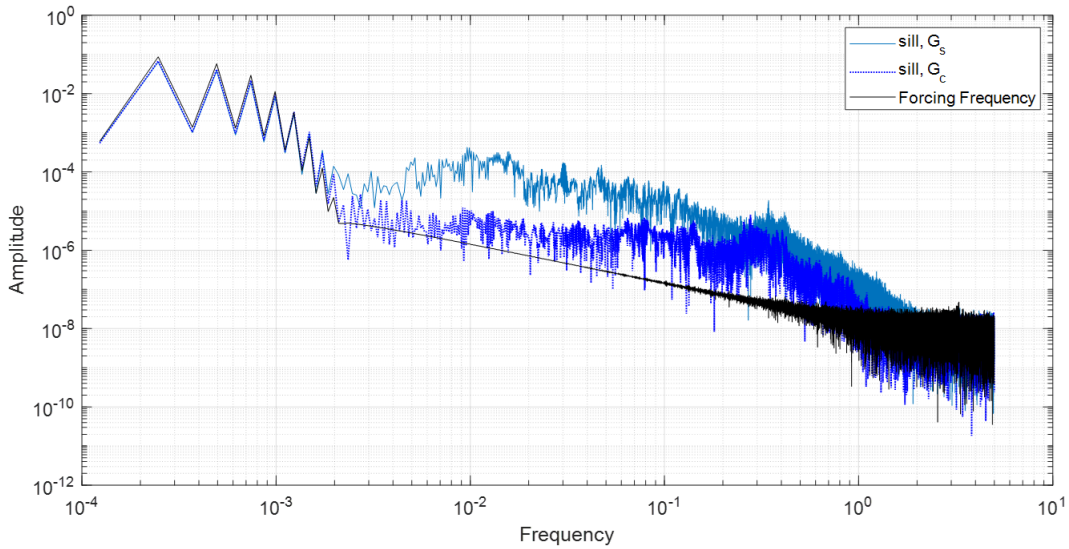

Figure 4.11: The sill response in frequency domain for simulations G_c and G_s.

To see the effect of forcing on the flow in the basin and the channel, the flow along the centerline of the channel is plotted in Figure 4.12. When the forcing is at its maximum ($t = 9120$, dotted curves), there is a depression in the interface height in the basin but the interface is maximized at the sill. When the forcing is at its minimum ($t = 11040$, solid curves), the interface height in the basin bulges upward, but the interface height is minimized at the sill. This is true regardless of the flow regime. This seesaw behavior between the upstream basin and the channel upstream of the (first) sill resembles Helmholtz oscillation. The oscillation is set by the water level going up in the basin while it goes down in the channel (or vice versa). The interface height

at the entrance of the basin experiences a sudden increase (at $y = 0$) for both experiments at all time steps. This is due to the shallowing of the topography at the entrance of the channel in addition to the increase in the parabolic curvature at the channel entrance. The interface height for the subcritical flow is higher than the hydraulically controlled flow at all times, consistent with the previous simulations.

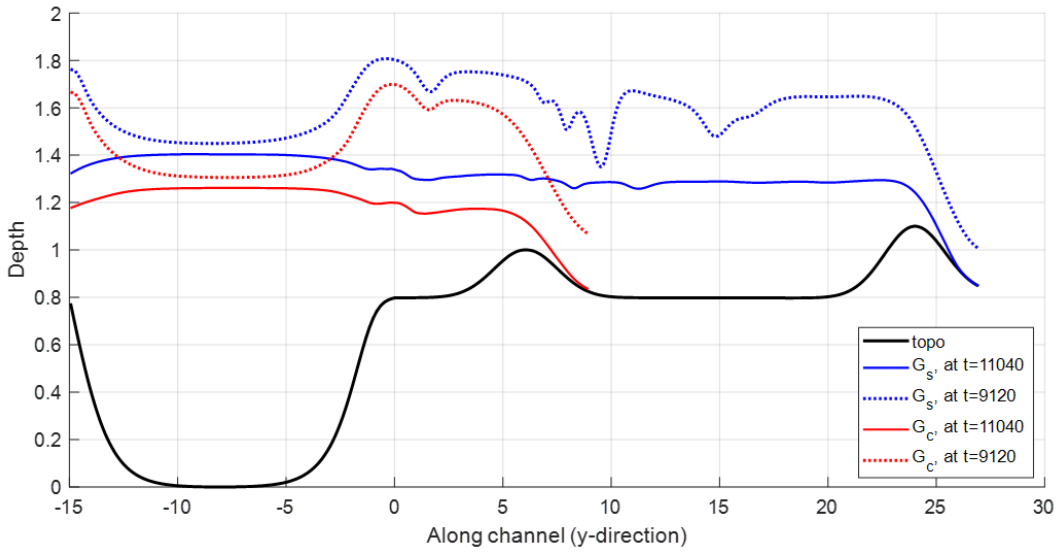

Figure 4.12: The interface height along the centerline of the channels for simulations G_c and G_s at two different times: $t = 9120$ (dotted curves) when the forcing is at its maximum and $t = 11040$ when the forcing is nearly zero (solid curves).

Figure 4.13 shows the interface height across the channel at the maximum and minimum of the inflow in the third seasonal cycle. When the inflow drops to zero (at the right tail of the Gaussian at $t = 11040$) from its maximum (at the peak of the Gaussian $t = 9120$), the interface height at the entrance (Figure 4.13 (a)) decreases by 20-30 %. The drop in the interface height is larger at the sill section (23-35 %) than the entrance (Figure 4.13 (b)). As

previously mentioned, it is evident that the interface height stands higher in the subcritical simulations than the hydraulically controlled simulations at all times. The slope of interface height at the entrance for the subcritical and the hydraulically controlled simulation is nearly the same. However, at the sill section, the hydraulically controlled flow has a steeper slope than the subcritical flow regardless of the phase of the forcing.

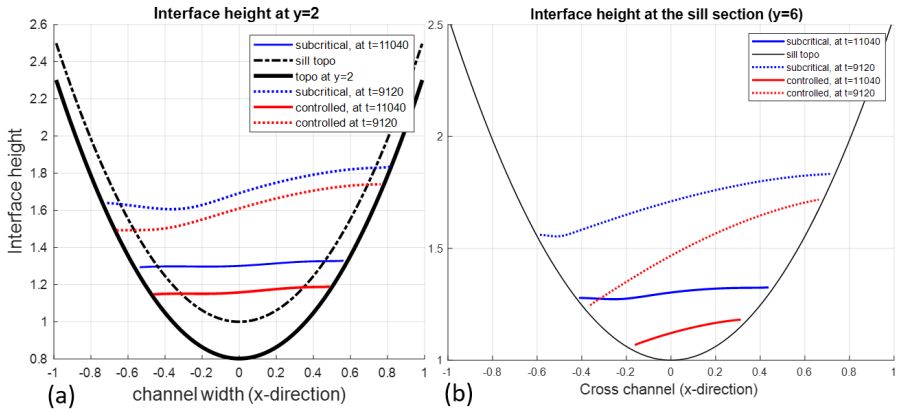

Figure 4.13: The interface height (a) at the entrance and (b) at the sill section for simulations G_c (blue curves) and G_s (red curves) at two different times $t = 9120$ (dotted curves) when the forcing is at its maximum and $t = 11040$ when the forcing is nearly zero (solid curves).

The contours of interface height in the basin and the channel are plotted in Figure 4.14 for the subcritical simulation G_s at the two time snaps. The circulation in the basin and the flow in the channel are similar to what we saw earlier in Figure 4.1 (c) for simulation A_s with constant inflow (the magnitude of the contours is different, but the nature of how and where they converge is the same). This is true if we compare any given time snapshots of flow for any of the experiments. The rotation and the geometry of the basin-channel system seems to influence the circulation more than the forcing properties. Therefore,

it is not trivial to deduce the time variability in forcing from snapshots of interface height.

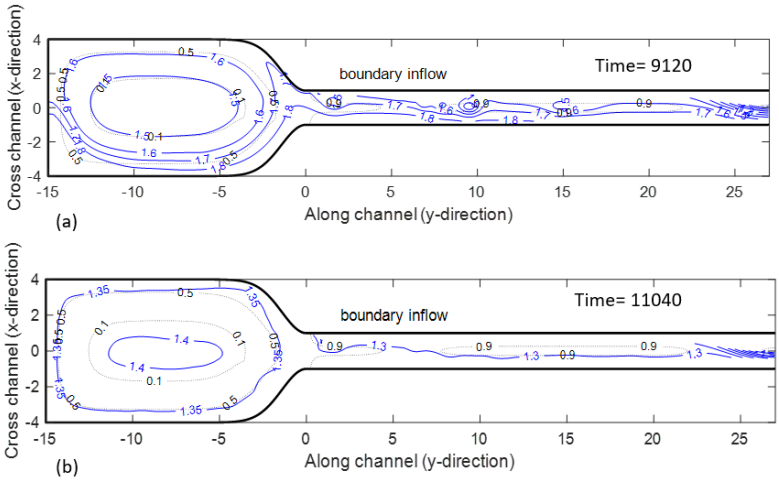

Figure 4.14: The interface height contours in the channel and the basin for simulation G_s at (a) $t = 9120$ when the forcing is at its maximum and (b) $t = 11040$ when the forcing is nearly zero.

4.4 Summary and Discussion

In this chapter, we illustrated the role of hydraulic control on the variability in transport observed in some sea-straits on a range of timescales from daily to interannual. To specifically diagnose the role of hydraulic control on the suppression of time dependence, we ran two series of experiments with periodic inflow in the upstream basin: (i) subcritical and (ii) hydraulically controlled flow. We explored the nature of the response of the basin and the sill to various periodic forcing.

Results reveal that the transport signal in the basin and the channel closely follow the forcing function with a phase lag and reduction in the amplitude

regardless of the flow regime. There is a high frequency variability in the basin that persists even when the forcing is constant. The frequency of this variability is on the order of Kelvin wave circumnavigation in the basin. This upstream basin variability is larger when the flow is subcritical and the waves generated downstream can travel back to the basin.

The subcritical flow causes intermittent variations in the water height while the controlled case gives a permanent change over the sill, regardless of whether the forcing is periodic or constant. This characteristic of the subcritical flow was known before and is consistent with Pratt and Whitehead, 2008 where they considered constant imposed transport (in their section 1.8). However, the sensitivity to the different forcing was not studied before.

There are two main mechanisms that suppress variability in the channel: (1) rising of the topography and narrowing of the geometry from the deep basin to the shallow channel, and (2) hydraulic control. The results reveal that the narrowing and shallowing of topography leads to 5-30% reduction of transport variability for the experiments listed in Table 4.1. This suppression in the amplitude of variability is not necessarily monotonic in relation to the magnitude of forcing frequency. For the controlled experiments, the reduction in amplitude is within 0-20%. The reduction of the amplitude at the sill is stronger for the hydraulically controlled flow, only for the high-frequency motions. The added reduction in amplitude due to hydraulic control is relatively minor at the forcing frequency (e.g., the reductions for the case shown in Figure 4.8 at the forcing frequency are about the same). The phase lags between the inflow and the response at the sill are generally longer

in the controlled cases relative the subcritical counterparts. This is because the overall layer thickness in the subcritical regime is larger, therefore the signals travel more rapidly.

The experiments additionally showed that the variability in the forcing magnitude and frequency does not affect the general pattern of circulation in the basin or the channel.

The results from the idealized experiments suggest that hydraulic control cannot be the main cause of variability at FBC. The role of topographic variation at FBC as well as atmospheric conditions need to be explored as a future work.

Chapter 5

Discussion and Conclusion

> I could be bounded in a nutshell and count myself king of infinite space.
>
> W. Shakespeare, Hamlet.

5.1 Summary and Conclusions

Many of the deep watermasses in the ocean originate in the deep overflows and their properties are set by the mixing that takes place in narrow straits or down the continental slopes. One example of these places is the Nordic Seas overflows that occur in the Greenland Scotland Ridge, mainly at the Denmark Strait and Faroe Bank Channel. The overflow through these two deep passages are the main sources of the North Atlantic Deep Water (NADW) and together they contribute to the deep branch of the AMOC. In this thesis, we first studied the sources of the Denmark Strait Overflow to better understand the composition and details of its pathways. Then we studied rotating hydraulics of an idealized basin-channel system with application to the Faroe Bank

Channel to suggest overflow monitoring strategies and also to understand the effect of hydraulic control on suppressing the time variability in transport at the sill.

We studied the kinematics of Denmark Strait Overflow in Chapter 2. We presented a detailed analysis of the upstream sources and pathways of the DSO by performing a Lagrangian analysis on the output of a high resolution ocean model of the Nordic Seas. The kinematic study gave a comprehensive understanding of the time-varying contribution to the overflow and evolution of previously identified northern pathways (the NIJ, the EGC, and the sEGC). Additionally, we found new pathways that feed the NADW from south of the Denmark Strait sill. These southern pathways supply 26% of the DSO during winter (JFM) of 2008 and are speculated to be the result of rapid transformation of the NIIC to the dense overflow. The schematic of the overflow water is updated by incorporating the direct pathways of the DSO. The evolution of hydrographic properties of the DSO is also presented. This study showed that the properties of all DSO sources converge after cascading over the Denmark Strait. Therefore, it is not trivial to discern the DSO sources at the sill section or south of it by watermass analysis. In addition to revealing a new pathway, the results suggest a generic method to study the evolution of watermasses. The combination of Lagrangian and watermass analysis can locate the watermass transformation sites continuously along the pathways (see Figure 2.14).

In Chapter 3, we explored the dynamics of overflow pathway partitioning and the effect of upstream reservoir on the overflow production for an idealized sea-strait geometry with parabolic cross-section. We studied the

sensitivity of the hydraulic solution (transport, and circulation) to the strait geometry and developed three overflow monitoring strategies. The results show that the flow in the channel is relatively insensitive to the basin circulation and the mass source type. Far enough from the channel entrance, the hydraulically controlled flow in the strait is independent of the basin circulation regardless of parabolic curvature. The controlled transport relation is derived for the case of uniform pv theory. Comparing the model to theory, we found that the measurement of the wetted edges of the interface height at the critical section can be used to estimate the volume flux. We also find that the simulated transport is well approximated by uniform pv theory, despite pv variation in the simulations. The three monitoring strategies we suggested only require making 1-3 measurements. We applied these strategies to the Faroe Bank Channel to estimate the transport and made a comparison with observations (see Figures 3.7 and 3.8). The results showed that the estimated transports are within the range of observed values. These monitoring strategies can be applied to similar deep passages and fracture zones around the world and are potentially useful in informing the deep ocean monitoring missions.

In Chapter 4, we studied the effect of hydraulic control on the variability in transport at the sill on different time scales such as seasonal. We forced our numerical model with periodic inflow in the upstream basin for subcritical and hydraulically controlled flow to see the effect of hydraulic control on the suppression of time dependence. Results show that the subcritical flow causes intermittent variations in the water height while the hydraulically controlled flow gives a permanent change over the sill, regardless of whether

the forcing is periodic or constant. The results reveal that the narrowing and shallowing of topography leads to reduction of transport variability. This suppression in the amplitude of variability is not necessarily monotonic in relation to the magnitude of forcing frequency. Hydraulic control causes a further suppression of time variability. However, the added reduction in amplitude afforded by hydraulic control is relatively minor, suggesting other potential mechanisms playing a role in variability of overflows at some sea straits such as FBC.

5.2 Future Work

In Chapter 2 we learned that the southern pathways of the DSO exist in the winter months of cold years when the NAO index is relatively high. Therefore, it is hypothesized that the phase of the NAO affects the partitioning of the DSO pathways (Harden et al., 2016). In Chapter 4, we learned that the shallowing and narrowing of topography from the upstream basin to the channel leads to the suppression of variability. We also learned that the role of hydraulic control in suppressing overflow variability is minimal and there must be other mechanisms in play. The surface wind can affect the potential vorticity distribution and the interface height in the upstream basin, both of which should have an impact on the overflow partitioning and transport variability. Additionally, the strength of the windstress affects the convection in the upstream basin, and therefore, the amount and timing of dense water production. To study these potential sources of overflow variability, the reduced gravity model used in Chapters 3 and 4 needs to be extended to two

layers. The windstress curl resembling that of the Nordic Seas can be imposed as an additional forcing on the top layer. A sensitivity study can be performed on the effect of wind direction and magnitude on the basin circulation, the fluid exchange between the two layers, and the variability in the overflow that reaches the sill.

Appendix A

The Hazards of Teaching for the First Time

I would like to share my learning experience as a PhD student teaching my first undergraduate course during fall 2020: Natural Hazards. Teaching this course, I wrestled with several questions: How can I engage students in a virtual setting? How can I make them think? What is the purpose of education after all and what do I want them to take away from the course?

A.1 About the course setting

Fall semester 2020 was a unique time to teach a course on natural hazards in the sense that all students were directly impacted by at least one type of disaster - the global pandemic. In addition, the semester coincided with a record-breaking Atlantic hurricane season on the East Coast and fires on the West Coast. I used these events as an opportunity to spark students' curiosity and motivate them to learn about the science of natural hazards. As a student, my best learning experiences happened through dialogues

and exchange of ideas between classmates and instructors that continued back and forth during class time. This experience inspired me to hold more than half of the class sessions synchronously. To focus students' attention, I motivated every class session by posing questions. For example, which hazards are the most destructive, frequent, or deadly? What is the effect of climate change on these hazards? What can we do about them? Some of these questions are open ended and may sound overwhelming at first, but to me, the essential step in learning is to become curious enough to engage with questions and take steps to answer them. Isn't the purpose of education to train future thinkers? The course included clear learning objectives following Bloom's Taxonomy to target both lower- and higher-level thinking skills. I designed multiple forms of assignments such as conducting readings, listening to podcasts, watching documentaries, completing analytical exercises, and participating in group discussions. To motivate the sense of exploration in students, instead of exams, I assigned a final term paper in which students investigated a natural disaster case study of their own interest. The assessment was structured using specifications grading. The method directly links course grades to achievements of learning objectives and motivates students to focus on learning instead of earning points (Kelly, 2018). Grading rubrics were provided for each individual assignment.

A.2 lab demonstrations

Just as a picture is worth a thousand words, lab demonstrations go a long way to supplement lectures and to improve conceptual understanding of

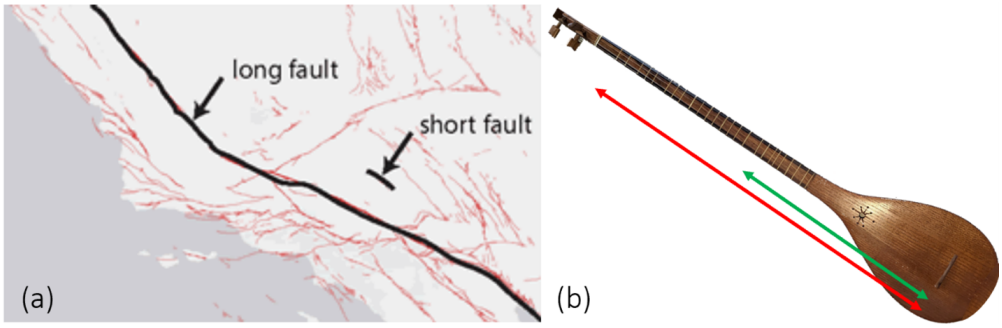

Figure A.1: Comparison of seismic waves to the sound waves generated by a string instrument. (a) length of two Earthquake faults (USGS, 2020). (b) music instrument producing analogous sound waves. The red and green arrows show the note, D, played on the same string in different octaves.

learning materials. But is it possible to perform them in a remote setting? Simple demonstrations were still possible. I just needed to get creative in implementing them! For example, I used a rubber band and a biscuit to demonstrate the strength of brittle versus elastic materials under various modes of deformation to explain how the choice of materials can make a drastic difference in what modes of deformation a building tolerates during an earthquake, which impacts the survival rate during an earthquake. I also used a musical instrument, my Setar, as an analogy for seismic waves. Just seeing the instrument immediately captured the students' attention. I played the same note at different octaves and reminded them how that results in a different pitch due to the string being confined to two different lengths. This is analogous to having a short versus long earthquake fault and therefore higher or lower frequency in seismic waves as in Figure A.1. Students were also given an exercise to listen to the sound of earthquakes from an archive to infer the fault length.

A.3 Freedom to learn

Noam Chomsky often says in his interviews about education that students are taught to be passive and obedient rather than independent and creative (Robichaud, 2014). He believes education is a matter of laying out a string along which students will develop, but in their own way (Chomsky and Barsamian, 1996). Chomsky quotes his colleague's response to students asking about course content, saying "it is not important what we cover in the class but rather what we discover" (Chomsky and Barsamian, 1996). I was inspired by this perspective and decided to encourage the enlightenment style of learning in my students by giving them freedom in their final term paper writing style. I encouraged the students to pick a case study based on what they loved to learn about natural hazards and gave them freedom in how to structure their writing or what to expand on (the science of the disaster, the losses, the social impacts, the aftermath, etc.). I was surprised to see so many of the students asked for strict guidelines, templates and sample term papers from previous semesters, as if the meaning of freedom and creativity in learning was unfamiliar to them!

A.4 Student perceptions of the class

I administered two anonymous feedback surveys, one in the middle of the semester and the other at the end. The mid-semester survey was focused on understanding what is working (not working) for students that I should keep (stop) doing, and what additional activities we could start doing to

better adapt to the unexpected transition to online learning. I learned that students had a lot to say, some of which I incorporated in the second half of the semester, such as taking a class session to practice writing the term paper and hold a Q and A session. The end-of-semester survey was more focused on their takeaways from the class, and what assignments/activities were most helpful in their learning experience. I specifically asked them questions such as, “What do you think you will remember from this course? What did you discover?"

The final survey revealed that by the end of the semester students, regardless of their background, comprehended the major earth processes and reflected on the relation between humans and natural disasters. They grasped the interdisciplinary nature of the course and how one can learn about intersection of physics, humanities, and international relations through studying natural hazards and disasters. They also developed a sense of appreciation for the role of science in predicting and dealing with natural hazards.

A.5 What I learned

Even though universities like Hopkins often train Ph.D. students to focus on producing publications rather than doing curiosity-driven research, I found that teaching a course like this led me to ask the kind of fundamental questions that could stimulate future research. This experience helped me develop as a teacher, as well as a true scientist, while raising awareness and sharing important knowledge about natural hazards in a changing climate in which the frequency of hazardous events will likely increase. I captured students’

attention by making the learning relevant to their lives, which inspired their curiosity. Feedback surveys revealed and reinforced my idea that synchronous class discussions, constant questioning, and interesting lab demos would hook the students and motivate them to engage in dialogue.

References

Aagaard, K., J. H. Swift, and E. C. Carmack (1985). "Thermohaline circulation in the Arctic Mediterranean Seas". In: *Journal of Geophysical Research: Oceans* 90.C3, pp. 4833–4846. DOI: https://doi.org/10.1029/JC090iC03p04833.

Alford, Matthew H., James B. Girton, Gunnar Voet, Glenn S. Carter, John B. Mickett, and Jody M. Klymak (2013). "Turbulent mixing and hydraulic control of abyssal water in the Samoan Passage". In: *Geophysical Research Letters* 40.17, pp. 4668–4674. DOI: https://doi.org/10.1002/grl.50684. URL: https://agupubs.onlinelibrary.wiley.com/doi/abs/10.1002/grl.50684.

Almansi, Mattia, Thomas W. N. Haine, Robert S. Pickart, Marcello G. Magaldi, Renske Gelderloos, and Dana Mastropole (2017). "High-frequency variability in the circulation and hydrography of the Denmark Strait Overflow from a high-resolution numerical model". In: *Journal of Physical Oceanography* 47.12, pp. 2999–3013. ISSN: 0022-3670. DOI: 10.1175/JPO-D-17-0129.1.

Appen, Wilken-Jon von, Inga M. Koszalka, Robert S. Pickart, Thomas W.N. Haine, Dana Mastropole, Marcello G. Magaldi, H. Valdimarsson, James Girton, Kerstin Jochumsen, and Gerd Krahmann (2014). "The East Greenland Spill Jet as an important component of the Atlantic Meridional Overturning Circulation". In: *Deep Sea Research Part I: Oceanographic Research Papers* 92, pp. 75 –84. ISSN: 0967-0637. DOI: https://doi.org/10.1016/j.dsr.2014.06.002. URL: http://www.sciencedirect.com/science/article/pii/S0967063714001022.

Armi, Laurence (1986). "The hydraulics of two flowing layers with different densities". In: *Journal of Fluid Mechanics* 163, pp. 27–58. DOI: 10.1017/S0022112086002197.

Bamber, Jonathan, Michiel van den Broeke, Janneke Ettema, Jan Lenaerts, and Eric Rignot (2012). "Recent large increases in freshwater fluxes from Greenland into the North Atlantic". In: *Geophysical Research Letters* 39.19. DOI: 10.1029/2012GL052552.

Behrendt, Axel, Hiroshi Sumata, Benjamin Rabe, and Ursula Schauer (2017). *A comprehensive, quality-controlled and up-to-date data set of temperature and salinity data for the Arctic Mediterranean Sea (Version 1.0), links to data files*. data set. DOI: 10.1594/PANGAEA.872931.

Behrens, Erik, Kjetil Våge, Benjamin Harden, Arne Biastoch, and Claus W Boning (2017). "Composition and variability of the Denmark Strait Overflow Water in a high-resolution numerical model hindcast simulation". In: *Journal of Geophysical Research: Oceans* 122.4, pp. 2830–2846. DOI: 10.1002/2016JC012158. URL: https://agupubs.onlinelibrary.wiley.com/doi/abs/10.1002/2016JC012158.

Bell, Johns, Jay Solomon, and William Szymczak (1989). "A second-order projection method for the incompressible Navier Stokes equations on quadrilateral grids". In: *9th Computational Fluid Dynamics Conference*, pp. 370–379. DOI: 10.2514/6.1989-1967.

Borenäs, M. and P. A. Lundberg (1986). "Rotating hydraulics of flow in a parabolic channel". In: *Journal of Fluid Mechanics* 167, pp. 309–326.

Borenäs, M. and P. A. Lundberg (1988). "On the deep-water flow through the Faroe Bank Channel". In: *Journal of Geophysical Research: Oceans* 93.C2, pp. 1281–1292.

Borenäs, M. and A. Nikolopoulos (2000). "Theoretical calculations based on real topography of the maximum deep-water flow through the Jungfern Passage." In: *Journal of Marine Research* 58, pp. 423–440.

Bray, N. A., J. Ochoa, and T. H. Kinder (1995). "The role of the interface in exchange through the Strait of Gibraltar". In: *Journal of Geophysical Research: Oceans* 100.C6, pp. 10755–10776. DOI: https://doi.org/10.1029/95JC00381.

Chassignet, Eric P., Claudia Cenedese, and Jacques Verron (2012). "Tracer evidence of the origin and variability of Denmark Strait Overflow Water". In: *Buoyancy-driven flows*. Cambridge University Press. Chap. 5, pp. 200–222.

Chomsky, N. and D. Barsamian (1996). *Class Warfare: interviews with David Barsamian*. Monroe , Maine.

Clement, Louis, Andreas M. Thurnherr, and Louis C. St. Laurent (2017). "Turbulent Mixing in a Deep Fracture Zone on the Mid-Atlantic Ridge". In: *Journal of Physical Oceanography* 47.8, pp. 1873 –1896. DOI: 10.1175/JPO-D-16-0264.1.

Cooper, L.H.N (1955). "Deep water movements in the North Atlantic as a link between climatic changes around Iceland and biological productivity

of the English Channel and Celtic Sea". In: *Journal of Marine Reseach* 14, pp. 347–362.

Cummings, James A. and Ole Martin Smedstad (2014). "Ocean Data Impacts in Global HYCOM". In: *Journal of Atmospheric and Oceanic Technology* 31.8, pp. 1771–1791. DOI: 10.1175/JTECH-D-14-00011.1. eprint: https://doi.org/10.1175/JTECH-D-14-00011.1. URL: https://doi.org/10.1175/JTECH-D-14-00011.1.

Dickson, Robert R. and Juan Brown (1994). "The production of North Atlantic deep water: Sources, rates, and pathways". In: *Journal of Geophysical Research: Oceans* 99.C6, pp. 12319–12341. DOI: 10.1029/94JC00530. eprint: https://agupubs.onlinelibrary.wiley.com/doi/pdf/10.1029/94JC00530. URL: https://agupubs.onlinelibrary.wiley.com/doi/abs/10.1029/94JC00530.

Donlon, Craig J., Matthew Martin, John Stark, Jonah Roberts-Jones, Emma Fiedler, and Werenfrid Wimmer (2012). "The Operational Sea Surface Temperature and Sea Ice Analysis (OSTIA) system". In: *Remote Sensing of Environment* 116, pp. 140 –158.

Drange, Helge, Trond Dokken, Tore Furevik, Rüdiger Gerdes, Wolfgang Berger, Atle Nesje, Kjell Arild Orvik, Øystein Skagseth, Ingunn Skjelvan, and Svein Østerhus (2005). "The Nordic Seas: An Overview". In: *The Nordic Seas: An Integrated Perspective*. American Geophysical Union (AGU), pp. 1–10. ISBN: 9781118666296. DOI: https://doi.org/10.1029/158GM02.

Gelderloos, R., A. S. Szalay, T. N. Haine, and G. Lemson (2016). "A fast algorithm for neutrally-buoyant Lagrangian particles in numerical ocean modeling". In: *2016 IEEE 12th International Conference on e-Science (e-Science)*. Los Alamitos, CA, USA: IEEE Computer Society, pp. 381–388. DOI: 10.1109/eScience.2016.7870923.

Gill, A. E. (1977). "The hydraulics of rotating-channel flow". In: *Journal of Fluid Mechanics* 80.4, pp. 641–671.

Haine, Thomas, Claus Böning, Peter Brandt, Jürgen Fischer, Andreas Funk, Dagmar Kieke, Erik Kvaleberg, Monika Rhein, and Martin Visbeck (2008). "North Atlantic Deep Water Formation in the Labrador Sea, Recirculation Through the Subpolar Gyre, and Discharge to the Subtropics". In: *Arctic–Subarctic Ocean Fluxes: Defining the Role of the Northern Seas in Climate*. Dordrecht: Springer Netherlands, pp. 653–701. ISBN: 978-1-4020-6774-7. DOI: 10.1007/978-1-4020-6774-7_28. URL: https://doi.org/10.1007/978-1-4020-6774-7_28.

Hansen, B., K. M. Húsgar Larsen, H. Hátún, and S. Østerhus (2016). "Astable Faroe Bank Channel overflow 1995–2015". In: *Ocean Science* 12, 1205 – 1220. DOI: 10.5194/os-12-1205-2016.

Harden, B. E., R. S. Pickart, Hédinn Valdimarsson, Kjetil Våge, Laura de Steur, Clark Richards, Frank Bahr, Dan Torres, Eli Børve, Steingrímur Jónsson, Andreas Macrander, Svein Østerhus, Lisbeth Håvik, and Tore Hattermann (2016). "Upstream sources of the Denmark Strait Overflow: Observations from a high-resolution mooring array". In: *Deep-Sea Research Part I: Oceanographic Research Papers* 112, pp. 94–112. ISSN: 09670637. DOI: 10.1016/j.dsr.2016.02.007.

Helfrich, K. R., A. C. Kuo, and L. J. Pratt (1999). "Nonlinear Rossby adjustment in a channel". In: *Journal of Fluid Mechanics* 390, pp. 187–222.

Helfrich, Karl R. (1995). "Time-Dependent Two-Layer Hydraulic Exchange Flows". In: *Journal of Physical Oceanography* 25.3, pp. 359 –373.

Helfrich, Karl R. and Lawrence J. Pratt (2003). "Rotating Hydraulics and Upstream Basin Circulation". In: *Journal of Physical Oceanography* 33.8, pp. 1651 –1663. DOI: 10.1175/2383.1.

Huang, J., R.S. Pickart, R.X. Huang, P. Lin, A. Brakstad, and F. Xu (2020). "Sources and upstream pathways of the densest overflow water in the Nordic Seas". In: *Nature Communication* 11, pp. 79 –90. DOI: https://doi.org/10.1038/s41467-020-19050-y.

ICES (2006). *International Council for the Exploration of the Seas hydrographic dataset*. data set. Copenhagen. URL: https://doi.org/10.5065/D6X9291B.

Jackett, David R. and Trevor J. Mcdougall (1995). "Minimal Adjustment of Hydrographic Profiles to Achieve Static Stability". In: *Journal of Atmospheric and Oceanic Technology* 12.2, pp. 381–389. DOI: 10.1175/1520-0426(1995)012<0381:MAOHPT>2.0.CO;2.

Jeansson, Emil, Sara Jutterström, Bert Rudels, Leif G. Anderson, K. Anders Olsson, E. Peter Jones, William M. Smethie, and James H. Swift (2008). "Sources to the East Greenland Current and its contribution to the Denmark Strait Overflow". In: *Progress in Oceanography* 78.1, pp. 12 –28. ISSN: 0079-6611. DOI: https://doi.org/10.1016/j.pocean.2007.08.031.

Jochumsen, Kerstin, Martin Moritz, Nuno Nunes, Detlef Quadfasel, Karin M.H. Larsen, Bogi Hansen, Hedinn Valdimarsson, and Steingrimur Jonsson (2017). "Revised transport estimates of the Denmark Strait overflow". In: *Journal of Geophysical Research: Oceans* 122.4, pp. 3434–3450. DOI: 10.1002/2017JC012803.

Jochumsen, Kerstin, Sarah M. Schnurr, and Detlef Quadfasel (2016). "Bottom temperature and salinity distribution and its variability around Iceland". In: *Deep Sea Research Part I: Oceanographic Research Papers* 111, pp. 79 –90. ISSN: 0967-0637. DOI: https://doi.org/10.1016/j.dsr.2016.02.009.

Jong, M. Femke de, Henrik Søiland, Amy S. Bower, and Heather H. Furey (2018). "The subsurface circulation of the Iceland Sea observed with RAFOS floats". In: *Deep Sea Research Part I: Oceanographic Research Papers*. ISSN: 0967-0637. DOI: https://doi.org/10.1016/j.dsr.2018.07.008.

Jónsson, Steingrimur and Hedinn Valdimarsson (2004). "A new path for the Denmark Strait overflow water from the Iceland Sea to Denmark Strait". In: *Geophysical Research Letters* 31.3, pp. 2–5. ISSN: 00948276. DOI: 10.1029/2003GL019214.

Kelly, Rebecca (2018). *Meaningful grades with specification grading*. https://cer.jhu.edu/files/InnovInstruct-Ped-18_specifications-grading.pdf.

Killworth, Peter D. and N. Robb McDonald (1993). "Maximal reduced-gravity flux in rotating hydraulics". In: *Geophysical & Astrophysical Fluid Dynamics* 70.1-4, pp. 31–40. DOI: 10.1080/03091929308203585.

Knupp, Patrick and Stanly Steinberg (1993). *The Fundamentals of Grid Generation*. Florida: CRC Press.

Köhl, Armin, Rolf H. Käse, Detlef Stammer, and Nuno Serra (2007). "Causes of changes in the Denmark Strait overflow". In: *Journal of Physical Oceanography* 37.6, pp. 1678–1696. DOI: 10.1175/JPO3080.1. eprint: https://doi.org/10.1175/JPO3080.1. URL: https://doi.org/10.1175/JPO3080.1.

Koszalka, Inga M., Thomas W. N. Haine, and Marcello G. Magaldi (2013). "Fates and travel times of Denmark Strait overflow water in the Irminger Basin". In: *Journal of Physical Oceanography* 43.12, pp. 2611–2628. DOI: 10.1175/JPO-D-13-023.1.

Koszalka, Inga M., Thomas W.N. Haine, and Marcello G. Magaldi (2017). "Mesoscale mixing of the Denmark Strait overflow in the Irminger Basin". In: *Ocean Modelling* 112, pp. 90 –98. ISSN: 1463-5003. DOI: https://doi.org/10.1016/j.ocemod.2017.03.001.

Käse, R. H., J. B. Girton, and T. B. Sanford (2003). "Structure and variability of the Denmark Strait Overflow: Model and observations". In: *Journal of Geophysical Research: Oceans* 108.C6. DOI: 10.1029/2002JC001548. eprint: https://agupubs.onlinelibrary.wiley.com/doi/pdf/10.1029/2002JC001548. URL: https://agupubs.onlinelibrary.wiley.com/doi/abs/10.1029/2002JC001548.

Lake, Iréne, Karin Borenäs, and Peter Lundberg (2005). "Potential-Vorticity Characteristics of the Faroe Bank Channel Deep-Water Overflow". In: *Journal of Physical Oceanography* 35.6, pp. 921 –932. DOI: 10.1175/JPO2721.1.

Lauvset, Siv K., Ailin Brakstad, Kjetil Våge, Are Olsen, Emil Jeansson, and Kjell Arne Mork (2018). "Continued warming, salinification and oxygenation of the Greenland Sea gyre". In: *Tellus A: Dynamic Meteorology and Oceanography* 70.1, pp. 1–9. DOI: 10.1080/16000870.2018.1476434.

Losch, Martin, D. Menemenlis, J. M. Campin, P. Heimbach, and C. Hill (2010). "On the formulation of sea-ice models. Part 1: Effects of different solver implementations and parameterizations." In: *Ocean Modelling, 33144* 129. DOI: 10.1016/j.ocemod.2009.12.008. URL: http://dx.doi.org/10.1016/j.ocemod.2009.12.008.

Macrander, A., U. Send, H. Valdimarsson, S. Jónsson, and R. H. Käse (2005). "Interannual changes in the overflow from the Nordic Seas into the Atlantic Ocean through Denmark Strait". In: *Geophysical Research Letters* 32.6. DOI: 10.1029/2004GL021463. URL: https://agupubs.onlinelibrary.wiley.com/doi/abs/10.1029/2004GL021463.

Macrander, Andreas, Rolf Käse, Uwe Send, Heðinn Valdimarsson, and Steingrímur Jónsson (2007). "Spatial and temporal structure of the Denmark Strait overflow revealed by acoustic observations". In: *Journal of Ocean Dynamics* 57, pp. 75–89. DOI: https://doi.org/10.1007/s10236-007-0101-x.

Malmberg, Svend-Aage and Héðinn Valdimarsson (2003). "Hydrographic conditions in Icelandic waters, 1990-1999". In: *ICES Marine Science Symposia* 69.5, pp. 50–60.

Marinov, I., M. Follows, A. Gnanadesikan, J. L. Sarmiento, and R. D. Slater (2008). "How does ocean biology affect atmospheric pCO2? Theory and models". In: *Journal of Geophysical Research: Oceans* 113.C7. DOI: https://doi.org/10.1029/2007JC004598.

Marshall, John, Alistair Adcroft, Chris Hill, Lev Perelman, and Curt Heisey (1997). "A finite-volume, incompressible Navier-Stokes model for studies of the ocean on parallel computers". In: *Journal of Geophysical Research: Oceans* 102.C3, pp. 5753–5766. DOI: 10.1029/96JC02775. URL: https://agupubs.onlinelibrary.wiley.com/doi/abs/10.1029/96JC02775.

Mastropole, Dana, Robert S. Pickart, Héðinn Valdimarsson, Kjetil Våge, Kerstin Jochumsen, and James Girton (2017). "On the hydrography of Denmark Strait". In: *Journal of Geophysical Research: Oceans* 122.1, pp. 306–321.

DOI: 10.1002/2016JC012007. URL: https://agupubs.onlinelibrary.wiley.com/doi/abs/10.1002/2016JC012007.

Mauritzen, Cecilie (1996). "Production of dense overflow waters feeding the North Atlantic across the Greenland-Scotland Ridge. Part 1: Evidence for a revised circulation scheme". In: *Deep Sea Research Part I: Oceanographic Research Papers* 43.6, pp. 769 –806. ISSN: 0967-0637. DOI: https://doi.org/10.1016/0967-0637(96)00037-4.

McCartney, M.S. (1992). "Recirculating components to the deep boundary current of the northern North Atlantic". In: *Progress in Oceanography* 29.4, pp. 283 –383. ISSN: 0079-6611. DOI: https://doi.org/10.1016/0079-6611(92)90006-L.

Moritz, Martin, Kerstin Jochumsen, Ryan P. North, Detlef Quadfasel, and Héðinn Valdimarsson (2019). "Mesoscale Eddies Observed at the Denmark Strait Sill". In: *Journal of Geophysical Research: Oceans* 124.11, 7947– 7961. DOI: 10.1029/2019JC015273.

Noël, B., W. J. van de Berg, H. Machguth, S. Lhermitte, I. Howat, X. Fettweis, and M. R. van den Broeke (2016). "A daily, 1 km resolution data set of downscaled Greenland ice sheet surface mass balance (1958–2015)". In: *The Cryosphere* 10.5, pp. 2361–2377. DOI: 10.5194/tc-10-2361-2016.

North, Ryan P., Kerstin Jochumsen, and Martin Moritz (2018). "Entrainment and Energy Transfer Variability Along the Descending Path of the Denmark Strait Overflow Plume". In: *Journal of Geophysical Research: Oceans* 123.4, pp. 2795–2807. DOI: 10.1002/2018JC013821. eprint: https://agupubs.onlinelibrary.wiley.com/doi/pdf/10.1002/2018JC013821.

Østerhus, S., R. Woodgate, H. Valdimarsson, B. Turrell, L. de Steur, D. Quadfasel, S. M. Olsen, M. Moritz, C. M. Lee, K. M. H. Larsen, S. Jónsson, C. Johnson, K. Jochumsen, B. Hansen, B. Curry, S. Cunningham, and B. Berx (2019). "Arctic Mediterranean exchanges: a consistent volume budget and trends in transports from two decades of observations". In: *Ocean Science* 15.2, pp. 379–399. DOI: 10.5194/os-15-379-2019.

Østerhus, Svein, Sherwin Toby, Detelef Quadfasel, and Bogi Hansen (2008). "The Overflow Transport East of Iceland". In: *Arctic–Subarctic Ocean Fluxes: Defining the Role of the Northern Seas in Climate*. Dordrecht: Springer Netherlands, pp. 423–435. ISBN: 978-1-4020-6774-7. DOI: 10.1007/978-1-4020-6774-7_28. URL: https://doi.org/10.1007/978-1-4020-6774-7_28.

Palsson, Jonbjorn, Olafur S. Astthorsson, and Héðinn Valdimarsson (2012). "Hydrographic variability in Icelandic waters during recent decades and related changes in distribution of some fish species". In: *ICES Journal of*

Marine Science 69.5, pp. 816–825. ISSN: 1054-3139. DOI: 10.1093/icesjms/fss027. URL: https://dx.doi.org/10.1093/icesjms/fss027.

Peters, Hartmut, William E. Johns, Amy S. Bower, and David M. Fratantoni (2005). "Mixing and Entrainment in the Red Sea Outflow Plume. Part I: Plume Structure". In: *Journal of Physical Oceanography* 35.5, pp. 569 –583. DOI: 10.1175/JPO2679.1.

Pickart, Robert S., Michael A. Spall, Daniel J. Torres, Kjetil Våge, Hedinn Valdimarsson, C. Nobre, G. W. K. Moore, Steingrimur Jonsson, and Dana Mastropole (2017). "The North Icelandic Jet and its relationship to the North Icelandic Irminger Current". In: *Journal of Marine Research* 75.5, pp. 605–639. ISSN: 0022-2402. DOI: 10.1357/002224017822109505.

Pratt, L. J. and M. Chechelnitsky (1997). "Principles for capturing the upstream effects of deep sills in low resolution ocean models". In: *Dynamics of Atmospheres and Oceans* 26, pp. 1 –25. DOI: https://doi.org/10.1016/S0377-0265(96)00483-6.

Pratt, L J and J A Whitehead (2008). *Rotating Hydraulics*. Vol. 167. Springer, p. 589. ISBN: 978-0-387-36639-5. DOI: 10.1007/978-0-387-49572-9.

Pratt, Larry J., Heather E. Deese, Stephen P. Murray, and William Johns (2000). "Continuous Dynamical Modes in Straits Having Arbitrary Cross Sections, with Applications to the Bab al Mandab". In: *Journal of Physical Oceanography* 30.10, pp. 2515 –2534.

Pratt, Larry J., Karl R. Helfrich, and David Leen (2008). "On the stability of ocean overflows". In: *Journal of Fluid Mechanics* 602, 241–266. DOI: 10.1017/S0022112008000827.

Pratt, Lawrence J. (1984). "On Nonlinear Flow with Multiple Obstructions". In: *Journal of Atmospheric Sciences* 41.7, pp. 1214 –1225.

Price, James F. and Molly O'Neil Baringer (1994). "Outflows and deep water production by marginal seas". In: *Progress in Oceanography* 33.3, pp. 161 –200. ISSN: 0079-6611. DOI: https://doi.org/10.1016/0079-6611(94)90027-2.

Reichelt, Mark W. and Lawrence F. Shampine (2010). *MATLAB*. Natick, Massachusetts: The MathWorks Inc.

Robichaud, Arianne (2014). "Interview with Noam Chomsky on Education." In: *Radical Pedagogy* 11.1, p. 4. ISSN: 15246345.

Ronski, Stephanie and Gereon Budéus (2005). "Time series of winter convection in the Greenland Sea". In: *Journal of Geophysical Research: Oceans* 110.C4.

Rossby, T., D. Dorson, and J. Fontaine (1986). "The RAFOS System". In: *Journal of Atmospheric and Oceanic Technology* 3.4, pp. 672–679. DOI: 10.1175/1520-0426(1986)003<0672:TRS>2.0.CO;2.

Rudels, Bert, Patrick Eriksson, Eberhard Fahrbach, Gereon Budéus, and Jens Meincke (2002). "The East Greenland Current and its contribution to the Denmark Strait overflow". In: *ICES Journal of Marine Science* 59.6, pp. 1133–1154. ISSN: 1054-3139. DOI: 10.1006/jmsc.2002.1284. eprint: http://oup.prod.sis.lan/icesjms/article-pdf/59/6/1133/6756418/59-6-1133.pdf. URL: https://dx.doi.org/10.1006/jmsc.2002.1284.

Sakov, P., F. Counillon, L. Bertino, K. A. Lisæter, P. R. Oke, and A. Korablev (2012). "TOPAZ4: an ocean-sea ice data assimilation system for the North Atlantic and Arctic". In: *Ocean Science* 8.4, pp. 633–656. DOI: 10.5194/os-8-633-2012. URL: https://www.ocean-sci.net/8/633/2012/.

Sannino, Gianmaria, J. C. Sánchez Garrido, L. Liberti, and L. Pratt (2014). "Exchange Flow through the Strait of Gibraltar as Simulated by a σ-Coordinate Hydrostatic Model and a z-Coordinate Nonhydrostatic Model". In: *The Mediterranean Sea*. American Geophysical Union (AGU). Chap. 3, pp. 25–50. ISBN: 9781118847572. DOI: https://doi.org/10.1002/9781118847572.ch3.

Semper, Stefanie, Kjetil Våge, Robert S. Pickart, Héðinn Valdimarsson, Daniel J. Torres, and Steingrímur Jónsson (2019). "The Emergence of the North Icelandic Jet and its evolution from northeast Iceland to Denmark Strait". In: *Journal of Physical Oceanography* 49.10, pp. 2499–2521. DOI: 10.1175/JPO-D-19-0088.1.

Smethie Jr., William M. and James H. Swift (1989). "The tritium:krypton-85 age of Denmark Strait Overflow Water and Gibbs Fracture Zone Water just south of Denmark Strait". In: *Journal of Geophysical Research: Oceans* 94.C6, pp. 8265–8275. DOI: 10.1029/JC094iC06p08265.

Spall, Michael A., Robert S. Pickart, Peigen Lin, Wilken-Jon von Appen, Dana Mastropole, H. Valdimarsson, Thomas W. N. Haine, and Mattia Almansi (2019). "Frontogenesis and Variability in Denmark Strait and Its Influence on Overflow Water". In: *Journal of Physical Oceanography* 49.7, pp. 1889–1904. DOI: 10.1175/JPO-D-19-0053.1. URL: https://doi.org/10.1175/JPO-D-19-0053.1.

Stern, Melvin E. (1972). "Rotating Hydraulics and Upstream Basin Circulation". In: *The Physics of Fluids* 15, pp. 2062 –2064. DOI: https://doi.org/10.1063/1.1693825.

Swift, James H. and Knut Aagaard (1981). "Seasonal transitions and water mass formation in the Iceland and Greenland seas". In: *Deep Sea Research Part A. Oceanographic Research Papers* 28.10, pp. 1107 –1129. ISSN: 0198-0149. DOI: https://doi.org/10.1016/0198-0149(81)90050-9.

Swift, James H., Knut Aagaard, and Svend-Aage Malmberg (1980). "The contribution of the Denmark strait overflow to the deep North Atlantic". In: *Deep Sea Research Part A. Oceanographic Research Papers* 27.1, pp. 29 –42. ISSN: 0198-0149. DOI: https://doi.org/10.1016/0198-0149(80)90070-9. URL: http://www.sciencedirect.com/science/article/pii/0198014980900709.

Talley, L D, G L Pickart, W J Emery, and J H Swift (2013). *Descriptive Physical Oceanography*. Elsevier. ISBN: 978-0-7506-4552-2.

Tanhua, Toste, Klaus Bulsiewicz, and Monika Rhein (2005). "Spreading of overflow water from the Greenland to the Labrador Sea". In: *Geophysical Research Letters* 32.10. DOI: 10.1029/2005GL022700.

Tanhua, Toste, K. Anders Olsson, and Emil Jeansson (2005). "Formation of Denmark Strait overflow water and its hydro-chemical composition". In: *Journal of Marine Systems* 57.3, pp. 264 –288. ISSN: 0924-7963. DOI: https://doi.org/10.1016/j.jmarsys.2005.05.003.

Tanhua, Toste, K. Anders Olsson, and Emil Jeansson (2008). "Tracer evidence of the origin and variability of Denmark Strait Overflow Water". In: *Arctic–Subarctic Ocean Fluxes: Defining the Role of the Northern Seas in Climate*. Dordrecht: Springer Netherlands, pp. 475–503. ISBN: 978-1-4020-6774-7. DOI: 10.1007/978-1-4020-6774-7_21. URL: https://doi.org/10.1007/978-1-4020-6774-7_21.

UCAR-NCAR and OHSTATE-POLARMET (2017). *Arctic System Reanalysis version 2*. Boulder CO. URL: https://doi.org/10.5065/D6X9291B.

USGS (2020). *Listening to Earthquake*. https://earthquake.usgs.gov/education/listen/index.php.

Våge, Kjetil, G.W.K. Moore, Steingrímur Jónsson, and Héinn Valdimarsson (2015). "Water mass transformation in the Iceland Sea". In: *Deep Sea Research Part I: Oceanographic Research Papers* 101, pp. 98 –109. ISSN: 0967-0637. DOI: https://doi.org/10.1016/j.dsr.2015.04.001.

Våge, Kjetil, Robert S. Pickart, Michael A. Spall, G.W.K. Moore, Héðinn Valdimarsson, Daniel J. Torres, Svetlana Y. Erofeeva, and Jan Even O. Nilsen (2013). "Revised circulation scheme north of the Denmark Strait". In: *Deep*

Sea Research Part I: Oceanographic Research Papers 79, pp. 20 –39. ISSN: 0967-0637. DOI: https://doi.org/10.1016/j.dsr.2013.05.007. URL: http://www.sciencedirect.com/science/article/pii/S0967063713001040.

Våge, Kjetil, Robert S. Pickart, Michael A. Spall, Héinn Valdimarsson, Steingrímur Jónsson, Daniel J. Torres, Svein Østerhus, and Tor Eldevik (2011). "Significant role of the North Icelandic Jet in the formation of Denmark Strait overflow water". In: *Nature Geoscience* 4.10, pp. 723–727. ISSN: 17520894. DOI: 10.1038/ngeo1234.

Valdimarsson, H. and SA. Malmberg (1999). "Near-surface circulation in the Icelandic waters derived from satellite tracked drifters". In: *Rit Fiskideildar* 16.5, pp. 23–39.

Whitehead, J. A. (1989). "Internal hydraulic control in rotating fluids— Applications to oceans." In: *Geophysical and Astrophysical Fluid Dynamics* 48, pp. 169–192.

Whitehead, J. A. (1998). "Topographic control of oceanic flows in deep passages and straits". In: *Reviews of Geophysics* 36, pp. 423–440.

Whitehead, J. A., A. Leetmaa, and R.A. Knox (1974). "Rotating hydraulics of strait and sill flows". In: *Geophysical Fluid Dynamics* 6.2, pp. 101–125. DOI: https://doi.org/10.1080/03091927409365790.

WOD (2013). *World Ocean Database*. data set. URL: https://www.nodc.noaa.gov/OC5/SELECT/dbsearch/dbsearch.html.